ELSEVIER

Physics Reports 246 (1994) 251–313

PHYSICS REPORTS

Principles and applications of grazing incidence X-ray and neutron scattering from ordered molecular monolayers at the air-water interface

Jens Als-Nielsen [a], Didier Jacquemain [b], Kristian Kjaer [a], Franck Leveiller [b], Meir Lahav [b], Leslie Leiserowitz [b]

[a] *Physics Department, RisøNational Laboratory, DK-4000 Roskilde, Denmark*

[b] *Department of Materials and Interfaces, Weizmann Institute of Science, Rehovot 76100, Israel*

Received April 1994; editor: M.L. Klein

Contents:

0370-1573/94/$26.00
SSDI 0370-1573(94)00070-J

Abstract

The advent of well collimated, high intensity synchrotron X-ray sources and the consequent development of surface-specific X-ray diffraction and fluorescence techniques have recently revolutionized the study of Langmuir monolayers at the air-liquid interface. These methods allowed for the first time the determination of the in-plane and vertical structure of such monolayers with a resolution approaching the atomic level. We briefly describe these methods, including grazing incidence X-ray diffraction, specular reflectivity, Bragg rods, standing waves and surface fluorescence techniques, and review recent results obtained for Langmuir films from their use. The methods have been successfully applied for the elucidation of the structure of crystalline aggregates of amphiphilic molecules at the water surface such as alcohols, carboxylic acids and their salts, α-amino acids and phospholipids. In addition, it became possible to monitor by diffraction the growth and dissolution of the crystalline self-aggregates as well as structural changes occurring by phase transitions. Furthermore, via the surface X-ray methods, new light is shed on the structure of the underlying attached solvent or solute ionic layer. Examples are given where singly or doubly charged ions bound to the two-dimensional (2D) crystal form either an ordered or diffuse counter-ionic layer. Finally, the surface diffraction methods provide data on transfer of structural information from 2D clusters to 3D single crystals which had been successfully accomplished by epitaxial-like crystallization both in organic and inorganic crystals.

1. Introduction

Early in this century, Langmuir demonstrated in a series of elegant experiments that amphiphilic molecules, composed of a hydrophobic tail and a hydrophilic head group, accumulate at the air-water interface [1]. These films still elicit wide interest because of their importance in the pure and applied sciences. For instance, Langmuir monolayers serve as useful models for elucidating structure and function of biological membranes in their interactions with lipids, steroids, sugars, proteins and ions [2]. They may also be designed to induce nucleation of organic or inorganic three-dimensional (3D) crystals from molecules or ions present in the subphase by a form of epitaxial growth [3]. In this respect they may be used as models for the study of biological mineralization which involves the use of two-dimensional (2D) surfaces of biological macromolecules to induce the mineral crystallization [4]. The design of monolayers with interfaces which mimic the surfaces of 3D crystals also provides a means of examining crystal surface-solvent interactions, for understanding the effect of the solvent on crystal growth. Furthermore, a knowledge of the characteristics of compressed and uncompressed Langmuir monolayers of water-insoluble amphiphiles should help to unravel the packing characteristics at the air-water interface of water-soluble amphiphiles, where even less is known about their 2D arrangements [5]. In addition, Langmuir films are easily transferred to solid supports for the formation of multilayer (Langmuir-Blodgett) films [6], for potential use as piezoelectric sensors [7], soft X-ray monochromators, non-linear optical devices [8] and in molecular electronics [9].

Despite the widespread interest in Langmuir films, many of the methods used to characterize their properties do not give direct information on their crystalline packing arrangements. These methods include measurements of surface pressure versus average molecular area [10], surface potential data [10], non-linear optics from surfaces [11] and IR spectroscopy [12]. Epifluorescence microscopy does furnish some information on crystallinity and morphology on the micron level, but is limited to films of dyes or films containing dye probes [13]. Thus, knowledge on the molecular level of two-dimensional monolayers has been achieved, in the main, from three-dimensional crystals. Indeed, M. Lundquist wrote [14] in a review from 1978: "...there still remains much to be learned especially about the detailed structure of condensed monolayers and regarding the mechanism of molecular rearrangement in monolayer phase transitions. As there are no methods available for direct structure analysis of a monolayer on a water substrate, knowledge of the monolayer structure has, for the most part, been achieved by a sort of translation and application of the knowledge gained from the study of the ordinary three-dimensional state." It is only recently, with the advent of intense and well collimated X-ray beams of variable wavelength from synchrotron sources, that it has become possible to obtain direct structural information on the packing of these films via X-ray surface methods.

Here we shall describe some of these new techniques and the information they provide and review some of the structural results obtained. Emphasis will be placed on monolayer packing arrangements, particularly in terms of the polar head groups. We shall examine self-aggregation, growth and domain size of 2D crystallites, surface pressure- and temperature-driven phase transitions, and the effect of pH, ions and solute molecules in the aqueous subphase on molecular packing and crystallinity. We shall discuss the role played by electrostatic interactions and structural complementarity in the induction of 3D crystal nucleation at the monolayer-solution interface.

The results obtained so far already necessitate a revision of our basic concepts of properties such as crystallinity, phase assignment, diffuse and non-diffuse counter-ionic layers.

2. Experimental

2.1. Specular reflectivity

The colors of a thin oil film on a puddle of water are an every-day experience. The colors come about from interference between light reflected from the oil-air interface and from the oil-water interface. Depending on the oil film thickness and the glancing angle only certain wavelengths, or colors, interfere constructively. This leads naturally to the idea that specular reflection of much shorter wavelength radiation, i.e. X-rays or neutrons, may yield information about the density variation across a Langmuir layer and thus elucidate the structure of such a layer on a microscopic or atomic length scale. Indeed, this intuition turns out to be a fruitful idea to pursue as we shall see in the following.

A side view of a liquid surface reflectometer is shown in the top part of Fig. 1. The incident synchrotron beam is "white". i.e. it has a continuous wavelength spectrum. A monochromatic beam is extracted by Bragg reflection from a single crystal, e.g. the (111) reflection from Germanium. The deflection is in the horizontal plane with the Bragg angle from Ge(111) being typically around 12 degrees, i.e. a deflection angle of 24 degrees. By tilting the monochromator crystal the monochromatic beam can be deflected downwards by an angle α_i towards the liquid surface. A horizontal slit of height h, placed right in front of the trough containing the liquid, limits the footprint of the beam on the liquid surface to be h/α_i. A typical value of h would be 0.10 mm giving a footprint of about 40 mm at $\alpha = \alpha_c^{H_2O} = 2.7$ mrad for a wavelength around 1.5Å. The specularly reflected beam intensity is registered in the detector behind slit S_3. In scanning α_i the footprint slit and the trough height track the beam by means of elevators.

A typical sample cell is shown in the bottom part of Fig. 1. A cannister contains a teflon trough with thermostated subphase water. On top of the water surface is deposited one monolayer of amphiphilic molecules, usually insoluble in water. In order to avoid excitation of long-wavelength, low-frequency surface waves the water depth is made shallow under the X-ray footprint by inserting a glass block — a typical water depth is a few tenths of a millimeter. The teflon trough may contain a barrier (not shown in the figure) so that the available area per molecule can be changed, typically by a factor of five. A Wilhelmy balance monitors the surface pressure of the monolayer.

First we will consider the reflectivity of the bare water surface, which we to begin with consider to be infinitely sharp. We derive the optical laws of Snell and Fresnel for the case of X-rays and neutrons and emphasize the relation between the scattering and absorption properties of a medium on one side and its refractive properties on the other side.

Next, we relax the assumption of an infinitely sharp interface and consider an arbitrary density profile across the the interface from bulk to vapor. That density profile may of course include the Langmuir layer. The reflectivity is modified accordingly and we shall see that the modification is by a factor, which is nothing but the absolute square of the Fourier transform of the density *gradient*.

Having established this general theoretical frame for interpreting reflectivity data, we shall illustrate it by a number of mathematically simple examples which are nevertheless relevant for a number of physical cases such as

- Fuzziness of a simple liquid surface by the thermal excitation of capillary waves
- A thin oil film
- An amphiphilic monolayer.

The arguments presented in Sections 2.1.1–2.1.4 are given in greater detail in [15].

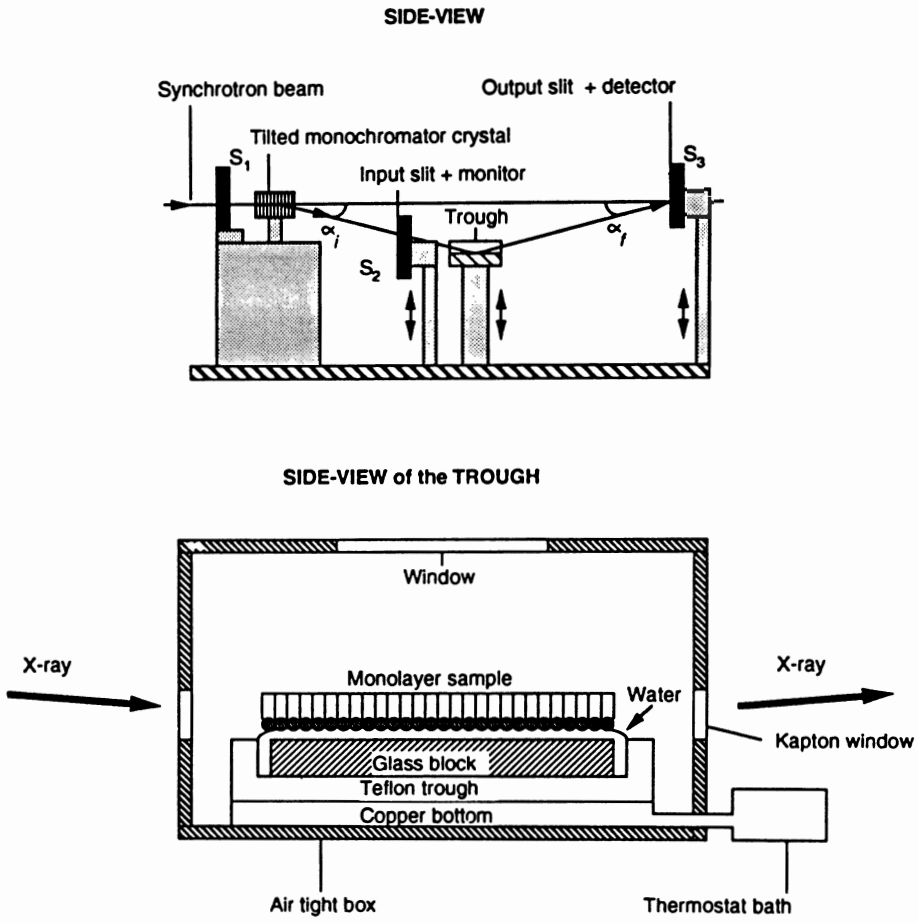

Fig. 1. Example of an experimental set-up of a liquid surface diffractometer (beamline D4, X-ray synchrotron source at Hasylab, Hamburg). Top: Side view of the vertical scattering plane. Beam directions are defined by slits. The monochromatic beam is bent down towards the sample by tilting the monochromator crystal. The incident beam intensity is monitored after slit S2. Bottom: Blown up view of the trough showing the monolayer sample spread on a thin film of water. The glass block provides for a thin liquid film (about 0.3 mm thick) and thus effectively reduces surface waves.

2.1.1. Snell's and Fresnel's laws

In this section we consider the reflection and refraction of a plane wave at a planar interface where the index of refraction changes abruptly from 1 to n, cf. Fig. 2. The three plane waves are all of the form

$$\psi_j = a_j e^{i\mathbf{k}_j \cdot \mathbf{r}}, \qquad j = I, R \text{ or } T \tag{1}$$

and

$$k = |\mathbf{k}_I| = |\mathbf{k}_R| = |\mathbf{k}_T|/n \tag{2}$$

The wavenumber k is related to the wavelength λ by $k = 2\pi/\lambda$. The coefficients a_j are related by the requirement that ψ as well as $\nabla\psi$ must be continuous across the interface:

$$\text{Continuity of } \psi : a_T = a_I + a_R \tag{3}$$

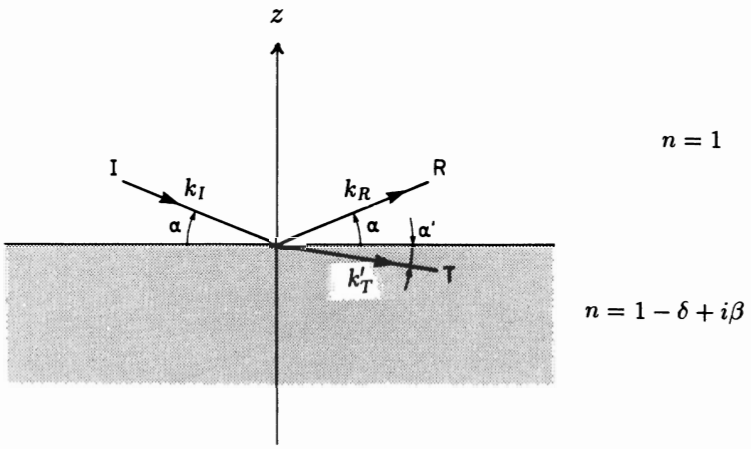

Fig. 2. An incident plane wave (index I) is reflected (index R) and refracted (index T) by a plane interface where the refractive index changes discontinuously from unity at $z > 0$ to n at $z < 0$.

$$\text{Continuity of } \nabla\psi : a_T \boldsymbol{k}_T = a_I \boldsymbol{k}_I + a_R \boldsymbol{k}_R \tag{4}$$

Writing out explicitly the x- and z-components of this vector equation leads to:

$$a_T(nk)\cos\alpha' = a_I k\cos\alpha + a_R k\cos\alpha \tag{5}$$

$$-a_T(nk)\sin\alpha' = -a_I k\sin\alpha + a_R k\sin\alpha \tag{6}$$

Inserting $a_T = a_I + a_R$ then leads to Snell's law

$$n\cos\alpha' = \cos\alpha \tag{7}$$

and

$$(a_I + a_R)n\sin\alpha' = (a_I - a_R)\sin\alpha \tag{8}$$

In the following Section (2.1.2) we shall relate the index of refraction to the scattering and absorption properties of the medium. The results are given in the three last equations (25)–(27), in Section 2.1.2, and we use them here. Since the deviation of n from unity is very small, appreciable refraction will only occur for very small angles. We therefore expand $\cos\alpha$ and $\cos\alpha'$ as $1 - \alpha^2/2$ and $1 - \alpha'^2/2$, respectively. Similarly, $\sin\alpha$ and $\sin\alpha'$ are expanded as α and α', respectively. Furthermore we write

$$n = 1 - \delta + i\beta \equiv 1 \mp \alpha_c^2/2 + i\beta \tag{9}$$

with

$$\alpha_c^2 \equiv (4\pi/k^2)|\rho_{av}| \tag{10}$$

from Eq. (25) and Eq. (26) below.
The minus sign in Eq. (9) applies when $\rho_{av} > 0$ (always the case for X-rays) and the plus sign applies when $\rho_{av} < 0$ (for example for neutron reflection from light water).

We now derive two well-known laws of optics, but applied here to X-rays and neutrons:
Snell's law (from Eq. (7)):

$$(1 \mp \alpha_c^2/2 + i\beta)(1 - \alpha'^2/2) = (1 - \alpha^2/2) \tag{11}$$

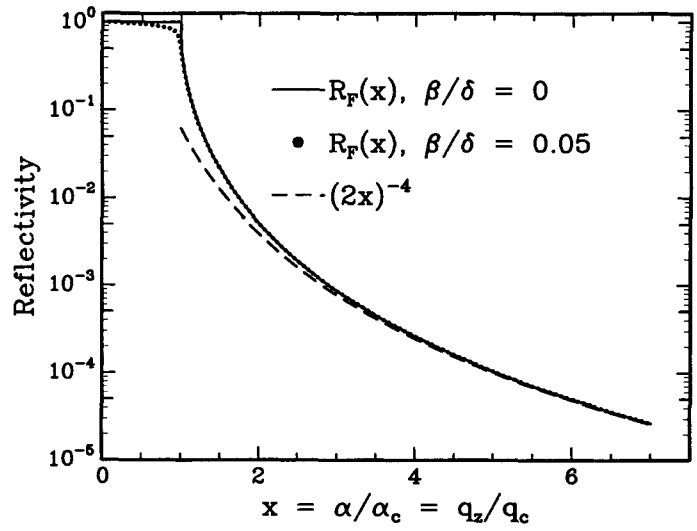

Fig. 3. Reflectivity from a sharp interface versus glancing angle. With no absorption the reflectivity has a kink at the critical angle. The kink is rounded by absorption as shown by the dotted curve. The dashed line is the asymptotic form, cf. Eq. (18).

or

$$\alpha'^2 = \alpha^2 \mp \alpha_c^2 + 2i\beta \tag{12}$$

and Fresnel's law (from Eq. (8) with $n \simeq 1$):

$$(1 + a_R/a_I)\alpha' = (1 - a_R/a_I)\alpha \tag{13}$$

or

$$R \equiv \frac{a_R}{a_I} = \frac{\alpha - \alpha'}{\alpha + \alpha'} \tag{14}$$

The reflectivity, $\mathcal{R}_F$, is the square of the amplitude ratio R:

$$\mathcal{R}_F = \left|\frac{\alpha - \alpha'}{\alpha + \alpha'}\right|^2 \tag{15}$$

the subscript F meaning "Fresnel". The Fresnel reflectivity vs. glancing angle α is shown in Fig. 3. The scale of angle is the critical angle α_c so we plot $\mathcal{R}_F$ versus $x \equiv \alpha/\alpha_c$. Assuming a positive scattering length density ρ_{av} (negative sign in Eq. (9) and in Eq. (12)) and no absorption ($\beta = 0$) Eq. (12) takes the form:

$$x'^2 = x^2 - 1 \tag{16}$$

in terms of $x \equiv \alpha/\alpha_c$ and $x' \equiv \alpha'/\alpha_c$. We see that for $x > 1$, x' is positive and real, but for $x < 1$, x' is purely imaginary. In terms of the quantity

$$a(x) \equiv [|(x^2 - 1)|]^{1/2} \tag{17}$$

we find

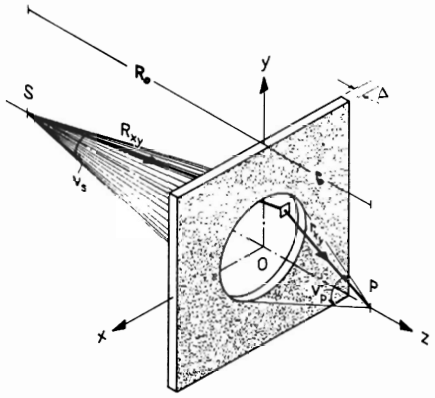

$$v_s, v_p \ll 1,$$

$$R_{xy} \simeq R_0 + \frac{x^2+y^2}{2R_0},$$

$$r_{xy} \simeq r_0 + \frac{x^2+y^2}{2R_0}$$

Fig. 4. When a plane wave traverses a thin plate of thickness Δ and with refractive index n a phase shift of $(nk-k)\Delta$ results after the plate. The plane wave is approximated by a spherical wave from a remote point source S. The incident wave is scattered from all volume elements of the plate having a number density of ρ_n scattering centers, each yielding a scattered spherical wave (only one shown) with amplitude b. The wave function at P is the superposition of the incident spherical wave and all the infinitesimal scattered spherical waves from the plate.

$$x > 1 : \mathcal{R}_F = \left|\frac{x-a(x)}{x+a(x)}\right|^2 \to (1/2x)^4 \qquad \text{for } x \to \infty \tag{18}$$

$$x < 1 : \mathcal{R}_F = \left|\frac{x-ia(x)}{x+ia(x)}\right|^2 = 1 \tag{19}$$

Finite absorption leads to a rounding of the kink at $x = 1$. The dotted curve in Fig. 3 is an example with $\beta/\delta = 2\beta/\alpha_c^2 = 0.05$. The dashed curve represents the simple asymptotic expression $1/(2x)^4$.

2.1.2. *Refraction and scattering*

Next, we derive relations between the refractive index n and scattering and absorption properties.

Two phenomena occur in Fig. 2 when the incident plane wave hits the interface with refractive index n: It changes the direction of propagation (from glancing angle α to α') and it changes wavenumber (from k to nk). We can simplify the discussion by considering *normal* incidence, because according to Eq. (7) there will be no change of propagation direction in that case.

At the interface the normal incident wave $\psi_I = e^{ikz}$ changes to $\psi_T = e^{inkz}$. With n being a complex number, $n = n_r + i\beta$, the wave in the medium becomes $\psi_T = e^{in_r kz}e^{-k\beta z}$, i.e. β is related to the linear absorption coefficient μ (which refers to intensity attenuation, not to amplitude attenuation) by $-2k\beta z = -\mu z$ or

$$\beta = \mu/2k \tag{20}$$

We now for a moment neglect absorption and discuss how the real part of the index of refraction, n_r, is related to the scattering properties of the medium. To this end, consider a thin plate inserted at normal incidence in the plane wave and consider the wave function at a particular point P on the z-axis, see Fig. 4. The wave function at P in the absence of the plate is denoted ψ_P^0. Within the plate of thickness Δ the wavenumber is $n_r k$, as opposed to k outside the plate, so the phase difference at P with and without plate is $(n_r k - k)\Delta$, i.e.

$$\psi_P = \psi_P^0 e^{i(n_r k - k)\Delta} \simeq \psi_P^0 [1 + i(n_r - 1)k\Delta] \tag{21}$$

But we can derive an expression for ψ_P by an alternative consideration involving only scattering processes. The plane wave geometry is almost similar to the point source geometry shown in Fig. 4 if we limit ourselves to large distances between source and plate (R_0) and plate and observation point (r_0).

We then consider the wave function in P as the superposition of the unattenuated spherical wave from the source point $\psi_P^0 = e^{ik(R_0+r_0)}/(R_0 + r_0)$ and all the spherical waves scattered from different volume elements in the plate, ψ_P^s. To derive the latter quantity properly requires some mathematics and the reader is referred to [16] for this derivation. Here we argue for part of the answer: Let us assume a number density ρ_n of identical scattering centers in the plate. The spherical wave from each scattering center has an amplitude b. Clearly then ψ_P^s must be proportional to ρ_n, to b and to the plate thickness Δ and of course also to the source strength and thereby to ψ_P^0. The proportionality factor between ψ_P^s and ψ_P^0 must be dimensionless, but the product of ρ_n, b and Δ has the dimension of inverse length, so the proportionality factor must contain one more physical quantity with the dimension of length. The only remaining possibility is the wavelength λ of the radiation. Therefore the answer must be of the form:

$$\psi_P^s/\psi_P^0 = C\lambda\rho_n b\Delta \tag{22}$$

and the only unknown is the complex number C. In [16] one finds that $C = -i$, so

$$\psi_P = \psi_P^0 [1 - i(2\pi/k)\rho_n b\Delta] \tag{23}$$

and when the two expressions, Eqs. (21) and 23, for ψ_P are identified we conclude that

$$(1 - n_r)k = (2\pi/k)\rho_n b \tag{24}$$

The product of ρ_n and b is the density of scattering length. If we relax the condition that all scattering centers are identical we must substitute the *average* scattering length density ρ_{av} for $\rho_n b$. The final result relating the complex index of refraction to scattering and absorption properties of the medium is then:

$$n = 1 - \delta + i\beta \tag{25}$$

$$\delta = (2\pi/k^2)\rho_{av} \tag{26}$$

$$\beta = \mu/(2k) \tag{27}$$

Inserting numbers for either X-ray scattering or neutron scattering in the expression for δ give numerical values of order 10^{-5}. However, for neutrons the average scattering density may in certain cases be *negative*! whereas it is always positive for X-rays. The reason is the following. X-rays are scattered by the atomic electrons. Each electron is set in vibration by the incident wave field and as an accelerated charge it radiates like a small dipolar antenna. In the far field limit one readily concludes that the radiated field from a free electron is out of phase with the incident field. That accounts for the minus sign in the expression for C. Neutrons, on the other hand, are scattered due to the interaction between the nucleus and the neutron which changes from isotope to isotope and depends also on the relative orientation of the neutron spin and the nuclear spin. The question, whether the

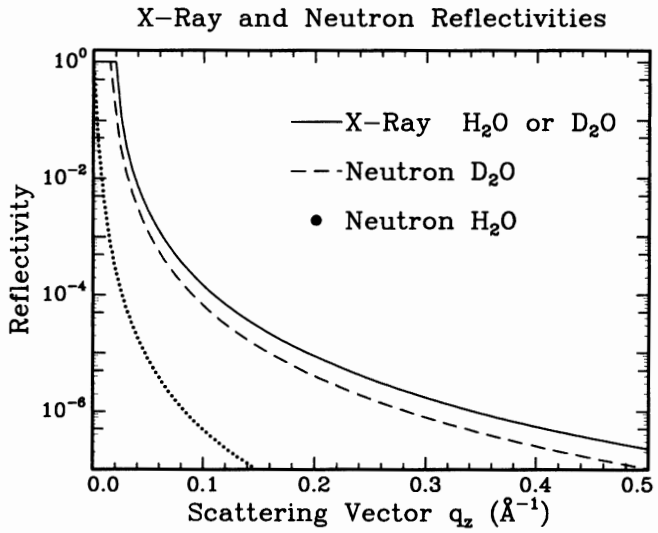

Fig. 5. The reflectivity of water versus the scattering vector $q = 2k\sin\alpha$ for neutrons and X-rays. Notice the enormous difference between reflectivity of light water and heavy water for neutrons.

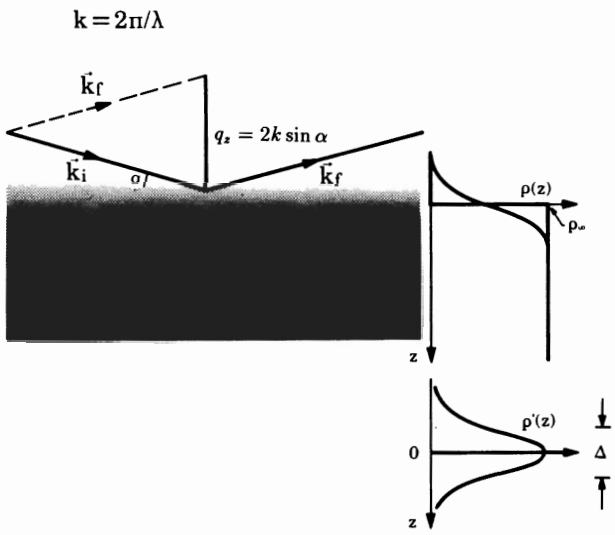

Fig. 6. The density variation across the interface is indicated by the shading in the left part of the figure, and more quantitatively by the normalized scattering density function $\rho(z)$ in the top right hand part and its derivative $\rho'(z)$ below.

scattered wave is in or out of phase with the incident wave, is thus a nuclear property which varies from isotope to isotope. Most isotopes scatter neutrons like electrons scatter X-rays, i.e. out-of-phase, but a few scatter in-phase, the most notable case being the proton. For X-rays the real part of the index of refraction is always less than unity, but for neutrons it is greater than unity for light water and smaller than unity for heavy water. The absorption parameter β is usually much smaller than δ, both for neutrons and X-rays.

Fig. 5 illustrates the reflectivity of X-rays and neutrons from a water surface. Notice that total external reflection does not occur for neutrons on light water - the scattering density of light water is negative! The abscissa is the wave vector transfer in the reflectivity process,

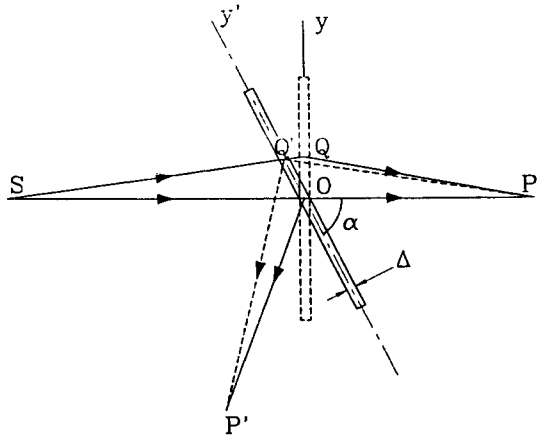

Fig. 7. The reflectivity of a thin sheet is derived by noting that the optical path length $Q'P$ equals the reflected path length $Q'P'$ for arbitrary Q'. Therefore the scattered wave in P' is the same as that in P.

$$q \equiv 2k \sin\alpha. \tag{28}$$

2.1.3. Graded interface

We now consider the case of a fuzzy, flat surface in stead of the sharp, flat Fresnel interface, cf. Fig. 6. The scattering length density[1] $\rho(z)$ has now a profile across the interface, and we shall be concerned in particular with the normalized *gradient* of this profile, $\rho_{av}^{-1} d\rho/dz$. Its Fourier transform is denoted $\phi(q')$ and we shall show (in the Born approximation which is valid in almost all cases of interest in this paper) that the ratio between the actual reflectivity and the ideal Fresnel reflectivity is simply the absolute square of $\phi(q')$:

$$\mathcal{R}(q) = \mathcal{R}_F(q)|\phi(q')|^2 \tag{29}$$

$$\phi(q') \equiv \frac{1}{\rho_{av}} \int \frac{d\rho}{dz} e^{iq'z} dz \tag{30}$$

Note that the exponent in Eq. (30) contains q', the wave vector transfer *inside* the material. This is because in the derivation one superimposes the waves reflected from infinitesimal thin layers at different depths z *inside* the material. According to Eq. (12) with $\beta = 0$, $q' = 2k\alpha'$ is determined by:

$$q'^2 = q^2 - \text{sign}(\rho_{av}) q_c^2 \tag{31}$$

Eq. (29) is obviously correct for a sharp interface since in that case the density gradient is a δ-function and the Fourier transform is unity.

The reflected wave amplitude from an infinitesimal thin sheet can be derived in a way similar to that used in Section 2.1.2, cf. Fig. 4. We merely have to generalize this figure slightly as shown in Fig. 7 so that the thin sheet, in stead of being oriented for normal incidence, is tilted an arbitrary angle. The number of scattering centers per unit area of incoming beam is then changed from $\rho_n \Delta$ to $\rho_n \Delta / \sin\alpha$ and the scattered wave amplitude in P becomes (in analogy to Eq. (22) with $C = -i$)

$$\psi_P^s / \psi_P^0 = -i(2\pi/k)(b\rho_n / \sin\alpha)\Delta \tag{32}$$

[1] With dimension $length^{-2}$ (as opposed to the number density ρ_n with dimension $length^{-3}$)

In Fig. 7 is also shown the mirror point P' of P with respect to the scattering sheet. Clearly the optical path length $Q'P$, from the arbitrary point Q' to the point of observation P, which were integrated over to derive Eq. (22) is identical to the path length $Q'P'$, so the reflected wave amplitude in P' is identical to that in P. The reflectivity *amplitude* ΔR of the thin sheet is therefore

$$\Delta R = -i(2\pi/k)(b\rho_n/\sin\alpha)\Delta \tag{33}$$

This result is almost self-evident: ΔR must vary in proportion to the plate thickness Δ and to the scattering density as seen along the beam, $(b\rho_n/\sin\alpha)$. For dimensional reasons, then, the radiation wavelength $\lambda = 2\pi/k$ must enter linearly. The factor i expresses that the average path length $SQ'P'$ is effectively 1/4 of a wavelength longer than the shortest possible path length SOP'.

Writing

$$\rho(z) \equiv b\rho_n(z) = \rho_{av}(\rho(z)/\rho_{av}) = q_c^2/(16\pi)(\rho(z)/\rho_{av}) \tag{34}$$

where in the second equation we have utilized Eq. (10) together with $q_c \equiv 2k\sin\alpha_c \simeq 2k\alpha_c$, and noting that the term $(2\pi/k)/\sin\alpha$ is equal to $4\pi/q$ we find:

$$i\cdot\Delta R = (2\pi/k)(b\rho_n/\sin\alpha)\Delta = (q_c/2q)^2 q\cdot(\rho(z)/\rho_{av})\cdot\Delta \tag{35}$$

By integrating Eq. (34) ($\Delta \to dz$), we thus obtain the reflectivity of the graded interface:

$$\mathcal{R}(q) = \left(\frac{q_c}{2q}\right)^4 |\phi(q')|^2 \tag{36}$$

with

$$\phi(q') = -iq\int_{-\infty}^{\infty}(\rho(z)/\rho_{av})e^{iq'z}dz \tag{37}$$

Eq. (30) follows by partial integration. Finally, Eq. (29) follows from Eq. (36) by replacing the asymptotic form $(q_c/2q)^4$ by the general form $\mathcal{R}_F(q)$, cf. Fig. 3 and Ref. [17].

The interpretation of reflectivity data becomes complicated if the film density across the surface is not laterally homogeneous. For example, at a certain coverage a solid crystalline phase with reflectivity $|R_1(q)|^2$ may coexist with a liquid or gas phase with reflectivity $|R_2(q)|^2$. If each of the two coexisting phases form macroscopic patches one must merely add the reflected intensities $|R_i(q)|^2$:

$$\mathcal{R}_{incoh}(q) = |R_1(q)|^2 + |R_2(q)|^2 \tag{38}$$

but if the phases are interspersed and the lateral extent of each phase is less than the X-ray coherence length then one obtains the reflectivity by adding amplitudes, not intensities:

$$\mathcal{R}_{coh}(q) = |R_1(q) + R_2(q)|^2 \tag{39}$$

The X-ray coherence length is not laterally isotropic [17]: it is usually quite long along the beam direction, typically of order 10^5Å, but comparatively short perpendicular to this direction, typically of order $10^2 - 10^3$Å. Therefore interpretation of reflectivity data from a heterogeneous film requires knowledge, for example from fluorescence microscopy, of the typical dimension of patches as well

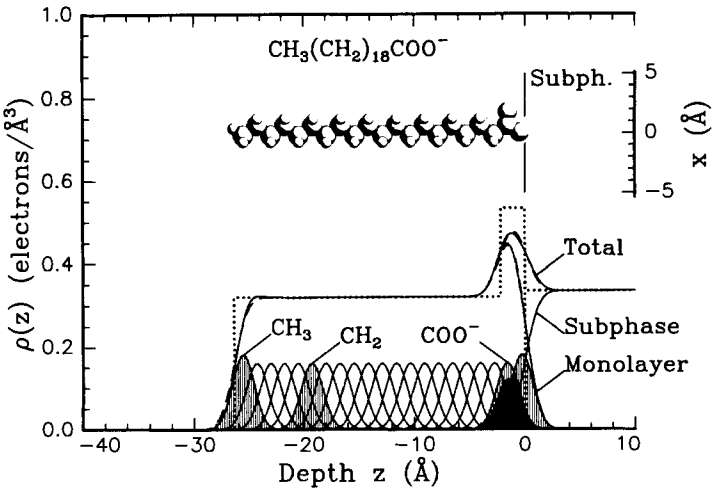

Fig. 8. Top: An amphiphilic molecule at a liquid surface. Bottom: Full lines: The total electron density at the interface is the sum of contributions from the subphase and the monolayer. The monolayer density, in turn, is the sum of contributions from individual atoms of the monolayer molecules. Thermally excited capillary waves lead to an r.m.s. diffuseness σ, and all densities are smeared accordingly. The density may alternatively be described by a two-box model (dotted line) which, smeared by σ (dashed line), agrees well with the profile calculated from contributions from individual atoms (full line).

as the lateral two-dimensional X-ray resolution function. In the case that one phase is crystalline its density variation across the interface may be derived from so-called Bragg-rod profiles which we shall discuss later.

2.1.4. *Model examples*

In this section we give a few examples of calculating the Fourier transform of the normalized density gradient for some model densities. First we remind the reader on some simple but useful properties of Fourier transforms. Let the model density gradient in real space be denoted $f(z)$. We want to calculate its Fourier transform denoted $\phi(q)$. The model density gradient may be broken down into simpler components denoted $g(z), h(z)$, etc. with known Fourier transforms denoted $\phi_g(q), \phi_h(q)$, etc. For example $g(z) = \delta(z)$ has the Fourier transform $\phi_g(q) = 1$, and a Gaussian $h(z) = (\sqrt{2\pi}\sigma)^{-1} e^{-z^2/(2\sigma^2)}$ has a Gaussian Fourier transform $\phi_h(q) = e^{-q^2\sigma^2/2}$. The break down of $f(z)$ may be in terms of superposition:

$$f(z) = g(z) + h(z) + \cdots \Rightarrow \phi(q) = \phi_g(q) + \phi_h(q) + \cdots \tag{40}$$

or it may be in terms of displacement:

$$f(z) = g(z - a) \Rightarrow \phi(q) = \phi_g(q) e^{iqa} \tag{41}$$

or it may in terms of folding:

$$f(z) = \int g(z')h(z - z')dz' \Rightarrow \phi(q) = \phi_g(q)\phi_h(q) \tag{42}$$

Let us now apply these results to some model cases; cf. Fig. 8:

- *A diffuse interface.* An interface is in reality never perfectly sharp. Its fuzziness may be modeled as the smearing of a sharp interface with a Gaussian of r.m.s. width σ. According to the folding

theorem above $\phi(q) = e^{-q^2\sigma^2/2}$ and the reflectivity relative to the Fresnel reflectivity is simply $e^{-q^2\sigma^2}$. It has been shown [18] that the air- liquid interface of simple liquids like water, ethanol etc. is well accounted for by this model, and that the smearing is entirely dominated by thermally excited capillary waves.

- *A homogeneous film.* A film of thickness L and with a scattering density of b relative to that of the substrate is modeled by a box of height b between $z = -L/2$ and $z = +L/2$ plus a box of unit height from $z = +L/2$ extending to infinity. According to the displacement theorem, the latter has a Fourier transform $e^{iqL/2}$ whereas the first is the sum of $e^{-iqL/2}$ from the first edge and $-e^{+iqL/2}$ from the second edge, both multiplied by the box height b, so altogether:

$$|\phi(q)|^2 = |e^{iqL/2} - b(2i)\sin(qL/2)|^2 = |1 - b + b\cdot e^{-iqL}|^2 \tag{43}$$

If both edges are smeared by the same Gaussian this expression for $|\phi(q)|^2$ must be multiplied by $e^{-q^2\sigma^2}$.

- *An amphiphilic monolayer.* The amphiphilic molecule is modeled by a tail part and a head group part. The tail part with a normalized scattering density of b_t is located between $z = -l - L/2$ and $z = -L/2$, whereas the head group part with a scattering density of b_h is located between $z = -L/2$ and $z = L/2$. The latter part is the same as the one-box model considered above and from the displacement theorem we can immediately write down

$$|\phi(q)|^2 = |e^{iqL/2} - b_h(2i)\sin(qL/2) - b_t(2i)\sin(ql/2)e^{-iq(L+l)/2}|^2 \tag{44}$$

If, as is frequently the case for compressed hydrocarbon tails, $b_t \simeq 1$, then Eq. (44) reduces to

$$|\phi(q)|^2 \simeq |e^{-iq(L/2+l)} - 2i\,(b_h - 1)\sin(qL/2)|^2, \tag{45}$$

for which the position of the first minimum is given [17,19] by $q_{\min} = \frac{3}{2}\pi/(L/2 + l)$. If all three edges are smeared by the same Gaussian the expressions (44,45) should be multiplied by $e^{-q^2\sigma^2}$. Daillant et al. [20,21] have studied the variation of σ with surface pressure in an amphiphilic monolayer ($C_{19}CO_2H$, cf. Table 1 below). They found that σ, the r. m. s. fuzziness generated by capillary waves, is given at low surface pressures by the surface tension, but that above a certain threshold pressure the monolayer aquires a significant stiffness against bending, resulting in a 20 per cent drop in σ.

Further examples of physically relevant model densities may be found in [22].

2.2. *Grazing incidence diffraction – GID*

2.2.1. *Evanescent wave*

We now consider in-plane diffraction. The incident beam is at a fixed glancing angle α which is usually smaller than the critical angle α_c for total external reflection. The plane wave inside the material has wave vector $(k'_x, k'_z) = nk(\cos\alpha', \sin\alpha')$ and thus factorizes into a plane wave propagating laterally times a 'wave' with wave vector $k'_z \cong k\alpha'$. According to Snell's law (Eq. (12)), neglecting absorption and for the sake of argument assuming that $\alpha \ll \alpha_c$, α' becomes purely imaginary, $\alpha' = i\alpha_c$ and consequently $k'_z = iq_c/2$, i.e. the laterally propagating plane wave inside the material has an exponentially damped amplitude along the inward surface normal with decay length $2/q_c$. Since the intensity is the square of the amplitude, its decay length $\Lambda_0 = 1/q_c$, independent of

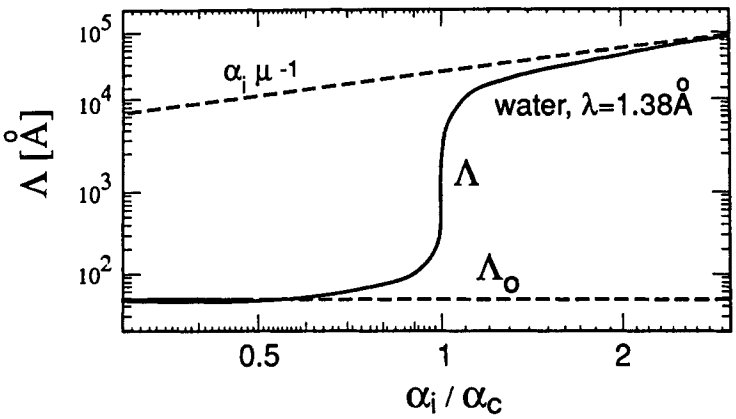

Fig. 9. X-ray penetration depth Λ in water at a wavelength λ=1.38 Å versus the incident glancing angle α relative to the critical angle α_c for total external reflection. The two asymptotes and the value at $\alpha = \alpha_c$ are derived in the text.

α as long as $\alpha \ll \alpha_c$, the latter condition being indicated by the subscript $_0$. For a water surface, using the expression for q_c, one finds that this evanescent wave only penetrates about 5nm so in this particular geometry X-rays have been made surface sensitive! In the opposite limit, $\alpha \gg \alpha_c$, the intensity decay length $\Lambda_\infty(\alpha)$ normal to the interface is determined by the linear absorption coefficient μ. At depth $\Lambda_\infty(\alpha)$ the incident ray has traversed a length $\Lambda_\infty(\alpha)/\alpha$ in the medium, so $\Lambda_\infty(\alpha)$ is determined by $(\Lambda_\infty(\alpha)/\alpha)\mu = 1$ or

$$\Lambda_\infty(\alpha) = \mu^{-1}\alpha \tag{46}$$

The slope μ^{-1} varies approximately in proportion to the cube of the X-ray wavelength. In Fig. 9 it is shown for $\lambda = 1.38$ Å.

Between these two limits, Λ_o and $\Lambda_\infty(\alpha)$, the decay length $\Lambda = \Lambda_c$ at $\alpha = \alpha_c$ is derived from Eq. (12):

$$\alpha'^2 = 2i\beta = 2i(\mu/2k) = i(\mu/k) \tag{47}$$

or

$$\alpha' = \sqrt{\mu/(2k)}(1+i) \tag{48}$$

so

$$\Lambda_c^{-1} = 2kIm(\alpha') = 2\sqrt{\mu k/2} \tag{49}$$

or

$$\Lambda_c = (2\mu k)^{-1/2} = \left(\frac{\alpha_c}{\mu}\frac{1}{2k\alpha_c}\right)^{1/2} = (\Lambda_\infty(\alpha = \alpha_c)\cdot\Lambda_0)^{1/2} \tag{50}$$

i.e. Λ_c is the geometric mean of the two asymptotes extrapolated to $\alpha = \alpha_c$.

So much for the depth variation of the evanescent wave.

What is its intensity just below the interface and how does it vary with incident glancing angle? As usual the intensity is the square of the amplitude $T(\alpha) \equiv T(\alpha, z = 0)$ just below the interface, and $T(\alpha)$ is derived from Eq. (14) utilizing

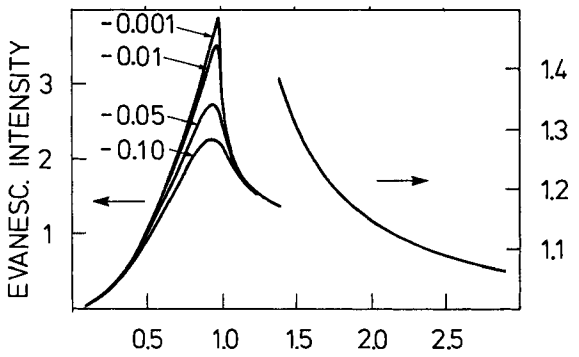

Fig. 10. The evanescent wave intensity at the interface versus incident glancing angle, for various values of the dimensionless absorption parameter $b \equiv -(2\mu k/Q_c^2) = -\frac{1}{2}\beta/\delta$.

$$1 + R(\alpha) = T(\alpha) \tag{51}$$

or

$$T(\alpha) = \frac{2\alpha}{\alpha + \alpha'} \tag{52}$$

As above we consider first three cases, and for simplicity take $\beta = 0$:

$$\alpha \ll \alpha_c; \quad \alpha' \to i\alpha_c; \quad T(\alpha) \to 0 \tag{53}$$

$$\alpha = \alpha_c; \quad \alpha' = 0; \quad T(\alpha) = 2 \tag{54}$$

$$\alpha \gg \alpha_c; \quad \alpha' \to \alpha; \quad T(\alpha) \to 1 \tag{55}$$

It is straightforward to derive $T(\alpha)$ explicitly in the same manner. In terms of $x = \alpha/\alpha_c$:

$$T(\alpha) = 2x \qquad \text{for } 0 < x < 1 \tag{56}$$

$$T(\alpha) = \frac{2x}{x + \sqrt{(x^2 - 1)}} \qquad \text{for } x > 1 \tag{57}$$

We interpret these results as follows. The evanescent wave amplitude $T(\alpha, z = 0)$ results from the interference from the incident wave and the reflected wave. Below the critical angle for total external reflection these waves are of equal strength, and for $\alpha = \alpha_c$ they are in phase so the evanescent wave amplitude is twice that of the incident wave amplitude and its intensity is four times that of the incident beam. As α becomes less than α_c the two waves get more and more out of phase and when $\alpha \ll \alpha_c$ they are in antiphase and the evanescent wave vanishes. For $\alpha \gg \alpha_c$ the reflected wave amplitude vanishes and the evanescent wave amplitude approaches that of the incident wave. The effect of finite absorption is to smear the kink at $\alpha = \alpha_c$ and thereby diminish the amplification of the evanescent wave below two (four) in amplitude (intensity). Quantitative curves for $|T(\alpha)|^2$ for $\beta = 0$ as well as for $\beta > 0$ given in Fig. 10.

The evanescent or transmitted wave may be utilized [23,24] to excite the fluorescence of ions attracted to the surface by the charged polar head groups of the amphiphilic monolayer, e. g., COO^- in Fig. 8. With the beam incident at an angle α_i, the fluorescent yield observed at an exit angle α_f from the surface will be proportional to $\int dz N(z)|T(\alpha_i, z)|^2|T'(\alpha_f, z)|^2$, $T(\alpha_i, z)$ being the

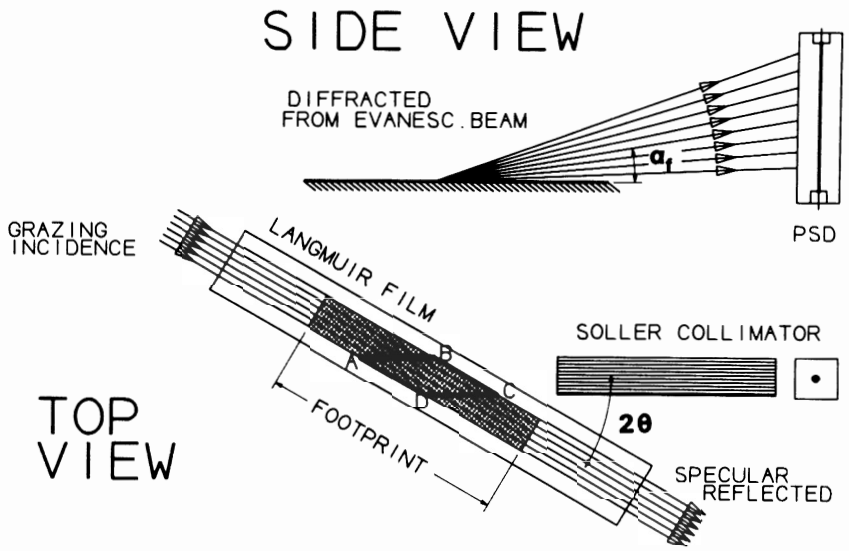

Fig. 11. Top and side views of GID geometry. The footprint of the incident beam is indicated by the darker area. The position sensitive detector (PSD) has its axis vertical. Only the cross-beam area ABCD contributes to scattering. The Soller collimator consists of thin vertical absorbing foils stacked together with appropriate spacing to define the horizontal resolution of the detector.

evanescent or transmitted field amplitude at a depth z and $T'(\alpha_f, z)$ being the analogous function describing how the fluorescence (of a modified wavelength λ') exits from the interface [25].

A more complete analysis [26] may then consist of first obtaining an electron density profile $\rho(z)$ from the measured reflectivity, use this profile to calculate the field amplitude $T(\alpha_i, z)$ by means of optics for stratified media (e.g., [27]), derive the ion density profile $N(z)$ from data for the fluorescent yield *vs.* α_i or *vs.* α_f, and refine the analysis of the reflectivity data including the ion concentration profile.

In a grazing incidence diffraction (GID) experiment the evanescent wave is diffracted by lateral two-dimensional order in the monolayer. If the order is crystalline the evanescent wave may be Bragg scattered from a grain which is oriented so its h, k lattice "planes" make an angle θ_{hk} with the evanescent beam fulfilling the Bragg condition $\lambda = 2d_{hk} \sin\theta_{hk}$. There is no restriction on the z-component of the Bragg scattered beam — the Bragg scattered ray may go deeper into the liquid or it may go out of the liquid at an exit angle $\alpha_f > 0$. In short: a two-dimensional lattice confines the scattering vector to Bragg *rods* - not Bragg *points* as for a 3D crystal. Consider now the variation of intensity with exit angle α_f near α_c. The Bragg scattered ray with $\alpha_f = -\alpha_c$ will be totally reflected by the interface and will interfere constructively with the Bragg scattered ray with $\alpha_f = +\alpha_c$. The exit beam will therefore have a maximum at $\alpha_f = +\alpha_c$ and the peak will be of the same shape as that given in Fig. 10 but now versus α_f/α_c. Hence, analogous to the fluorescent yield discussed above, the diffracted signal will contain both the factors $|T(\alpha_i, z \simeq 0)|^2$ and $|T(\alpha_f, z \simeq 0)|^2$.

2.2.2. *Bragg rod profile*

Fig. 11 shows in more detail the geometry for in-plane diffraction. The grazing incidence beam illuminates a certain footprint of the surface. A Soller collimator can transmit X-ray photons from part of this footprint if they are diffracted a lateral angle of 2θ and within a fan of vertical angles α_f from

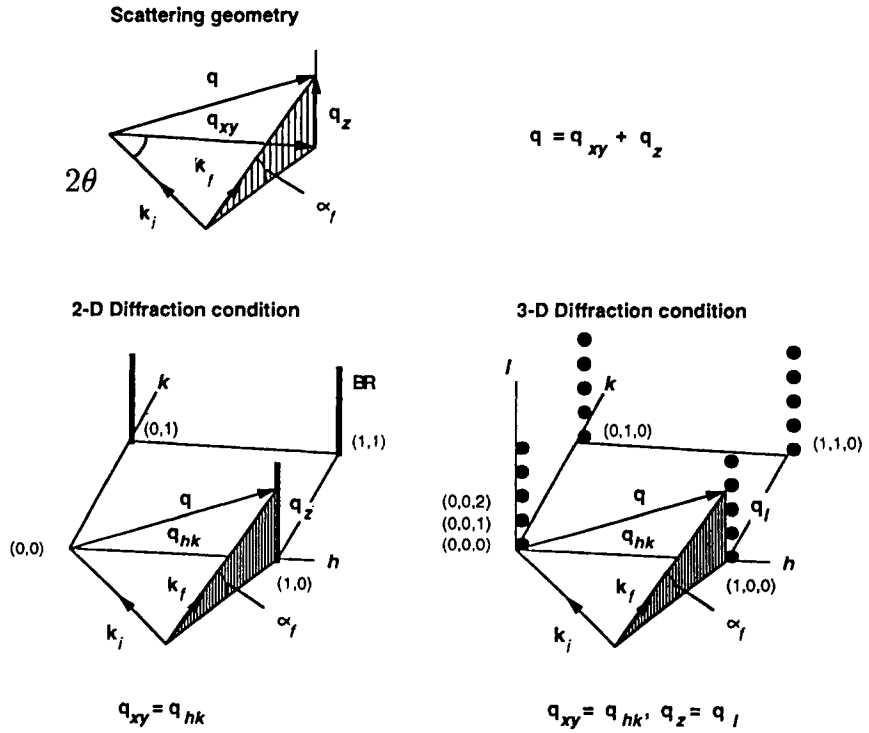

Fig. 12. The top part of the figure shows the general scattering geometry. k_i and k_f are the wave vectors of the incident and diffracted beams respectively. The scattering vector $q = k_f - k_i$ has components $|q_{xy}| \simeq 2k \sin\theta$ parallel to the monolayer plane and $q_z = k \sin\alpha_f$ perpendicular to it. The bottom right figure shows that the scattering from a 3D crystal occurs at the reciprocal lattice points (h, k, l) in reciprocal space (q-space). Diffraction takes place when q coincides with a reciprocal lattice point, (1,0,3) in this particular case. The bottom left figure shows that in reciprocal space, the scattering from a 2D crystal extends in rods (Bragg Rods) in the q_z direction, perpendicular to the plane of the monolayer and to its reciprocal 2D net. The scattering vector q must end on an (h, k) Bragg Rod for Bragg diffraction.

the horizon and up to a practical upper limit of around 10°. The vertical angle α_f is determined by a position sensitive detector aligned vertically. In this geometry one thus determines the lateral (q_{xy}) as well as the vertical (q_z) components of the scattering vector. Assume now that the amphiphilic monolayer has two-dimensional (quasi) long range order. This implies that for appreciable scattering to take place q_{xy} must coincide with a reciprocal lattice vector q_{hk} with integer coordinates (h, k) and length $(4\pi/\lambda) \sin\theta_{hk}$. For all the diffraction patterns measured so far, the monolayers were found to be composed of 2D crystallites randomly oriented on the water surface: a 2D "powder". Hence there will always be a crystallite grain with reciprocal lattice vector q_{hk} coinciding with q_{xy} in the crossed beam area of the footprint. There is no selection rule on q_z but the intensity along the (h, k) Bragg rod is modulated with the square of the molecular formfactor, cf. lower part of Fig. 12. The form factor of a rod or of a cigar shaped molecule is a disc perpendicular to the molecular axis. Assume first that the rod-like molecules are perpendicular to the surface. The intensity along any Bragg rod will then have its maximum at the horizon, cf. Fig. 13a. Next, assume that the molecules are tilted around a horizontal axis. In a specific example illustrating the point, let us assume that the unit cell is rectangular and that the molecular rotation axis is along $(0, k)$. In that case the intercept between the molecular formfactor disc will still have its maximum at the horizon for $(0, k)$ reflections, but for the (h, k) reflections $(h \neq 0)$ the maximum occurs at the intercept of the tilted disc and the (h, k)

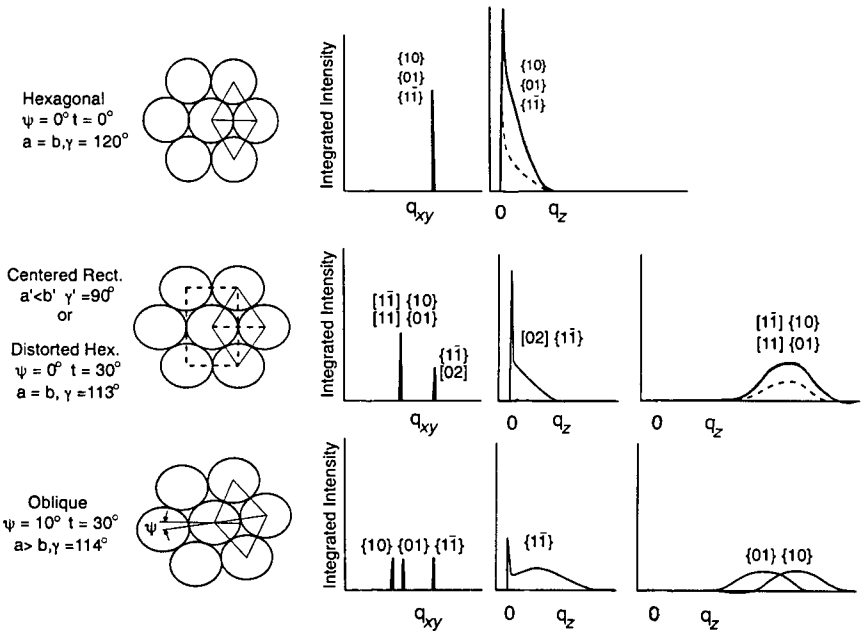

Fig. 13. Three possible structures and diffraction from a monolayer of close-packed alkyl chains. For simplicity, we assume the chains to be in the "free rotator phase", i.e. they exhibit cylindrical symmetry. The middle column shows the q_{xy}-pattern integrated over the vertical wave vector component q_z, and the right column shows the Bragg rod integrated over the corresponding q_{xy}. Here, the dashed lines represent the intensity from individual reflections as indicated by the Miller indices. The full line represents the intensity from a two-dimensional powder sample; i.e. the sum of the intensities indicated by dashed lines. When the cylinder axis is perpendicular to the water surface the lattice is hexagonal (top row), and the $\{1,0\}$, $\{0,1\}$ and $\{1,\bar{1}\}$ reflections are degenerate. The Bragg rod obtained from the single in-plane diffraction peak has its maximum at $q_z = 0$ Å^{-1}. When the cylinder axis is tilted towards nearest neighbors (middle row), the hexagonal structure is distorted to a centered rectangular structure. The degeneracy of the three reflections is partially lifted resulting in two peaks. One comprises two degenerate reflections and the other is a singlet. The Bragg rod of the two degenerate reflections $\{1,0\}_h$ and $\{0,1\}_h$ ($[1,1]_r$, $[1,\bar{1}]_r$ in the rectangular notation) is centered at $q_z \geq 0$ Å^{-1}, the position of the center depending upon the extent of the molecular tilt. The singlet corresponds to the $\{1,\bar{1}\}_h$ reflection ($[0,2]_r$ in the rectangular notation). Its Bragg rod is still centered around $q_z = 0$ Å^{-1}. Finally, when the molecular axis is tilted in a non-symmetry direction, the intersection between the close-packed circular chains and the water surface forms an oblique 2D lattice (bottom row). The degeneracy is completely lifted. In all three cases, the peak positions of the Bragg rod(s) unambiguously determine both the tilt angle and the azimuthal angle ψ.

Bragg rod, cf. Fig. 13b. We conclude from this example that from the intensity distribution along Bragg rods one can find both the tilt angle and the tilt direction of the molecules. If the molecules do not have rotational symmetry around the molecular axis, the intensity in different Bragg rods (h, k) will be modified accordingly.

In-plane diffraction experiments with the capability of measuring the Bragg rod intensity modulation is thus a very powerful method for determining the detailed molecular structure of the Langmuir layer.

3. General packing characteristics of Langmuir monolayers on water

Before the development of surface X-ray diffraction techniques, knowledge of molecular arrangement in the three-dimensional state was used to increase understanding of the structure and behavior

Table 1
Chemical formulae of monolayer compounds

Abbreviated name	Full name and chemical formula
C_nOH	Aliphatic primary alcohols $C_nH_{2n+1}OH$
$C_{19}CO_2C_nOH$	*n*-hydroxy-nonyl-eicosanoate $C_{19}H_{39}CO_2C_nH_{2n}OH$
C_nCO_2H	Aliphatic primary acids $C_nH_{2n+1}CO_2H$
$C_{18}OC_6H_4\text{-}CO_2H$	*p*-octadecyl-oxybenzoic acid $C_{18}H_{37}O\text{-}C_6H_4\text{-}CO_2H$
C_nCONH_2	Aliphatic primary amides $C_nH_{2n+1}CONH_2$
$C_{19}CONHC_2H_4CO_2H$	N-arachidoyl-β-alanine $C_{19}H_{39}CONHC_2H_4CO_2H$
Dimyristoyl-phosphatidylethanolamine DMPE	$C_{13}H_{27}COOCH_2$ | $C_{13}H_{27}COOCHCH_2PO_4^-C_2H_4NH_3^+$
PL	Palmityol-lysine $C_{15}H_{31}CONHC_4H_8CHNH_3^+CO_2^-$
PFA	1H,1H,2H,2H-perfluorododecyl-aspartate $C_{10}F_{21}C_2H_4OCOCH_2CHNH_3^+CO_2^-$

of molecules in the monolayer state, as already mentioned in the Introduction. Analogous packing is not always possible however, because of environmental differences between the two- and three-dimensional states. Phase diagrams constructed from surface pressure-area (π-A) measurements for such compounds revealed phase boundaries, depending upon the pressure, temperature and chain length, but could provide little information on the structure of these phases. Now, with the recently acquired information from surface-sensitive X-ray techniques, packing of such Langmuir films can be determined almost at the atomic level. Although GID measurements have been carried out on several Langmuir monolayer systems, the monolayer structures corresponding to the complete phase diagrams have been elucidated by GID only for the acids $C_{20}CO_2H$ and $C_{21}CO_2H$, discussed in Section 3.2. Here, we will describe one or two examples from each chemical class studied to date: alcohols, amides, carboxylic acids, divalent salts of the latter, α-amino acids and phospholipids (see Table 1 for their chemical formulae and abbreviated names). The latter two classes of compounds possess an asymmetric carbon atom whose chirality is specified by the symbol (R) or (S).

It is useful at this stage to describe how the unit cell dimensions and molecular orientation may be determined from the GID data for simple cases. We consider the molecule as a freely rotating alkane chain, *i.e.* it has cylindrical symmetry. These molecules may pack in three different cells: hexagonal ($a = b, \gamma = 120°$), distorted-hexagonal ($a = b, \gamma \neq 120°$) which may be more properly described as

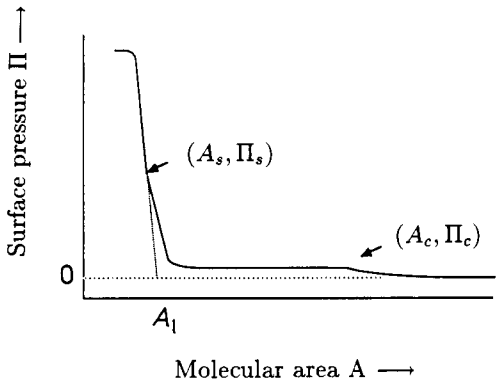

Fig. 14. A surface pressure versus area isotherm of an imaginary Langmuir monolayer. A_ℓ is defined as the limiting area, i.e., the close-packed area for the molecules at zero pressure. (A_s, π_s) and (A_c, π_c) define areas and pressures for transitions between phases.

centered rectangular ($a' = |\mathbf{a} + \mathbf{b}|, b' = |\mathbf{a} - \mathbf{b}|$) and oblique ($a \neq b \neq |\mathbf{a} + \mathbf{b}|$). They are shown in Fig. 13. The molecules in a hexagonal cell are aligned vertically, in the distorted hexagonal cell the molecules are tilted along a symmetry direction and in the oblique cell the molecules are tilted along an arbitrary direction. As mentioned earlier, all Langmuir monolayers studied to date by GID consist of "powders" of randomly ordered 2D crystallites on the water surface so that the GID measurements are not made on single crystals. Thus, the diffraction patterns consist of coinciding Bragg rods of reflections (h, k, q_z) and $(\bar{h}, \bar{k}, q_z)$. In general, the intensity distribution along their two coinciding Bragg rods will be different unless the monolayer structure has a twofold symmetry along the vertical axis.

The hexagonal cell has three equivalent lattice spacings d_{hk} : d_{10}, d_{01} and $d_{1\bar{1}}$. The GID pattern from these three reflections will appear as a single peak with all corresponding Bragg rods peaking at $q_z = 0$ Å^{-1} (top row of Fig. 13). The corresponding GID pattern for the distorted-hexagonal cell will comprise two peaks; one a superimposed doublet arising from the coinciding {1,0} and {0,1} reflections, and the remaining $\{1, \bar{1}\}$ peak (middle row of Fig. 13). The separation between the two peaks depends upon the deviation of the angle γ from 120°. In the oblique cell the degree to which the three peaks {1,0}, {0,1} and $\{1, \bar{1}\}$ are resolved (bottom of Fig. 13), depends upon the deviation from centered rectangular (*i.e.*, distorted hexagonal) cell symmetry.

3.1. Phase changes induced by surface pressure

A typical pressure-area isotherm of Langmuir films at room temperature is shown in Fig. 14. It has long been realized that the "kinks" in the isotherm (the surface pressures at the kinks are designated π_c and π_s) indicate phase transitions [10]. The shape of the isotherm and the positions of the "kinks" are characteristics of a given monolayer. At room temperature, the alcohol $C_{21}OH$ and the acid $C_{20}CO_2H$ as well as the α-amino acid PFA exhibit isotherms with only one distinct "kink" at π_s (in the range 15-30 mN/m) whereas the phospholipid compound DMPE has an isotherm with two kinks (π_c in the range 5-10 mN/m and π_s in the range 20-30 mN/m). The α-amino acid PL shows no observable "kink". It has generally been assumed that a decrease in molecular-area induces transitions from gaseous to "liquid-expanded" to "liquid-condensed" to the solid crystalline phases

[10]. But the GID data on several systems reveal high crystallinity in the uncompressed state and sometimes a tendency towards a reduction of crystallinity with increased pressure. Thus, the GID and XR results may provide a more accurate description of the phases. However, if the crystalline solid phase is in coexistence with a disordered phase, it can be difficult to determine the fraction of molecules which are part of the crystalline phase. Further, no information can be gained on the molecules in the disordered phase.

3.1.1. *Fatty acids and alcohols*

GID data for heneicosanol [28] $C_{21}OH$ show a single peak in the surface pressure-temperature range 15-30 mN/m - 15-30°C. The changes in the peak with pressure observed at 24.6°C are shown in Fig. 15 and are typical of the isotherms measured. The gradual loss of intensity below π_s was interpreted [28] as being due to the appearance of gauche defects in the hydrocarbon chain. The kink would then represent the lowest pressure at which the last of the gauche configurations are squeezed out. Above the kink, all the molecules would stand straight with their hydrophobic tails in all-*trans* conformation. However, more recent results [29] indicate that the loss of intensity was due instead to the molecules tilting uniformly towards their next nearest neighbors, causing the diffraction signal to move away from the horizon ($q_z = 0$), cf. Fig. 13, hence out of the detector's aperture.

Combined GID, Bragg rod and XR room temperature measurements on arachidic acid [17,30,31] $C_{19}CO_2H$ along the isotherm (Fig. 16) have been interpreted differently; the drop in GID intensity as a function of decreasing surface pressure was accounted for by a continuous change in tilt of rigid parallel molecules toward their *nearest* neighbors.

The high pressure phase corresponds to a 2D structure with molecules which are aligned perpendicular to the surface in a hexagonal cell. The low pressure structure was assigned to a distorted hexagonal cell, with molecules tilting towards nearest neighbors. Such a cell yields two diffraction peaks, one corresponding to the $\{1,\bar{1}\}$ reflection and the other to $\{1,0\}$ and $\{0,1\}$.

Recently, the phase diagrams of heneicosanoic acid ($C_{20}CO_2H$) [32] and behenic acid ($C_{21}CO_2H$) [33] at the air-water interface were studied by GID. It was reported that at high surface pressure the molecules are essentially perpendicular to the water surface and that at intermediate surface pressure two distinct distorted hexagonal structures with tilted molecules were observed. A more detailed description of all the phases will be given in Section 3.2.

The GID and XR results on $C_{19}CO_2H$ over pure water allows us to deduce some information on the packing of the carboxyl groups in the compressed ordered state at room temperature. The hexagonal cell may at first sight imply complete rotational disorder about the chain axis and consequently that the structure possesses hexagonal symmetry. Indeed, such structural disorder may be possible for the alcohol $C_{21}OH$. However, aliphatic carboxylic acids can hardly support such disorder for it could lead to a short intermolecular contact $d_{O\ldots O}$ of about 1.5 Å between two neighboring oxygen atoms with their lone pair electrons directed at each other as shown in Fig. 17. Numerous studies [34] have demonstrated that two such neighboring oxygen atoms have a preferred separation of 3.5 Å. A six-fold disorder would lead to a short $d_{O\ldots O}$ contact and is thus impossible; only a three-fold disorder is acceptable. Thus, the hindered rotation of the acid molecules precludes hexagonal symmetry. Yet, the hexagonal character of the unit cell may reflect a trigonal symmetry of the crystalline phase.

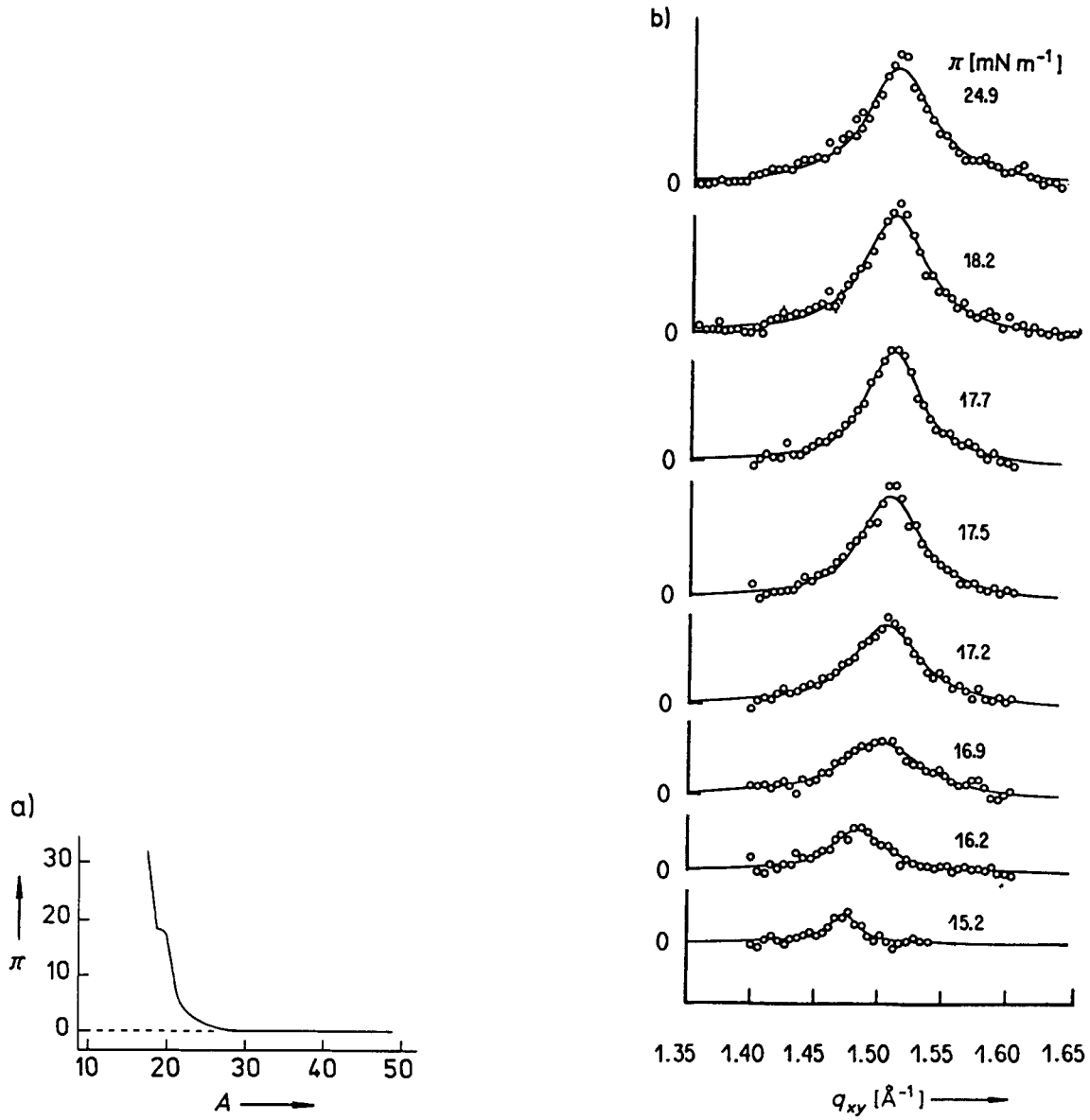

Fig. 15. The alcohol $C_{21}OH$ monolayer at 25°C: (a) Surface pressure-area isotherm over pure water. (b) GID data along the isotherm, a linear background has been subtracted (data taken from Ref. [28]).

3.1.2. Phospholipids

There have been extensive surface X-ray [35–41] and neutron [42,43] studies done on phospholipid monolayers. Part of this work has been reviewed in detail in terms of structural changes along the π-A isotherm [16].

The isotherm of dimyristoylphosphatidylethanolamine (DMPE) is shown in Fig. 18a. X-ray GID measurements with a detector accepting only q_z close to the horizon [38,16] yielded a single peak in the pressure range from 10 to 38 mN/m. The variation with surface pressure of the diffraction peak characteristics is depicted in Fig. 18b. The diffraction data for $\pi_c < \pi < \pi_s$ is consistent with coexistence between a non-diffracting liquid phase and a "gel" phase with a coherence length, L,

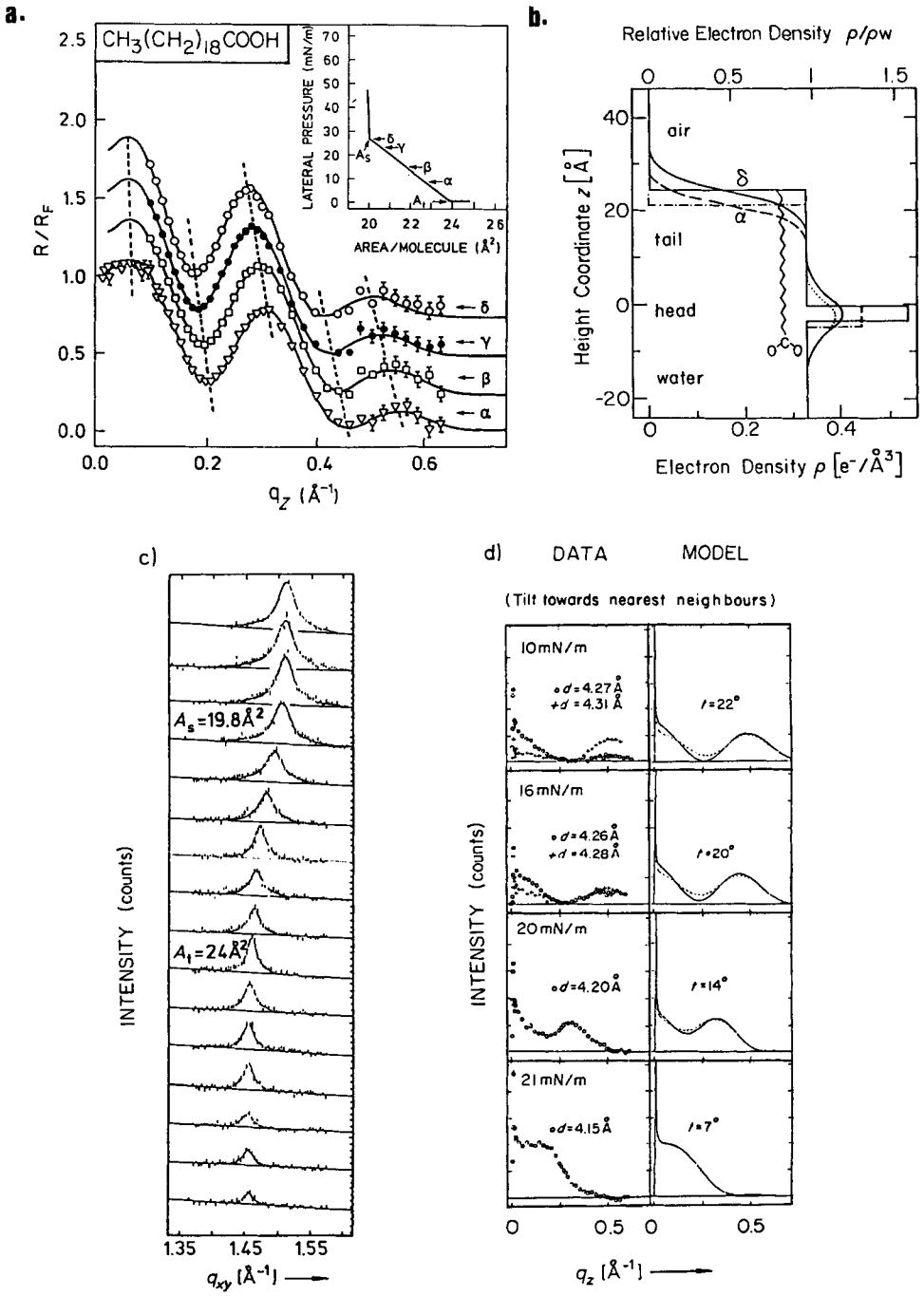

Fig. 16. Arachidic acid $C_{19}CO_2H$ monolayer at room temperature and over pure water: (a) Normalized X-ray reflectivity (XR) data for increasing surface pressure ($\alpha - \delta$). The insert shows the surface pressure-area isotherm of the monolayer and indicates the points were the XR measurements were performed. (b) Fitted model of the vertical electron density $\rho(z)$. On compression, the monolayer thickness increases while the density remains constant in the tail region as shown by the change from the dashed lines to the full lines. (c) GID data for decreasing mean molecular area, A_s and A_f correspond to the areas marked on the pressure-area diagram. (d) Left: 2D powder Bragg rods observed at surface pressures of 10, 16, 20 and 21 mN/m. At 20 and 21 mN/m, the optimal q_{xy} settings for the merging peaks at $q_z = 0$ Å^{-1} and $q_z > 0$ Å^{-1} coincide, but for lower surface pressures they split as indicated by open circles (optimum q_{xy} for $q_z = 0$ Å^{-1}) and crosses (optimum q_{xy} for $q_z = 0.5$ Å^{-1}). Right: Calculated Bragg rod profiles from a slab model in which the molecules tilt towards next nearest neighbors. The model parameters were essentially determined from the reflectivity data. The dashed line represents a perturbation of this model in that molecules were tilted in a direction 8° from the symmetry direction.

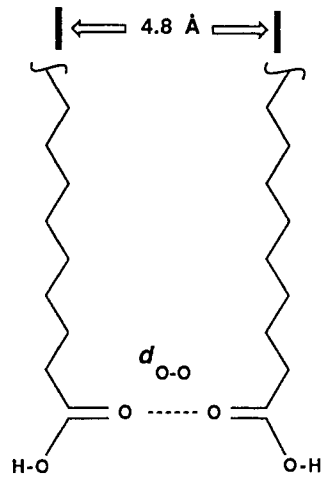

Fig. 17. Close contact ($d_{O\cdots O}$ spacing) between neighboring oxygen atoms of two fatty acid molecules separated by 4.8 Å and related by twofold symmetry.

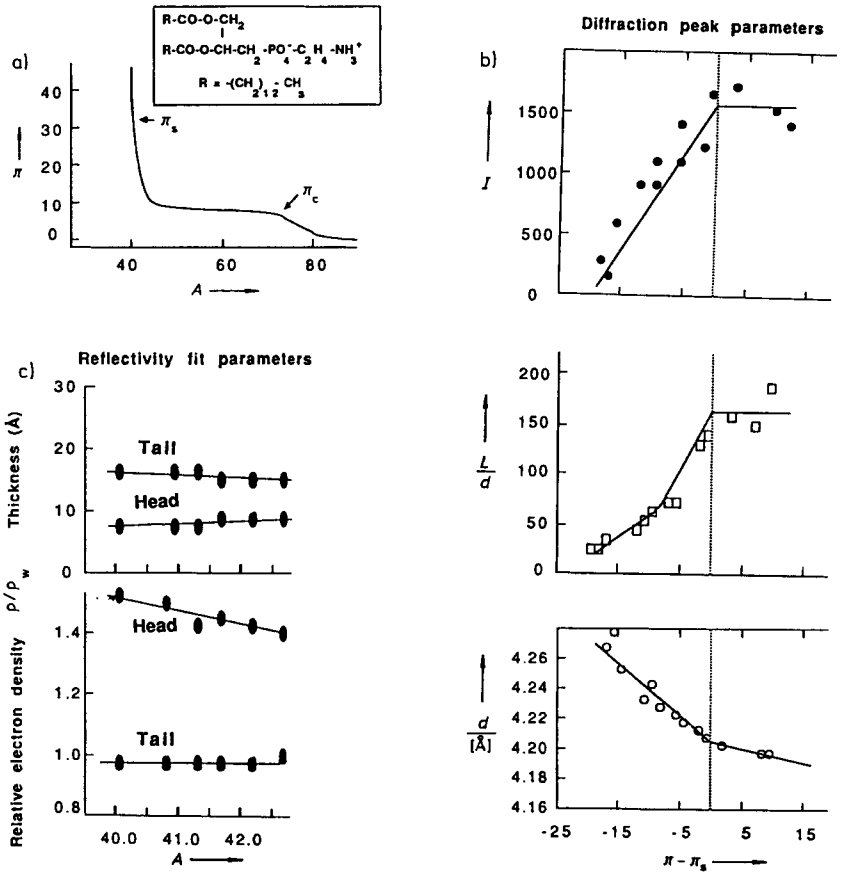

Fig. 18. Phospholipid DMPE monolayer over pure water at room temperature: (a) Pressure-area isotherm and chemical formula of DMPE. (b) Three parameters extracted from the GID data as a function of surface pressure; the GID peak integrated intensity, the coherence length L and the d-spacing. (c) Model parameters thickness and electron densities $\rho(z)$ relative to that of water ρ_w used in XR data fitting, for the head and tail slabs.

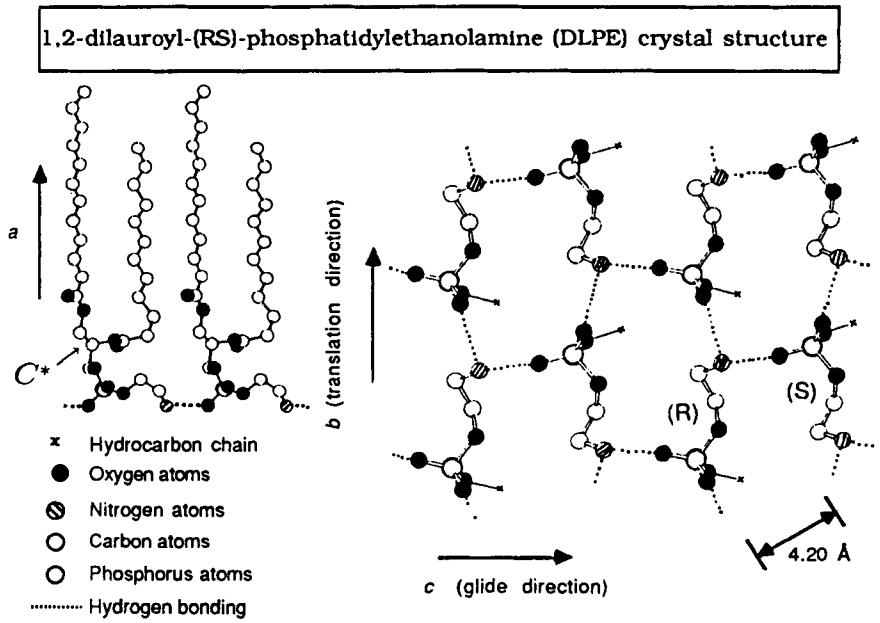

Fig. 19. The layer structure of 1,2-dilauroyl-(RS)-phosphatidylethanolamine (DLPE). The hydrogen atoms are omitted. Left: View down the c axis. Right: View down the a axis. The hydrocarbon chains are not shown for clarity. The molecules are interlinked by N-H···O hydrogen bonds (dashed lines) by translation symmetry along the b axis (molecules of the same configuration) and by glide symmetry along the c axis (molecules of the opposite configuration). Note the characteristic 4.20 Å spacing imposed by the molecular packing.

increasing with pressure. In the condensed phase, above π_s, the coherence length is no more than about 50 lattice distances, so if the monolayer is crystalline it must have many defects. Another possibility is that the structure is non-crystalline but hexatic.

Further X-ray studies with an extended q_z-acceptance range and Bragg Rod analysis [39,40] have shown that in the ordered phase the organization of the hydrocarbon chains changes with increasing pressure from an oblique structure with tilted chains (yielding three peaks, only one of which was detected in the earlier studies because for the other two Bragg Rods the intensity peaks well above the horizon) to a pseudo-hexagonal structure with the chains vertical. Quite similar structures have been observed [41] at room temperature in DPPE-monolayers where $\pi_c \sim 0$.

Although the early diffraction data [38–41] gave no direct evidence on the mode and degree of ordering of the phospholipid head groups PO_4^--CH_2-CH_2-NH_3^+ in the condensed phase, such order may be indicated by X-ray reflectivity data (Fig. 18c) and other arguments [41]. The question of the degree and mode of head group order in DPPE monolayers is currently under investigation by means of high-intensity Bragg Rod data [44].

Further information thereon and on the packing arrangement of the hydrophobic chains may also be gleaned from the three-dimensional crystal structure of the racemic (R,S) dilauryl derivative (DLPE) whose packing arrangement [45] is shown in Fig. 19. It is noteworthy that the most intense reflection from the layer structure of (R,S) DLPE has a spacing of 4.2 Å which is the same value as that of the single GID peak observed from the chiral resolved compressed monolayer of DMPE (Fig. 18b), indicating a similarity in packing of their hydrophobic chains. In the 3D crystal the molecules form a bilayer (only the monolayer is shown in Fig. 19); within each layer the head groups are interlinked by N-H···O hydrogen bonds by translation and glide symmetry. This head group packing is also observed

in the crystal structure of phosphorylethanolamine [46] HO-PO_3^--CH_2-CH_2-NH_3^+. It is tempting to think that the head groups of chiral resolved monolayers of DMPE, DLPE and DPPE would pack in the same way. That would imply two different conformations of the chains of the molecules of identical chirality that could be realized by a pseudo glide.

It should be noted that the thickness of the layer of the head groups in the 3D crystal structure is 5.5 Å, but is in the range of 7.15 to 9.5 Å in the monolayer structures according to the XR data.

For phospholipids with the more bulky choline (PO_4^--CH_2-CH_2-$N(CH_3)_3^+$) head group, e.g., DPPC, quite different structures were deduced from both X-ray [37] and neutron [42,43] reflectivity data: Even at the highest pressures the chains are tilted by *ca.* 30°, thus remaining in close-packed contact at the larger area per molecule dictated by the head group. GID data [47,44] indicates that the structures of chiral resolved and of racemic monolayers are quite similar.

3.1.3. α-amino acids

The α-amino acid surfactants were used for the oriented crystallization of the α-polymorph of glycine and of NaCl at the monolayer-solution interface [3], to be discussed in Section 5. GID and XR measurements were performed on two of these monolayers in order to establish independently the similarity or complementarity of the head group arrangement of the monolayer molecule and the layer arrangement of the crystal face attached to the monolayer [48–50]. Here we describe the packing characteristics of two α-amino acid surfactants, PL and PFA.

Palmitoyl-Lysine (PL): The N-H···O hydrogen bonding arrangement of the α-amino acid head groups NH_3^+-CH-$CO_2,^-$ and that of the amide groups CO-NH in the chain, essentially fixed the monolayer packing. The π-A isotherm of the monolayer of PL at room temperature is shown in Fig. 20a. A compressed (~25 mN/m) monolayer of PL was found by GID to form crystalline domains with a coherence length of about 500 Å. No diffraction signal could be detected for low surface pressures. The diffraction pattern [48] shows two Bragg peaks (Fig. 20c). The calculated GID positions and intensities for the model structure [48,51] are also shown in the same figure. Analysis of the observed XR data (Fig. 20b) yields a tilt angle of the molecular chain axis of about 30° from the vertical. The deduced cell axes and packing arrangement of PL is shown in Fig. 21. The α-amino acid head groups NH_3^+-CH-CO_2^- are arranged in a manner similar to that of crystalline α-glycine or other naturally occurring hydrophobic α-amino acids [52–54]. The linear N-H···O hydrogen bonds between amide groups in the chain linking neighboring molecules along the **a**+**b** director (Fig. 21b) requires a 30° tilt of the chain axes as was independently deduced from the XR analysis.

Perfluorododecyl-Aspartate (PFA): The behavior of PFA upon compression is similar to that of arachidic acid in that a continuous reduction of the molecular tilt angle happens with increasing surface pressure [50](a). However, the system revealed some original features. At low surface coverage (points α, β, γ on the isotherm in Fig. 22a), molecules of PFA self-assemble in large crystalline domains, arranged in an oblique cell, and tilted by about 22° from the surface normal towards nearest neighbors (Fig. 23), as deduced from the three observed reflections in Fig. 22d. Upon compression, the three peaks first merge into a doublet (Fig. 22c) and then into a singlet (Fig. 22b) indicating that the unit cell goes from oblique to distorted-hexagonal to pure hexagonal (cf. Fig. 13 and the related discussion). However, the symmetry of the molecular packing arrangement is not hexagonal but has only translational symmetry p1.

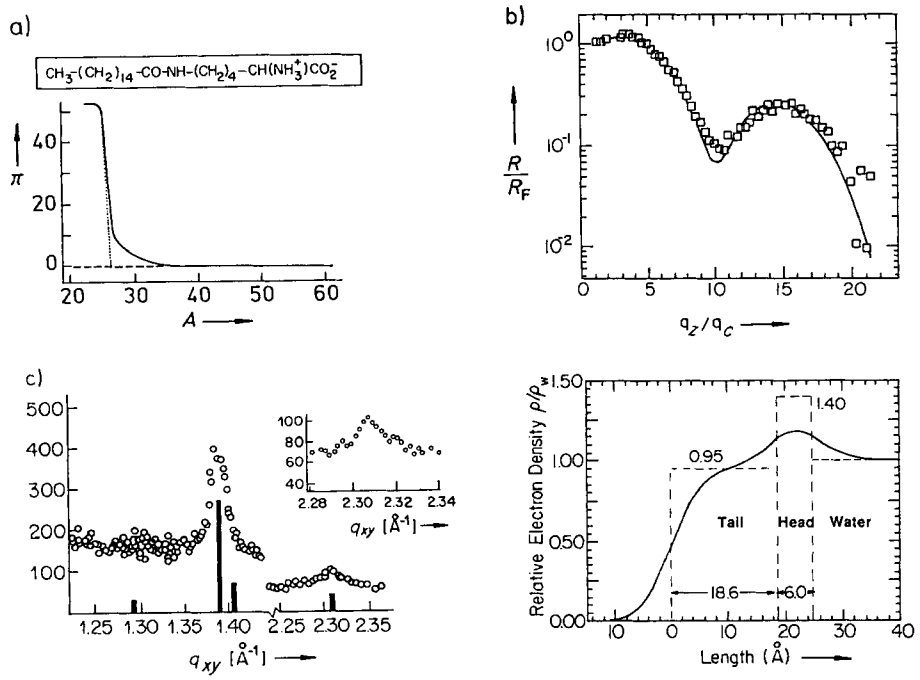

Fig. 20. Palmitoyl-(R)-lysine monolayers over pure water at room temperature. (a) Pressure-area isotherm and chemical formula of PL. (b) Top: The measured, normalized R/R_F reflectivity curves and the theoretical model fitted thereto. Bottom: The refined model electron density $\rho(z)$ relative to that of water ρ_w. The PL molecules are modeled by two slabs, one corresponding to the head group and the other to the hydrocarbon tail. The smeared model shown as a full line is obtained with a smearing of 3 Å. (c) GID of a compressed PL monolayer. The calculated relative intensities of the model (Fig. 21) drawn in underneath the peaks are without adjustable parameters but for scale and Debye-Waller factors.

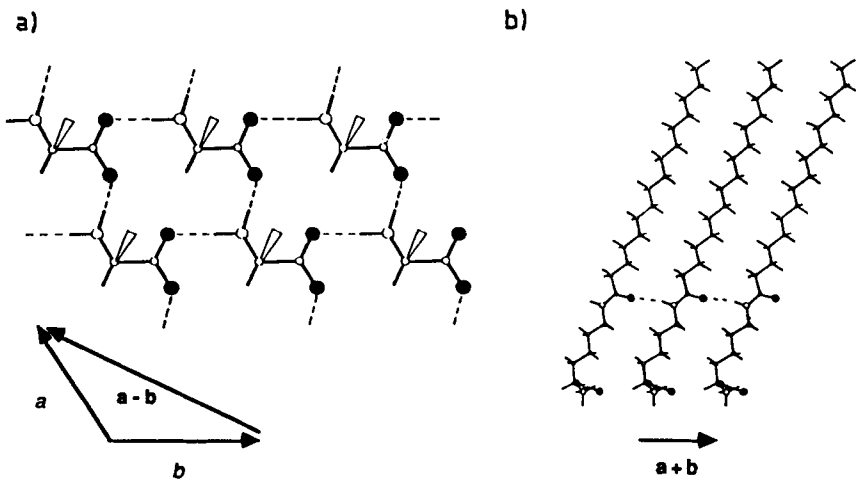

Fig. 21. Views of the model packing arrangement of palmitoyl-(R)-lysine monolayers. (a) Perpendicular to the monolayer plane, the hydrophobic chain is represented by a wedge. (b) View along the **a** − **b** axis showing molecules in a row parallel to the **a** + **b** direction, interlinked by N-H···O=C (amide) hydrogen bonds.

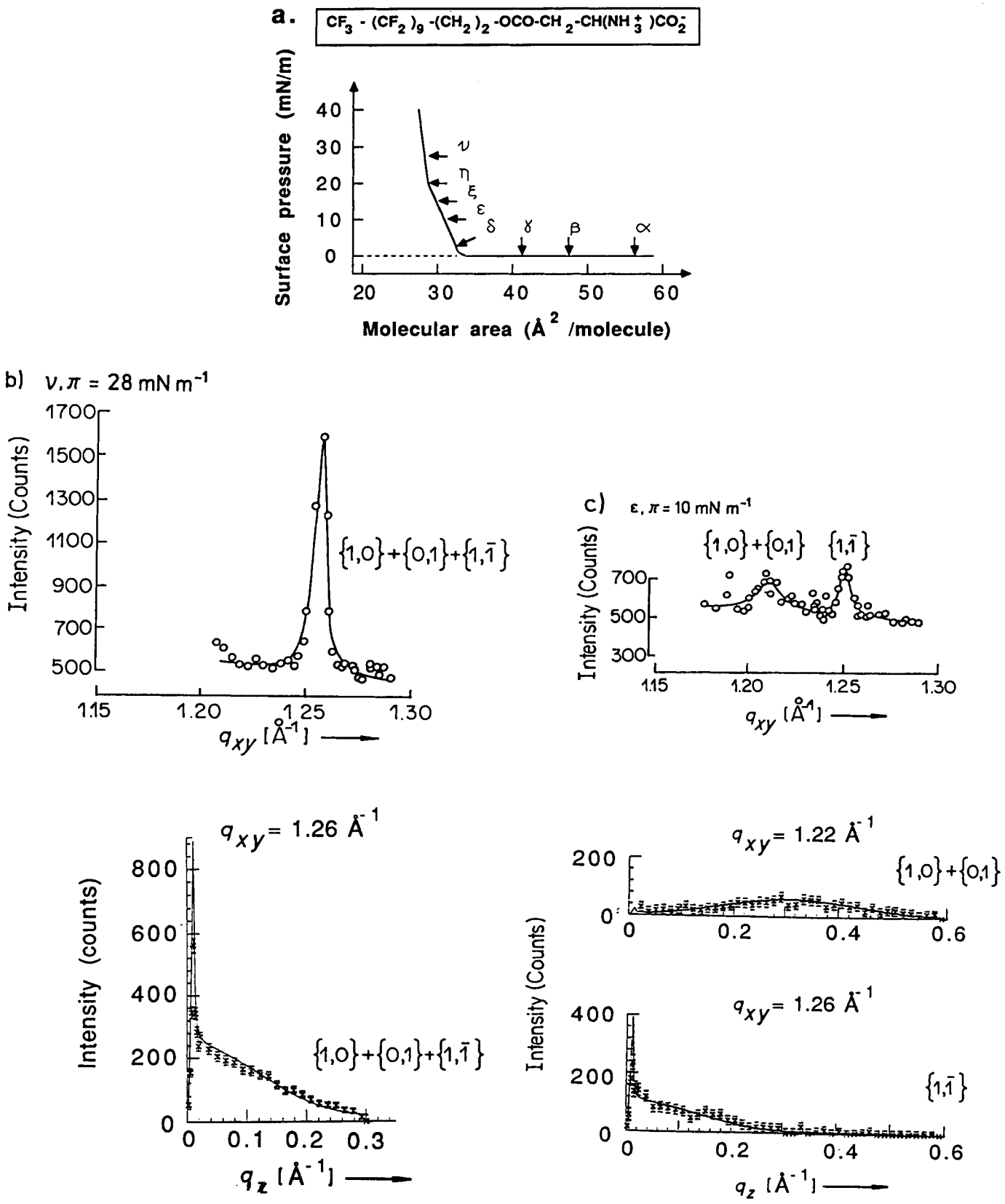
a.
CF3 - (CF2)9 -(CH2)2 -OCO-CH2-CH(NH3+)CO2-
Surface pressure (mN/m)
Molecular area (Å2 /molecule)
ν
η
ξ
ε
δ
γ
β
α
b) ν, π = 28 mN m-1
Intensity (Counts)
{1,0}+{0,1}+{1,1̄}
qxy [Å-1]
c) ε, π = 10 mN m-1
{1,0}+{0,1}
{1,1̄}
qxy = 1.26 Å-1
Intensity (counts)
qz [Å-1]
qxy = 1.22 Å-1
Intensity (Counts)

Fig. 22. (a), (b), (c).

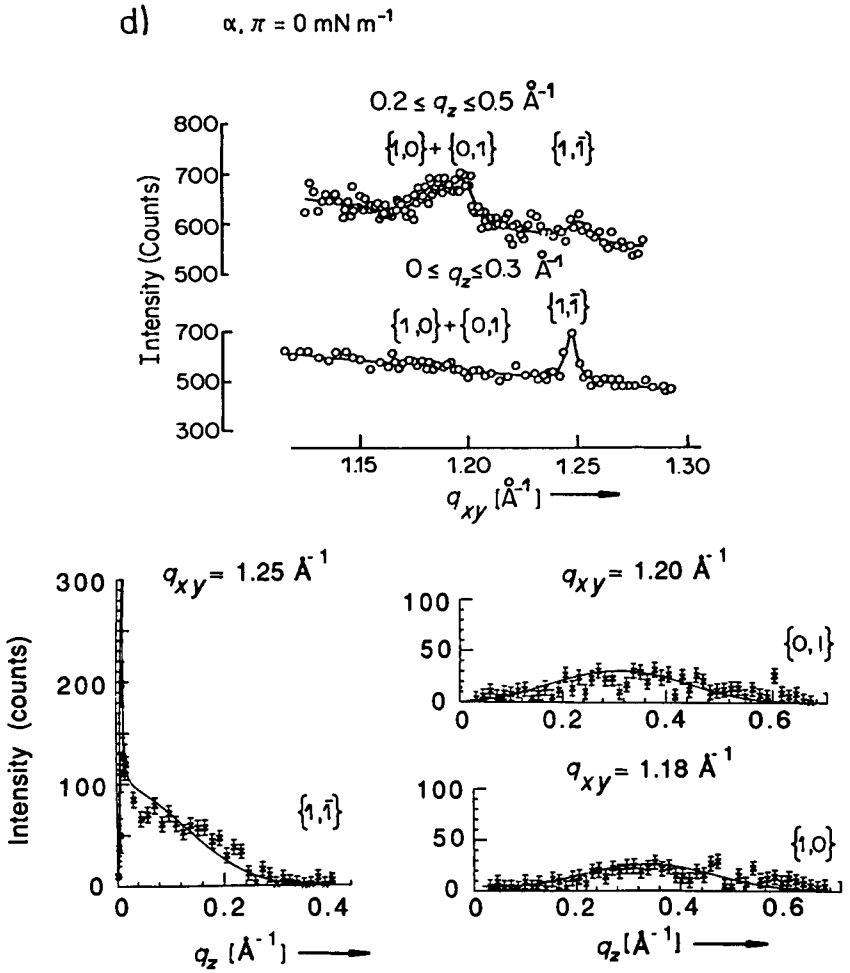

Fig. 22. PFA monolayers over pure water at room temperature. (a) Pressure-area isotherm and chemical formula of PFA. The points $(\alpha-\nu)$ indicate where GID measurements were made. (b), (c), (d) A selection of GID measurements showing three different 2D crystal symmetries (cf. Fig. 13) when increasing the surface pressure. Top: GID peaks. The reflection indices are indicated. Bottom: Bragg rod profiles measured on the GID peaks. Reflection positions and indices are given. Note that in (d) the GID peaks were measured for two different q_z intervals; also the Bragg rod intensity profiles have a different scale than in (b) and (c). In all cases, the solid line is the model fitted to the data.

The molecular behavior of monolayers of PFA during a compression-decompression cycle can be explained with a knowledge of the head-group packing before compression [50](a). The hydrogen-bonding motif of the α-amino acid head-groups of uncompressed PFA was constructed from the known motifs of the 3D crystal structures of neopentyl-glycine [5](b), (S)-alanine [55] and (R,S)-alanine [56]. The major feature of this motif is the participation of intercalated ordered water molecules interlinking neighboring hydrogen-bonded ribbons of PFA molecules (Fig. 23). The molecular area, which is dictated by the head group, is 30.9 Å^2 as compared with the cross-sectional area of the fluorocarbon chain which is 28.5 Å^2. Upon increasing the pressure, the molecular area is reduced and the water molecules are probably partially squeezed out of the hydrogen-bonded layer. At high pressure, the hexagonal cell dimensions are imposed by the close contact between the fluorocarbon chains. Release of the surface pressure causes a dramatic decrease in coherence length L, tilting of

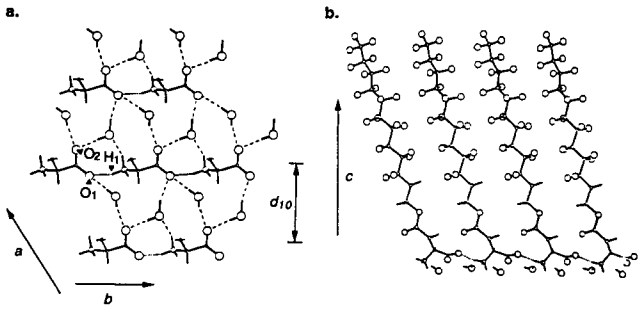

Fig. 23. Model arrangement of the self-assembled crystallites of PFA monolayer over water at zero pressure. Left: View perpendicular to the monolayer showing hydrogen bonding of head groups and water molecules. O_1 and O_2 are the oxygen atoms of the carboxylate groups, each forms hydrogen bonds with the hydrogens of two water molecules. O_1 form a hydrogen bond with the hydrogen atom H_1 of the NH_3^+ moiety. The molecular chains are omitted for clarity. The oxygen atoms of the water molecules are indicated as filled circles. Right: View along the a axis showing the attached layer of water molecules, and the projection of the chain tilt in the $(1,\bar{1})$ plane.

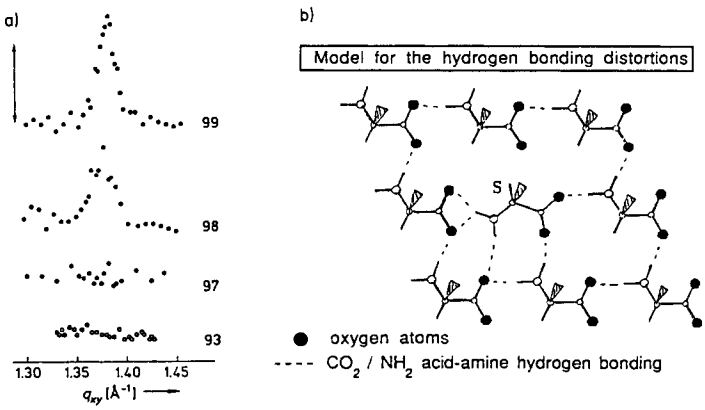

Fig. 24. (a) GID data of chiral mixed monolayers of palmitoyl lysine (PL). The percentage of the (S)-enantiomer in the mixture is indicated. (b) A PL molecule of (S) configuration surrounded by PL molecules of the opposite (R) configuration in a possible packing arrangement. All the chains are restricted to be related by translation, and are indicated by wedges, so that the distortion of the hydrogen-bonding between neighboring head groups is visible.

the molecules and finally disappearance of any observable diffraction probably linked to the dynamics of the building process of a new bonding layer akin to the original one.

3.1.4. Enantiomeric mixtures of α-amino acid monolayers

When as little as 3 per cent of the opposite enantiomer is included in the chiral resolved monolayer of PL, the GID peak disappears (Fig. 24a). This indicates that the lattice of the monolayer becomes sufficiently distorted to drastically reduce the crystalline coherence length. This effect was explained by the possible inclusion of say an (S)-molecule in a lattice of (R)-molecules, as shown in Fig. 24b. The figure shows that in order to reduce bad intermolecular contacts, the structure becomes distorted. Thus an appreciable fraction of the molecules in the monolayer are misaligned when even as little as 3 per cent of the opposite enantiomer is added. It is noteworthy that the pure racemate did not give a diffraction pattern at room temperature. Here we might have expected an arrangement in which the (R) and (S) molecules are interlinked in a layer by glide symmetry as observed in the crystal

structure of hydrophobic (R,S) α-amino acids [5,56]. We cannot rule out that the pure racemate contains small ordered domains of such a type in solid solution.

In contrast to PL, the molecular area of compressed PFA monolayers (28.5 Å^2) as imposed by the perfluorinated chain, is larger than that of compressed monolayers of PL (24.3 Å^2) and that of glycine in its crystal structure (25.5 Å^2). Therefore, the more open head group arrangement of PFA is in keeping with the observation that racemic mixtures of compressed PFA display a very intense diffraction peak [51](b). Unlike for PL, addition of the opposite enantiomer does not affect the crystal packing: The distortion introduced in the hydrogen-bonding at the head group can be accommodated without disturbing the long-range crystalline order in compressed PFA monolayers.

3.2. *Phase changes induced by temperature*

There is a wealth of macroscopic data available on temperature-induced phase transitions in Langmuir films, yet little reliable structural information on the molecular level could be deduced. Only recently is such information becoming available from GID data. For example, the results on monolayers of fatty acids and alcohols indicate a reduction in rotational disorder upon reduction in temperature. Indeed, the diffraction pattern at high surface pressures (30 mN/m) for Langmuir films of the alcohol $C_{21}OH$, and the carboxylic acid $C_{20}CO_2H$ upon cooling from 30°C to 0°C shows that the single peak observed at high temperature (Fig. 25a) is split into two peaks a lower temperature (Fig. 25a,b), indicative of a change from hexagonal to a centred rectangular cell [28,29]. The change was interpreted as being caused by a pronounced reduction of librational motion of the molecule about its chain axis. Diffraction data on compressed monolayers of acids $C_{21}CO_2H$ [33] and $C_{29}CO_2H$ [58], and on alcohols $C_{23}OH$, $C_{30}OH$, $C_{31}OH$ [58] and $C_{21}OH$ [29] showed that in the compressed state, at all temperatures, the molecules are vertically aligned.

For the alcohol monolayers, on reduction of pressure, only structures with a uniform tilt of the molecules approximately towards their next nearest neighbors were observed [58–61,29], cf. Section 3.3.3 below.

By contrast, the homologous series of long chain fatty acids C_nCO_2H show a richer behavior. Their phase diagrams have been studied by means of pressure-area isotherms [62]. The phase diagrams of the series seem to be approximately identical, provided that the temperature scale is shifted by 5-10°C for each additional CH_2 moiety : extending the chain length is as good as lowering the temperature. The available GID data [17,30–33,63,64] taken as a whole, seem to confirm this conjecture. The phase diagram of docosanoic acid (n = 21) is shown in Fig. 26. The acid $C_{21}CO_2H$ is convenient because nearly all the phases are observable at temperatures 5-30°C. Two independent synchrotron GID studies determined the structure of all the phases of docosanoic (n = 21) acid [33] and heneicosanoic (n = 20) acid [32]. The diffraction results were similar and we report here those observed with docosanoic acid monolayers. In each phase, the molecules are oriented with their long axes parallel and form a 2D crystal structure, albeit with positional coherence lengths ranging from 50 Å at high temperatures to more than 1000 Å at lower temperatures. The higher-temperature structures may be similar to the mesophases found in liquid crystals. The L_2 phase (Fig. 26) has tilted molecules on a centered-rectangular net, the tilt being towards nearest-neighbors. On compression, at temperatures above *ca.* 25°C one enters through a second-order phase transition into the hexagonal LS phase with vertical molecules. At these temperatures, indirect evidence suggests that the molecules are free rotators. At lower temperatures, compression leads from the L_2 phase through a first order

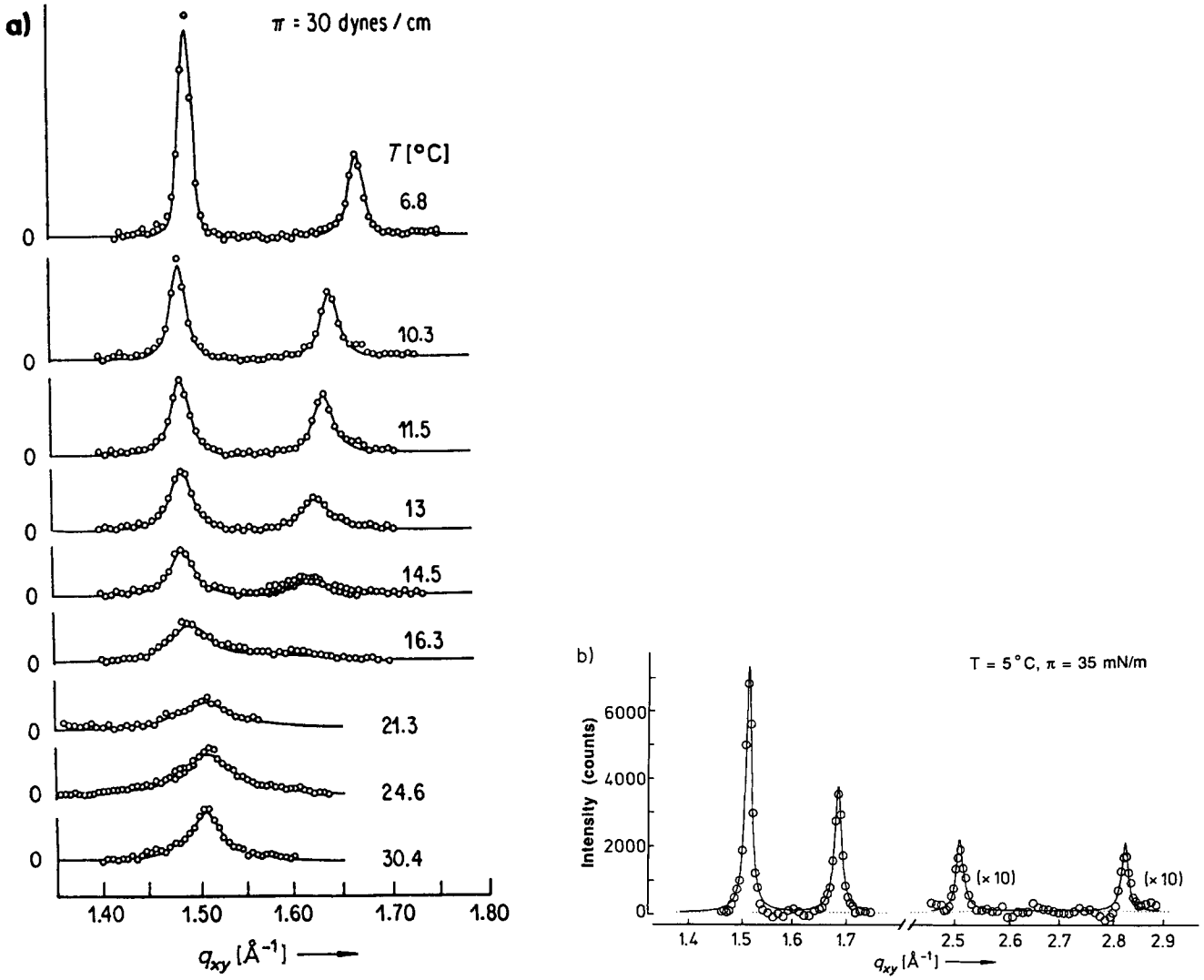

Fig. 25. (a) Monolayer of the alcohol $C_{21}OH$ over pure water (from Ref. [28]): GID data taken along the isobar at 30 mN/m. There is increasing peak intensity with decreasing temperature. The peak splitting is due to the transition from a hexagonal to a distorted hexagonal net. A linear background has been subtracted. (b) Monolayer of $C_{20}CO_2H$ (from Ref. [57]): GID at 5°C and π = 35 mN/m. A linear background has been subtracted. In addition to the split reflection observed as for the alcohol monolayer for 6.8°C in (a), two higher order reflections are shown here. For these reflections the signal is multiplied by a factor 10 in the figure.

phase transition to the L_2' phase (Fig. 26), again with tilted molecules on a centered-rectangular net, but with the molecules inclined towards next-nearest neighbors. Further compression leads to the phase S with vertical molecules on a centered-rectangular net (Fig. 26). One may speculate that in going at high pressure from the hexagonal phase to the distorted-hexagonal S phase, the mechanism for breaking the hexagonal symmetry is that the molecules become hindered rotators. Below *ca.* 10°C at high pressure, one observes the CS phase (Fig. 26) which has the same symmetry as the S phase. The CS phase, however, has long positional coherence lengths (> 1000 Å), a small area per molecule (18.6 Å^2), and a very low compressibility. One may compare it to 3D-crystalline

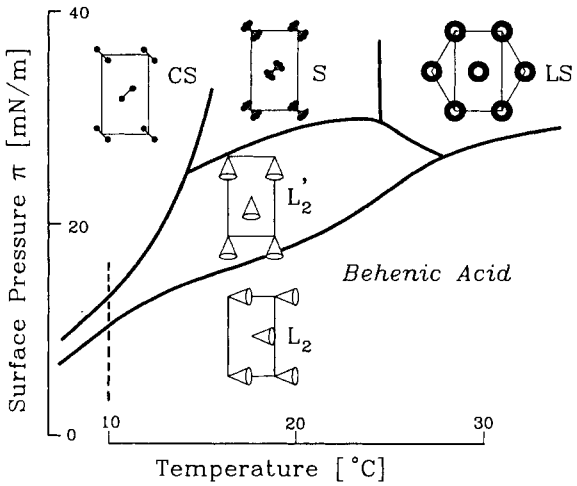

Fig. 26. Phase diagram for monolayers over pure water of docosanoic or behenic acid ($C_{21}CO_2H$) (from Ref. [33]). See the text for an explanation of the structures.

structures of alkanes, well below their melting points in which the molecular back-bones are locked in a herring-bone pattern [65].

Monolayers of tetracosanoic acid ($C_{23}CO_2H$) have been studied with great thoroughness at $pH = 2$ along the isotherm indicated by the dashed line in Fig. 26[2] by Schwartz et al. [63,64]. These authors find that the pressure-induced isothermal phase transition requires long equilibrium times. In stead of the sequence $L_2 \rightarrow L_2' \rightarrow$ CS they report the *reentrant* sequence $L_2 \rightarrow$ CS $\rightarrow L_2 \rightarrow$ CS $\rightarrow$ with L_2' coexisting with CS at the phase boundaries.

Based on GID data for $C_{20}CO_2H$, Shih et al. [120] report the existence, between the S and LS phases, of yet another phase 'Rot1' with the same symmetry as the S phase, and, correspondingly, at lower pressures between the L_2' and L_2 a phase 'C'' with the same symmetry as the L_2' phase (not shown in Fig. 26).

3.3. *Crystalline self-assembly of amphiphilic molecules*

3.3.1. *Experimental observations*

The degree of crystalline order in biological lipid membranes in solution is probably low. But we may expect a high degree of order in self-aggregated clusters of amphiphilic molecules at the water surface because of the constraints imposed; a "flat" surface and solvent in contact only from the hydrophilic side. Direct evidence for self-organized 2D crystalline clusters is now available from GID, but only for the water-insoluble species. For soluble species, characterization by X-ray diffraction has not been achieved as yet, possibly because of the low scattering power of these molecules and furthermore the range of crystallinity of the clusters may be very small. Nevertheless, evidence for aggregation comes from specular neutron reflectivity data [66]; evidence in favor of some degree of ordering comes from oriented epitaxial crystallization in the subphase at the solution surface [5]. More recently, a remarkable observation was made by fluorescence microscopy [67]: two-dimensional faceted crystals of sodium dodecyl sulfate with facets as large as 50 μm could be seen on the water

[2] With a corresponding change from *ca.* 10°C (as in Fig. 26) to *ca.* 20°C.

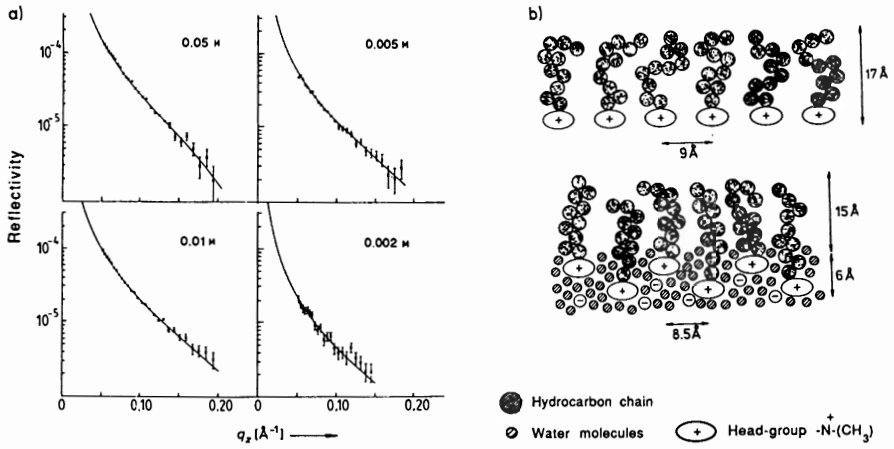

Fig. 27. (a) Observed neutron specular reflectivity profiles of fully deuterated decyltrimethylammonium bromide in contrast matched water, for different molecular orientations and the theoretical model fitted thereto (from Ref. [66](a)). (b) Model for the distribution of water and decyltrimethylammonium molecules at the air/solution interface. Top: Configuration of the molecules within the adsorbed layer at 0.01 M or less. Bottom: The surface layer at 0.05 M deduced from isotopic substitution neutron measurements (from Ref. [66](a)).

surface, for a concentration of 0.055 per cent by weight which is far below the critical micelle concentration (0.25 per cent by weight).

Neutron reflectivity measurements (Fig. 27a) performed on a soluble surfactant, decyltrimethyl ammonium bromide (DTAB) at the air-solution interface [66] provide some information on the self-organization of the system. They indicate a vertical alignment of these molecules, yielding a layer thickness of about 16 Å for concentrations varying from 0.002 to 0.01 M. Since the extended chain plus head group is about 17 Å thick, the molecules are assumed to lie in one layer as shown in Fig. 27b. At a concentration of 0.05 M, where the monolayer is essentially complete, the reflectivity measurements yielded a film thickness of about 21 Å (Fig. 27b). This was explained in terms of a staggered configuration reducing the electrostatic repulsion.

X-ray reflectivity measurements of norleucine solutions and surface tension measurements of several hydrophobic α-amino acids, such as leucine, valine, isovaline, phenylalanine and α-amino octanoic acid suggested accumulation of the molecules at the air-water interface [5]. Evidence for organized 2D clusters of these molecules at the air-water interface was obtained by crystallization experiments [5]: these additives promote formation of α-glycine crystals at the water surface from specific faces. It was shown that the appearance of these faces can be controlled by choosing the additive, thus establishing a direct correlation between organized aggregates of the hydrophobic α-amino acid at the surface and the face of α-glycine from which the crystal grows.

If these short chain hydrophobic α-amino acids spontaneously aggregate at the interface, Langmuir monolayers such as palmitoyl lysine (PL) and perfluoro-aspartate (PFA), which also induce α-glycine crystallization, should behave similarly. PL in the uncompressed state at room temperature did not yield any diffraction signal [48]. But it was found that uncompressed PL, with an average molecular area 10-15 times greater than its molecular area in the compressed state, induced oriented crystallization of α-glycine, suggesting ordered monolayer domains [3](b,c). Apparently these domains at room temperature are too low in coherence length to be detected by surface diffraction with the intensities available today. In contrast, as mentioned earlier, self-assembled crystalline domains of

PFA were detected by GID with only 50 per cent surface coverage. The fluorine atoms, which induce a helical conformation in long fluorocarbon chains [68], render these chains stiffer than aliphatic hydrocarbon chains and lower the possibility for conformational disorder. Hence, Langmuir monolayers of fluorinated molecules were characterized by a higher crystallinity than the hydrocarbon counterpart. GID data of fluorinated monolayers of PFA [50](a) and $C_{10}F_{21}$-CH_2-CO_2H [69] suggested the coexistence of crystalline and dilute disordered phases; in the latter the PFA molecules have a molecular area of about 100 Å^2 and $C_{10}F_{21}$-CH_2-CO_2H an area of 2000 Å^2, indicating a gaseous state. This result may be compared with results obtained for arachidic acid monolayers ($C_{19}CO_2H$) at room temperature and at low surface pressure [31] where in the tilted solid L_2 phase the molecular area is 24 Å^2; this phase coexisting with a fluid phase of molecular area 31 Å^2. The greater extent of crystallinity in fluorocarbon monolayers may be due not only to higher stiffness of the carbon backbone. Atom-atom potential energy calculations [70] have indicated a more favorable van der Waals interaction energy between fluorocarbon chains than between hydrocarbon ones.

Lowering the temperature considerably enhances the tendency for high crystalline order in the uncompressed state presumably by reducing molecular motion and so providing effective intermolecular interactions. Low temperature GID studies were performed on several monolayers C_n-X with different head groups X, *i.e.* $C_{16}OH$, $C_{20}OH$ [60,61]; $C_{23}OH$, $C_{30}OH$, $C_{31}OH$ [58,59,71]; $C_{19}CO_2C_9OH$, $C_{19}CO_2C_{10}OH$ [59,71] $C_{29}CO_2H$ [58,72]; $C_{19}CONH_2$ [58]; $C_{29}CONH_2$ [60]; and $C_{18}OC_6H_4$-CO_2H (where C_6H_4 is a *p*-phenyl ring introduced in the chain) [60].

3.3.2. *Structure determination of self-assembled crystallites by GID and lattice energy calculations*

The probable packing characteristics of these spontaneously formed crystallites could be extracted from the GID data [58]. But we stress that advantage was taken of known 3D crystal structures of molecules with long hydrocarbon chains as well as atom-atom potential energy calculations to reduce ambiguities. This strategy is meaningful since the 3D crystal structures are comprised of molecular layers which may be compared with the proposed monolayer structure. Atom-atom potential energy calculations have been used with a good measure of success [73–79] for extracting probable packing arrangements from an ensemble of (computer) generated 3D crystal structures and for 3D crystal structure refinement. It is of course necessary that the atomic potential energy parameters be known with sufficient accuracy, which is the case for the hydrocarbon chain and for the head groups such as CO_2, $CONH_2$ and OH [76,77,34,80]. We shall present a description of the deduced packing of the acid (X=CO_2H), the alcohol (X=OH) and the amide (X=$CONH_2$) monolayers, but in detail only for the acid in order to outline the steps involved.

The GID pattern for the monolayer of $C_{29}CO_2H$ in the uncompressed state at +5°C is shown in Fig. 28. The pattern comprises two low-order reflections, which indicates a rectangular cell for which the symmetry-related $\{1,1\}$ and $\{1,\bar{1}\}$ reflections coincide and the $\{0,2\}$ reflection is separate and distinct. The intensity profile of the Bragg rod for the $\{0,2\}$ reflection has its maximum at $q_z = 0$ Å^{-1}; hence the molecular axis lies in a plane perpendicular to the long *b* axis of the unit cell cf. Fig. 13. The angle of tilt of the hydrocarbon chain within this plane can be extracted from the intensity profile of the $\{1,1\}$ and $\{1,\bar{1}\}$ Bragg rod. The chain is tilted at 27° towards nearest neighbors along the short *a* axis. This angle is compatible with the value 5.53 Å of *a*, because, according to GID measurements, the acid hydrocarbon chain, in the compressed state, stands vertically with *a* reduced in length to 4.94 Å. These two lengths yield a molecular tilt angle of 26°(= arccos 4.94/5.53) in the

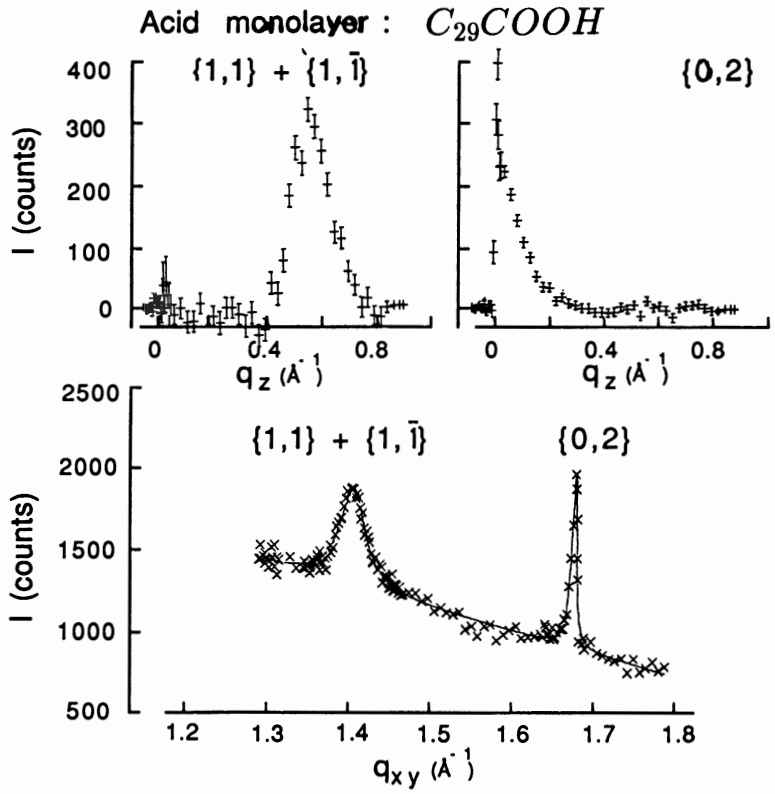

Fig. 28. Grazing incidence X-ray diffraction data for the $C_{29}CO_2H$ acid monolayer at zero surface pressure over pure water at 5°C. Top: q_z-resolved Bragg rod profiles. Bottom: q_z-integrated Bragg peaks. The $\{h, k\}$ reflection assignment is indicated on the two data sets.

uncompressed state, in close agreement with the value derived from the Bragg rod profile.

In order to establish the cell symmetry and molecular packing, we now divert to review layered 3D crystal structures of long chain acids and alcohols.

In each layer the molecules are related by a glide so that neighboring hydrocarbon chains have parallel long axes, but are in a mutually perpendicular orientation when viewed down the long axis; the motif is described as orthorhombic orthogonal [65]. Common to all these structures are the parameters of the orthorhombic sub-cell, which is a projection of the unit cell onto a plane perpendicular to the molecular axis [65]. The sub-cell may be regarded as rectangular O⊥, as shown in Fig. 29a with dimensions a_s = 4.98 Å, b_s = 7.42 Å, corresponding to a cross-sectional area of 18.5 Å^2 per molecule. Remarkably, the calculated 2D cell of the $C_{29}CO_2H$ monolayer, projected onto a plane perpendicular to the molecular axis perfectly matches the orthorhombic sub-cell of the 3D crystal structures. Thus it was deduced that the $C_{29}CO_2H$ acid monolayer molecules appear in the orthogonal O⊥ packing, *i.e.*, they are related by a glide along the a axis in a primitive rectangular cell in plane group $p11g$ as shown in Fig. 30a. The symbol p specifies a primitive unit cell, the symbol g a glide plane perpendicular to the b axis; so naturally the glide is parallel to the a axis. In this arrangement, the hydrogen atoms of adjacent hydrocarbon chains intermesh and thus close packing of the chains is ensured [65]. Further, the molecular chain axis is parallel to the glide plane

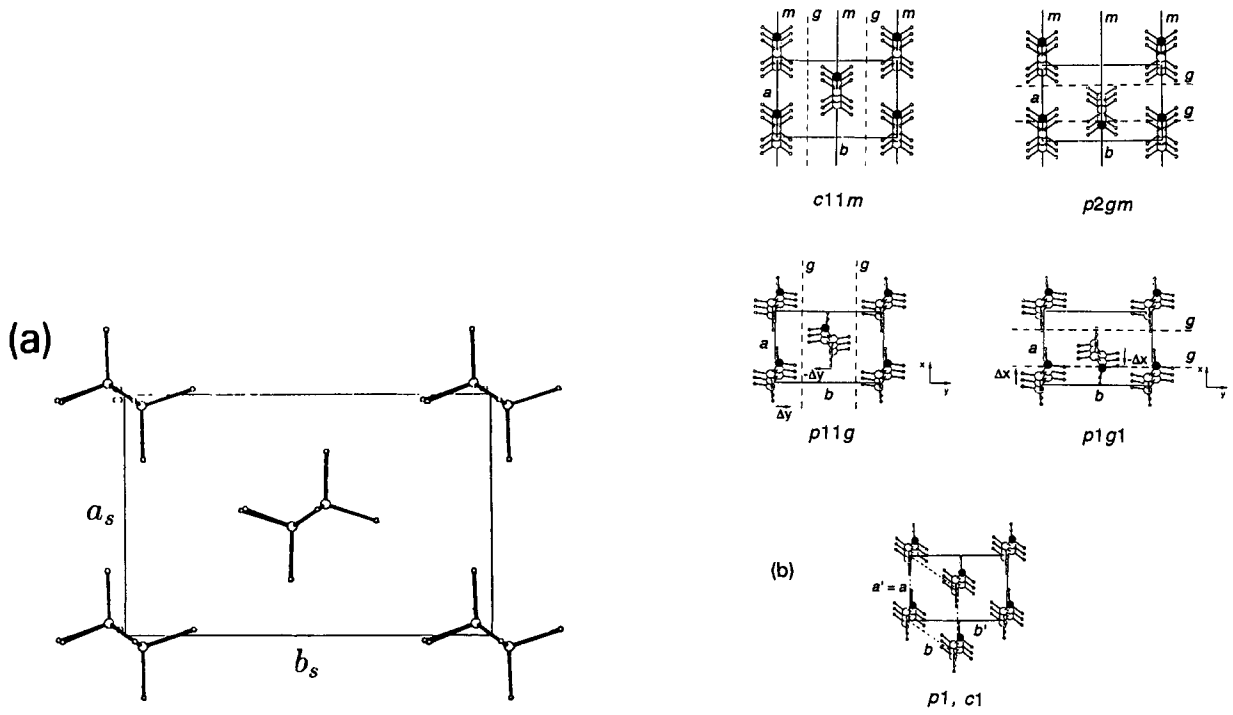

Fig. 29. (a) Schematic representation of hydrocarbon chains packing in the orthogonal O⊥ motif, as viewed along the molecular axis. The lengths of the axes are a_s=4.98Å and b_s=7.42Å. (b) View perpendicular to the water surface of some possible packing arrangements of model hydrocarbon chains in different plane groups (assuming that the chain is tilted along the a axis) (A) in plane group $c11m$, (B) $p2gm$, (C) $p11g$, (D) $p1g1$; and (E) in $p1$ with an oblique cell (a, b) (dashed lines), which can also be described as $c1$with a centered almost-rectangular unit cell (a', b') (solid lines). The glide or mirror symmetry elements are shown as dashed or full lines, respectively, in the conventional way [81]. For clarity, only six methylene CH_2 groups are shown for each chain. The terminal atom is shown filled in order to indicate the direction of molecular tilt and to differentiate more easily between the different packing arrangements. The molecular chains are shown as tilted from the vertical by $t = 10°$ along the short a axis. The unit cell axes (a, b) are indicated.

so that intermolecular contacts between methylene CH_2 groups of the glide-related molecules are the same along the chains.

3.3.3. *Detailed structure determination*

An independent *ab initio* demonstration of the orthogonal O⊥ packing of the hydrocarbon chains of $C_{29}CO_2H$ in plane group $p11g$ was provided by an analysis of the BR data [72] involving the calculation of a reliability index R_w, [3] complemented by lattice energy calculations. Molecular packing arrangements of $C_{29}CO_2H$ in various plane groups including $p1g1$, $p2gm$, $c11m$, as shown schematically in Fig. 29b, were eliminated on the basis of the BR data, and lattice energy calculations. For plane group $p11g$, the molecular arrangement of $C_{29}CO_2H$ was varied about its deduced position by rotation about three Eulerian angles (rotation angle ω about the vertical z axis, molecular tilt

[3] The weighted reliability index R_w is defined by $R_w = \sum_i w_0|I_0 - I_c| / \sum_i w_0 I_0$. The summation is over all the i individual Bragg rod points, where I_0 is the observed intensity of the i^{th} point, w_0, the weight, $= 1/\sigma(I_0)$, and I_c the intensity calculated from the structure factor formula, making use of the atomic xyz coordinates of the molecule. R_w is analogous to the reliability index used for 3D crystal structure determination.

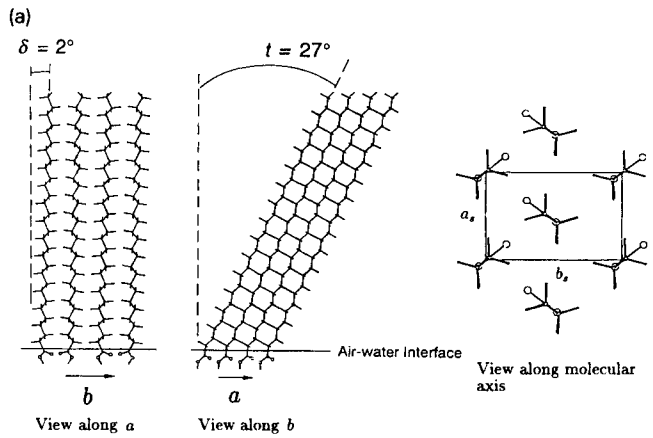

Fig. 30. (a) Molecular packing arrangement for $C_{29}CO_2H$ molecules in the 2D crystal. All molecules are tilted by $t = 27°$ from the vertical, in a plane deviating from the *ac* plane by an angle $\delta = 2°$, as shown: (left) view along the *a* axis, (center) the *b* axis, and (right) the molecular axis. Note that the molecules at the origin and at the center of the unit cell are related by a glide (at $y = \frac{1}{4}$) along the *a* axis. This packing arrangement, providing the absolute orientation of the molecule and the "lean" angle $\delta = 2°$ was deduced from a detailed analysis of the Bragg Rod data and from lattice energy computations, as described in the text. (b) $\{1, \pm 1\}$ and $\{0, 2\}$ Bragg rod intensity profiles *vs.* q_z of the uncompressed $C_{29}CO_2H$ acid monolayer over water. The lines are the best fits obtained for molecules packing in plane group $p11g$, tilted by $t = 26.5°$ along the *a* axis and $\delta = 0°$ (dashed line) and for the pseudo-glide packing model which has a "lean' angle $\delta = 2°$ (full line), as shown in (a).

angle t, and the rotation angle ϕ about the molecular axis). Also molecular translation along the y axis was applied. The model in which the molecular chain axes are centered parallel between the glide planes, tilted at an angle of 27° and oriented so as to form the orthogonal O⊥ packing, gave the lowest R_w index. The Bragg rod profiles calculated for the pure glide symmetry $p11g$, shown by the dashed lines in Fig. 30b, compared fairly well with the observed ones but the fit was not considered sufficient. The question then arose whether, for molecular layers on the water surface the assumption was justified, that molecules pack in plane group $p11g$ of perfect symmetry: Thus the glide symmetry was slightly relaxed by "leaning" the glide planes and also all the molecular chains (like a pack of playing cards) by a small angle δ about the glide axis, yielding a better fit to the BR data, as shown by the full lines in Fig. 30b. This relaxed symmetry may be a general phenomenon for it appears to occur in the monolayer crystallites of the uncompressed alcohols C_nOH, $n = 30, 31$ [59] in the Cd salt of $C_{29}CO_2$ [82] and definitely in the Cd salt of $C_{19}CO_2H$ [83]. In the latter, however, the reduced symmetry is brought about by the presence of the Cd ions. The R_w index is sensitive to parameters ω and y, and particularly to the tilt t, but less so to the molecular axial rotation parameter ϕ. For example it could not distinguish between two structures which differed only in axial rotation by 180°. This glaring ambiguity was eliminated, and the correctness of the model structure established, through lattice energy calculations, varying the same structural parameters as before. The energy curves certainly complemented the Bragg Rod analysis; they verified the model structure and removed the molecular rotational ambiguity since there is a calculated energy difference of 6Kcal/mol between the energy minima 180° apart.

Several packing characteristics of the carboxyl head group CO_2H could be deduced from the model arrangement (Fig. 30a). Firstly, neighboring CO_2H groups are too far separated to be interlinked by O-H$\cdots$O=C hydrogen bonds. Such a hydrogen bond would have required the antiplanar O=C-O-H_a

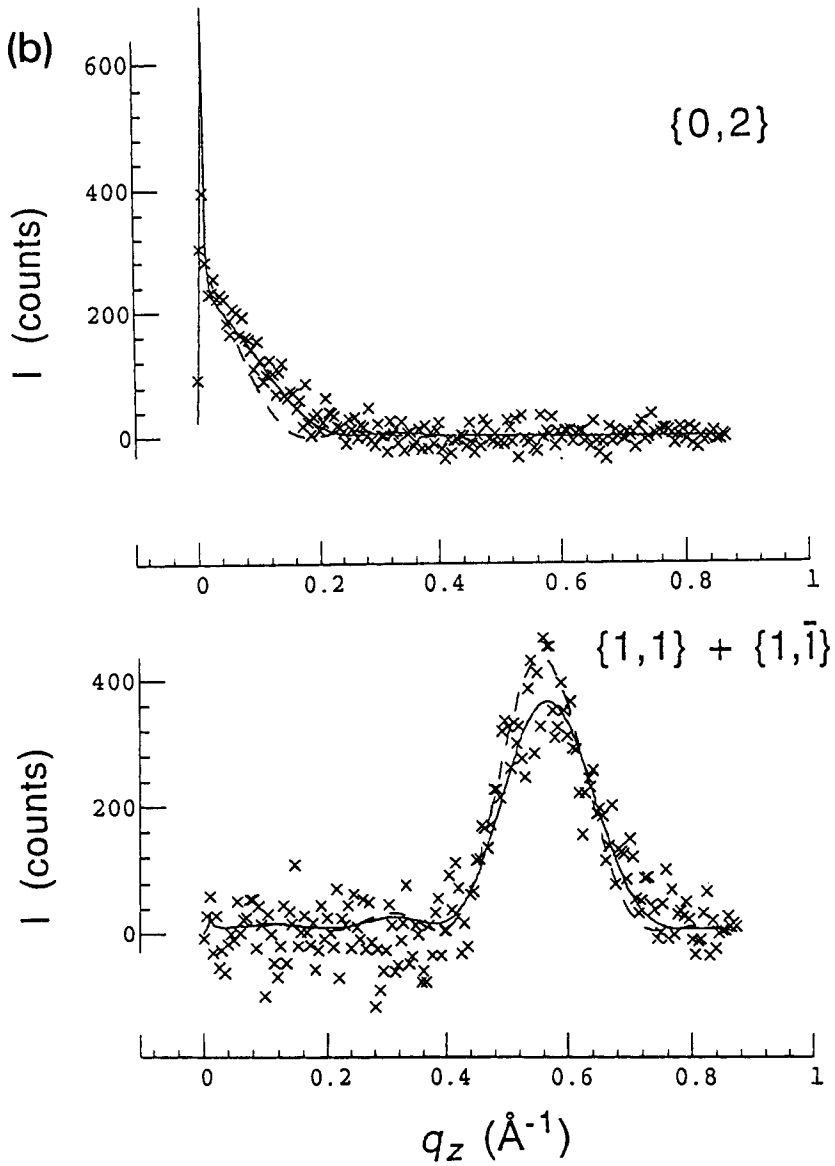

Fig. 30 — continued.

conformation so the carboxyl group probably adopts the more commonly observed and more stable synplanar O=C-O-H_s conformer (see Fig. 30a). The molecules, which are tilted at 27° to the vertical, are oriented so that the carbonyl oxygen atom and the hydroxyl OH groups are both equally well exposed to the water surface.

The Bragg rod data of uncompressed monolayers of alcohols $C_{23}OH$, $C_{30}OH$, and $C_{31}OH$ were analyzed [58,59] and interpreted in a manner similar to that adopted for the $C_{29}CO_2H$ monolayer, but for the fact that the GID data of the alcohols yielded an observed {2,0} reflection. The molecules crystallize in a rectangular cell in space group $p1g1$ (in this plane group the glide plane is perpendicular to the a axis) in the orthogonal O⊥ motif (Fig. 31). Unlike the $C_{29}CO_2H$ structure, the alcohol molecular chains are tilted by a low angle of $\sim 10°$ and in the direction of the long b axis. In these systems the presence of the {2,0} reflection enabled a reliable determination of the molecular mean

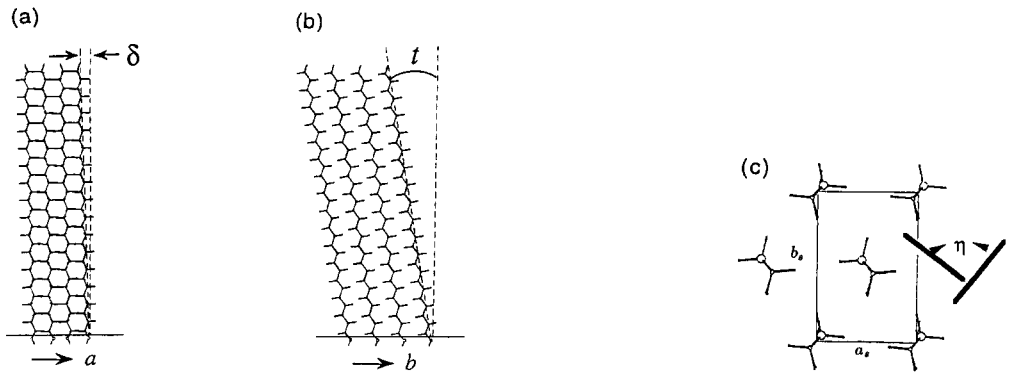

Fig. 31. Structure of the alcohol monolayers C_nOH (n = 23, 30, 31) in *pseudo* $p1g1$ symmetry. The "lean" angle of of the *pseudo* glide plane $\delta = 1.2°, 1.7°, 1.7°$; the tilt angles t in the direction of the b axis equal $9.2°, 7.8°, 9.7°$; and the dihedral angles η between the 'planes' of the *pseudo* glide-related molecules are $90°, 86°, 82°$ for (n = 23, 30, 31), respectively. (a) View along the b axis; (b) view along the a axis; (c) View along the molecular axis.

squared motion U_{xy} parallel to the water surface. A value U_{xy} = 0.08 Å^2 was obtained, in keeping with the molecular motion found at room temperature in layers of 3D crystal structures composed of amphiphilic molecules containing long hydrocarbon chains. The monolayers of the alcohols $C_{16}OH$ and $C_{20}OH$ [60,61] pack in an arrangement similar to $C_{23}OH$, $C_{30}OH$, and $C_{31}OH$, but with a larger tilt angle of $\sim$ 19°. The alcohols $C_{19}CO_2C_9OH$, $C_{19}CO_2C_{10}OH$ [59] pack in a manner very similar to the long chain acid $C_{29}CO_2H$.

The proposed packing arrangement of the 2D crystal structure of $C_{19}CONH_2$ [58], shown in Fig. 32, was based on the GID data and on three-dimensional crystal structures of long-chain diamides ($H_2NOC(CH_2)_{2n+1}CONH_2$). The intensity profiles of the Bragg rods indicate that the molecular chains are stacked in rows by translation along the 4.7Å a axis with the molecular axis tilted at an angle of 18° to the vertical. The molecules are interlinked by N-H···O hydrogen bonds by translation symmetry along the diagonal $(a + b)/2$ in accordance with the 3D crystal structures.

3.3.4. A Correlation between observed crystalline self-assembly and calculated lattice energies

The positional correlation lengths of all the crystallites $C_{21}CO_2H$ [33]; $C_{29}CO_2H$ [58]; $C_{16}OH$, $C_{20}OH$ [61]; $C_{19}CO_2C_9OH$, $C_{19}CO_2C_{10}OH$ [59]; in all of which the molecules are tilted by an angle $\geq$ 18°, were found to be anisotropic [58]; extending much further in the direction perpendicular to the molecular tilt direction than parallel to it. The lattice energy calculations were used also to help throw light on this coherence length anisotropy. The idea implemented involved calculation of the attachment energy of different (h, k) rows of molecules to the crystal; the logic being the lower the attachment energy the easier it is to disturb or disrupt the crystal about that (h, k) line. Such energy computations were performed on $C_{29}CO_2H$ [72], $C_{19}CO_2C_9OH$ and $C_{19}CO_2C_{10}OH$ [59]. A distinct correlation was obtained as the attachment energy was found to be much weaker for the molecular row corresponding to the broad {1,1} reflection than to the sharp {0,2} reflection (Table 2). Although this approach seems promising the data is still too sparse and a systematic study of a homologous molecular series is required to understand the relationship between the amphiphilic structure and the monolayer crystal morphology.

These results are in a sense a corollary of the observation that the stronger the interactions

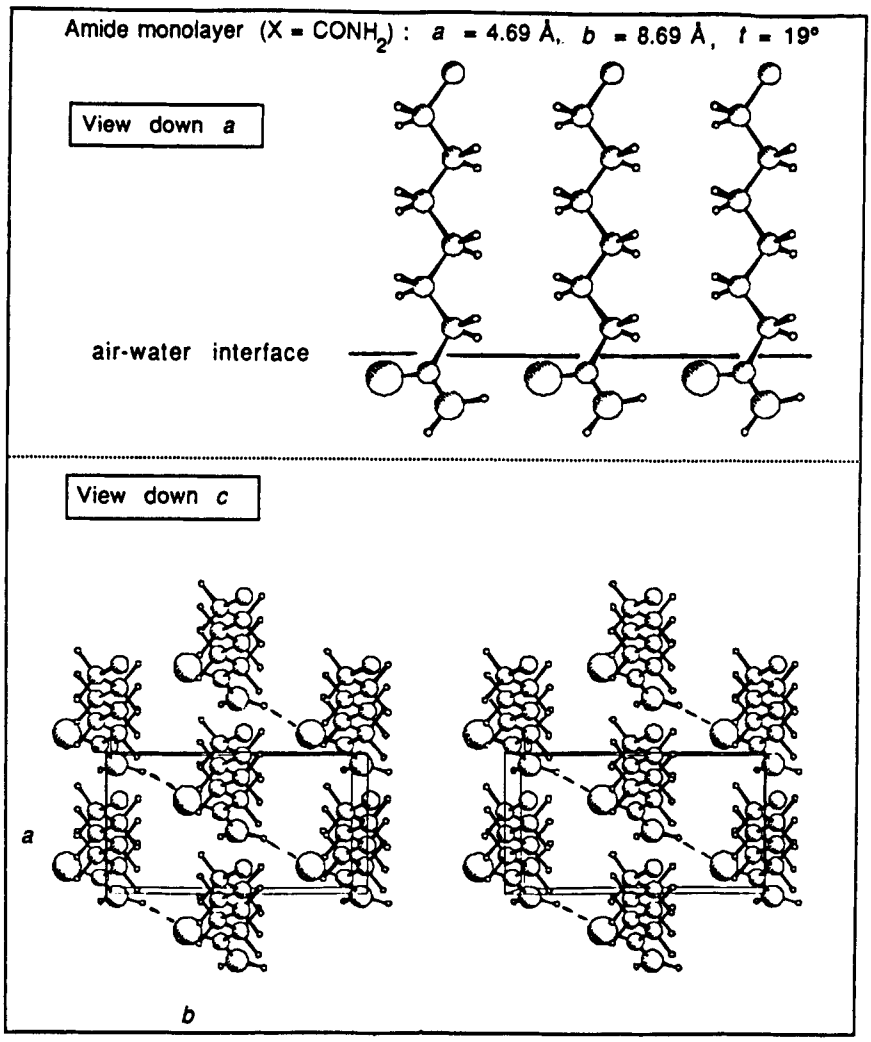

Fig. 32. Stereoscopic view of the packing arrangement of the arachidamide ($C_{19}CONH_2$) monolayer, seen perpendicular to the water surface, and a side view along a direction parallel to the water surface of models of the hydrocarbon chain packing in the crystallites formed at 5°C over pure water. For clarity only the head group and maximally eleven methylene groups CH_2 of each molecules are shown. The rectangular cell (a, b) is indicated.

between the amphiphilic molecules on the liquid surface, the more crystalline the material in the self-aggregated state [70,72,82,83]. This observation was shown to hold for the fatty acids C_nCO_2H (n = 14 to 29) over pure water; the longer the chain the more crystalline the material [70]. This increased crystallinity with chain length in the acids may be correlated with the contribution to the lattice energy of $\sim$ 2 kcal/mol per CH_2 group in the chain. This simple correlation is in keeping with the observation, alluded to earlier in Section 3.3.1, that fluorocarbon amphiphiles are more crystalline than their hydrocarbon counterparts because of more favorable inter-chain van der Waals interactions.

Table 2
Energy of attachment (E_{att}) per molecule to the $\{h, k\}$ facet of the monolayer crystals, and measured coherence lengths along these $\{h, k\}$ directions

	$\{h, k\}$	E_{att}(kcal/mol)	L(Å)
$C_{29}CO_2H$	$\{1, \pm 1\}$	-21.5	150(±10)
	{0,2}	-25.9	≥1000
$C_{19}CO_2C_9H_{18}OH$	$\{1, \pm 1\}$	-20.5	430(±10)
	{0,2}	-23.1	≥1000
$C_{19}CO_2C_{10}H_{18}OH$	$\{1, \pm 1\}$	-22.0	450(±10)
	{0,2}	-24.7	≥1000

4. Influence of ions and solutes on monolayer organization

4.1. Solute binding and growth and dissolution of monolayers

The binding of solute molecules to hydrophilic groups of monolayers allows us to probe not only its effect on the growth, stability and dissolution of 2D crystals, but to simulate interactions between the surface of a 3D crystal and solvent or solute molecules.

To date it has not been possible to monitor the process of nucleation and crystallization of layered 3D structures such as α-glycine or other amino acids from the air-water interface. But it is possible, with undersaturated solutions of these compounds, to show that the solute binds to the monolayer in a way similar to the way the nucleating crystal's first layer would be formed. Indeed, XR studies showed that even in undersaturated solutions of amino acids, the solute molecules bind to the interface. Reflectivity measurements were made on monolayers of PL over a dilute aqueous solution of glutamine NH_2-CO-C_2H_4-CH-(NH_3^+)CO_2^-, molecules [51]. Advantage was taken of the possibility that glutamine may bind to the monolayer via N-H···O bonds and may bind also to neighboring glutamine molecules by N-H···O (carboxylate) and N-H···O=C (amide) hydrogen bonds (Fig. 33b). The reflectivities of palmitoyl-R-lysine monolayers over the solution and over pure water are quite different (Fig. 33a). Analysis of the two data sets shows that as much as one quarter of the sites below the head groups is occupied by glutamine. The result is in qualitative agreement with the model shown in Fig. 33b.

Addition of solute species in the subphase can deter crystalline self-aggregation of monolayers so that growth of the latter can be monitored as a function of time. Fig. 34a shows that 10 minutes after a PFA monolayer was deposited over an undersaturated solution of glycine, no diffraction peak had developed, as opposed to pure water subphase [50]. It took around 30 minutes before crystalline domains could be detected. This inhibition can be understood from Fig. 34c, which shows how one glycine molecule can bind to two neighboring molecules of the α-amino acid monolayer with very strong hydrogen bonds, and so hinder their proper juxtaposition. The formation of this complex is in kinetic competition with that of the crystalline hydrogen-bonded bilayer which is composed of quasi-cyclic dimers of PFA and glycine (Fig. 34d). That this bilayer is eventually formed is deduced from the following observations : firstly, glycine forms oriented crystals attached to monolayers of PFA, denoting formation of a bilayer at the onset of crystallization [3]; secondly, monolayers of PFA

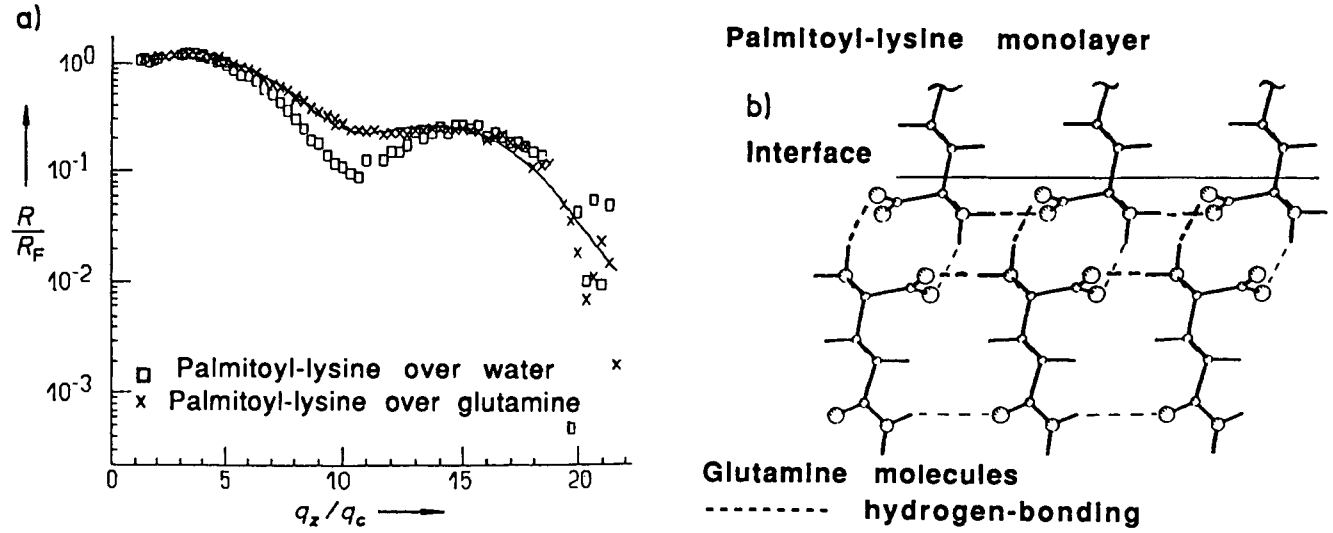

Fig. 33. (a) Reflectivity data of compressed monolayers of palmitoyl-(R)-lysine over water and over an undersaturated solution of (S)-glutamine (0.137 M). (b) A model of surface enrichment of glutamine at the interface. The hydrophobic chains are represented by a short segment thereof. Hydrogen bonding between amide groups of neighboring glutamine molecules, and between the glutamine layer and the monolayer, is shown.

over glycine solutions maintain their crystallinity after compression and decompression, unlike PFA over pure water [50](b) and finally (this evidence is indirect), X-ray reflectivity measurements of monolayers of PL over glycine solutions showed that the glycine molecules accumulate at the interface [51](c), suggesting formation of an incomplete bilayer, as in the experiment with glutamine.

Use of β-alanine NH_3^+-CH_2-CH_2-CO_2^- as a solute molecule instead of glycine had an entirely different effect on the 2D crystals of uncompressed PFA; it did not strongly inhibit growth, but caused a complete dissolution of the PFA crystals over two hours as shown by GID measurements (Fig. 34b). This dissolution can be rationalized in terms of a strong interaction of β-alanine with the amino-acid head groups of neighboring surfactant molecules leading to a disruption of the 2D crystal (Fig. 34e). It is noteworthy that because of a molecular mismatch, β-alanine can hardly form a hydrogen-bonded cyclic dimer with the amino acid head group of the monolayer and certainly not a commensurate hydrogen bonded counter-layer (Fig. 34f) as can glycine (Fig. 34d).

These results provided incentive for more experiments with various amphiphile-solute interacting pairs. GID and XR measurements involving fatty amide or acid molecules on aqueous solutions containing cosolvents such as formamide $HCONH_2$ or formic acid HCO_2H are underway to probe the effect of such cosolvents on the structure and crystallinity of the monolayers. For example, formamide as pure solvent supports crystalline monolayers of $C_{29}CONH_2$ and of $C_{29}CO_2H$, in which the molecules are aligned vertically on the liquid surface [84]. By comparison the $C_{29}CO_2H$ molecules on a water surface are tilted by $\sim 26°$ from the vertical [72]. Formamide solvent also may induce formation of trilayer of arachidamide $C_{19}CONH_2$ on the liquid surface, with the molecules vertically aligned [84]. On water subphase, $C_{19}CONH_2$ forms a monolayer with the chains tilted by $\sim 18°$ from the vertical [58]. Cosolvents such as formic acid HCO_2H may have a pronounced effect on the coherence length of the monolayer; for example a 1M concentration of HCO_2H in aqueous solution inhibits the 2D crystalline self-aggregation of a monolayer of arachidamide [85]. These experimental

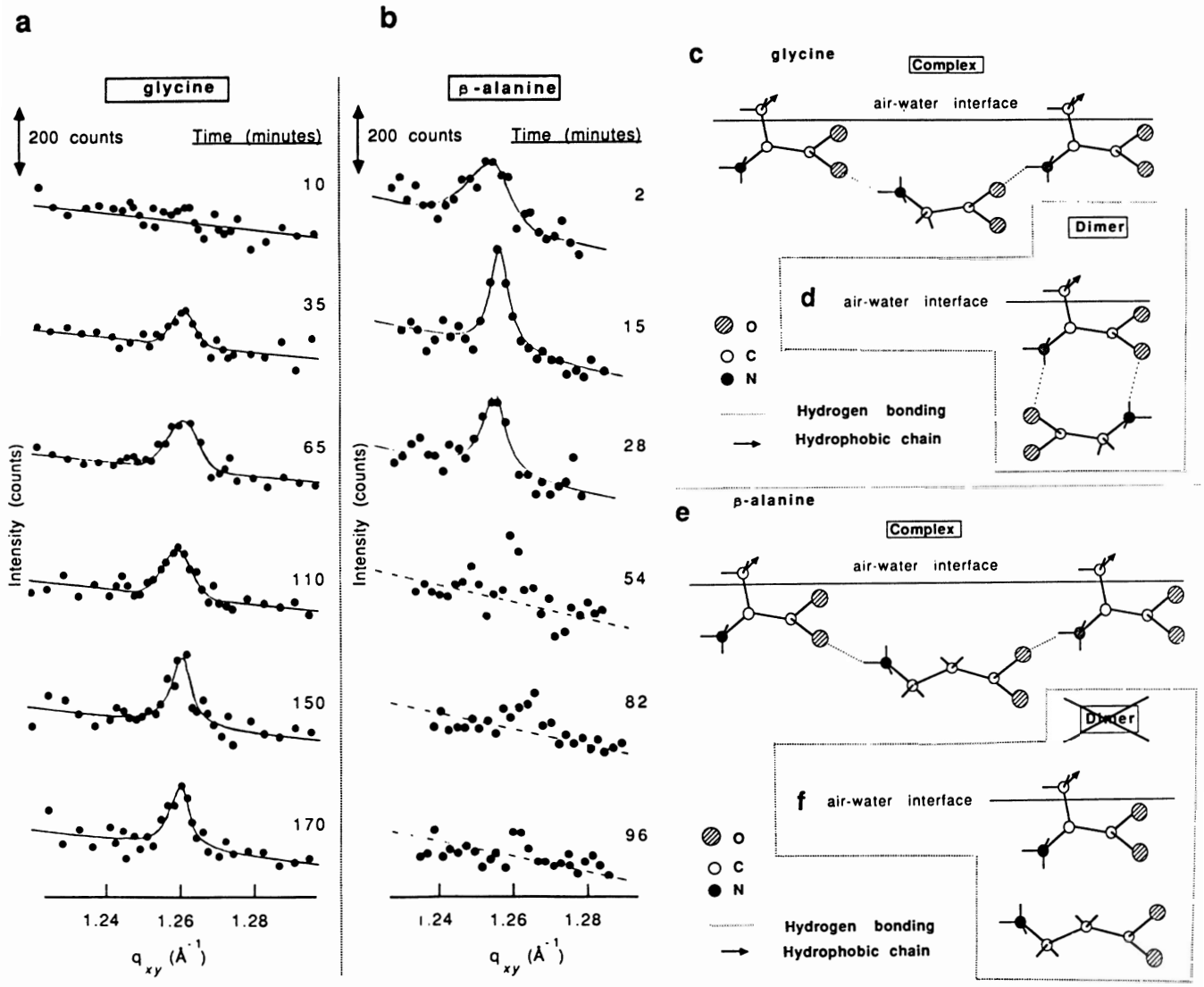

Fig. 34. Uncompressed monolayer of PFA with an average molecular area of 45Å^2. (a,b) GID measurements as a function of time after spreading. (a) Over α-glycine solution (0.015 M). (b) Over β-alanine solution (0.005 M). Note the increase in crystallinity in the former (a), and the decrease in the latter (b) as indicated by the different time evolution of the peak. (c) Schematic drawing of a "bridging complex" between monolayer molecules and the solute molecules: α-glycine. (d) The possibility of quasi dimer formation is also shown. (e) β-alanine solute. This molecule cannot form a quasi dimer with the PFA molecule as illustrated in (f).

results also may provide insight as to how solvents affect the morphology and polymorphic behavior of 3D crystals.

4.2. *Ion binding from solution*

The interfacial region between a charged surface and an electrolyte is central to many processes such as those occurring during electro-deposition, ion transport through biological membranes, prepa-

ration of LB films [6], biomineralization [4] and induced oriented nucleation of inorganic systems [3](c,d) under Langmuir monolayers. X-ray reflectivity measurements demonstrated that metal ions, when present in solution, interact closely with the charged monolayer head groups at the interface [31,86,87,20]. However, the question was still open as to whether the ion distribution near such charged ordered surfaces is crystalline. In a recent study [88](b), the interface between a phospholipid monolayer and a $ZnCl_2$ aqueous solution was measured with X-ray standing waves. The technique is sensitive to the ion distribution normal to the surface and allows one to distinguish between a vertically non-diffuse ionic layer (Helmholtz model) and diffuse ionic layers (Gouy-Chapman and Stern models). The authors concluded that the double layer at the phospholipid membrane-aqueous interface is diffuse along the normal to the film. GID measurements of lead-arachidate [89] monolayers at room temperature did not demonstrate the existence of laterally ordered Pb^{2+} counter-ionic layers but did not directly address the question of the vertical distribution of the ions. Liquid surface EXAFS experiments on manganese-stearate [23,24] films at room temperature yielded a Mn-Mn nearest-neighbor distance at the surface in the compressed phase only, indicating at least short-range order.

A weak indication of lateral ionic order is provided by GID data of uncompressed monolayers of PFA over a HCl solution [50](a) at pH = 1.5. A model was proposed in which the Cl^- ions were partially intercalated between neighboring NH_3^+-CH-CO_2H sites, participating in attractive N-$H^+ \cdots Cl^-$ and CO-H$\cdots Cl^-$ interactions. This model also explains the high molecular area of 31.6 $Å^2$, compared to the value of 28.5 $Å^2$ at high pH (discussed below), which imposes a tilt of the molecule of 25° from the vertical according to the GID data. The model is also in keeping with the observation that in 3D crystals of glycine·HCl, the molecules appear in a layered arrangement with intercalated Cl^- ions [90].

PFA monolayers spread over highly basic KOH subphases (pH = 11.5) yielded results in favor of a laterally ordered bilayer [50](a). The presence of the K^+ ions induces all molecules to be assembled into crystals even in the uncompressed state, with the molecules aligned vertically in a hexagonal cell. According to an analysis of the GID data (Fig. 35a), the K^+ ions occupy ordered sites bridging oxygen atoms of neighboring molecules (Fig. 35b,c). The XR measurements on compressed monolayers at high pH over KOH indicate excess electron density just below the head group. This excess density is consistent with one K^+ ion and one H_2O molecule per head group. Upon compression, lateral pressure introduces defects in the randomly oriented islands, causing a reduction in crystallinity. It is possible that the distortion occurs at the periphery of the crystallites due to strong electrostatic inter-peripheral forces between anion-cation bilayers of neighboring crystallites. It is noteworthy that in both systems the counter-ions maintain the original molecular packing and a long range crystalline order is maintained after decompression. This is in contrast to results observed over pure water [50](a).

As mentioned earlier, lowering the temperature has the effect of reducing molecular rotational disorder and enhancing crystalline self-aggregation. Indeed, a GID study of uncompressed cadmium arachidate monolayers over a subphase with an adjusted pH of 8.8 using ammonia as a base, demonstrated the presence at temperatures lower than 9°C of an ordered Cd ionic layer [91] with a coherence length of 1000 Å. The diffraction pattern showed ten distinct peaks (Fig. 36), seven of which were attributed to a cadmium counterionic layer. The remaining three peaks were deduced to stem from the arachidate layer, on the basis of their Bragg rod profiles and q_{xy} positions and so denoted as the "arachidate triplet". The diffraction peaks of the cadmium lattice whose BR profiles were flat and

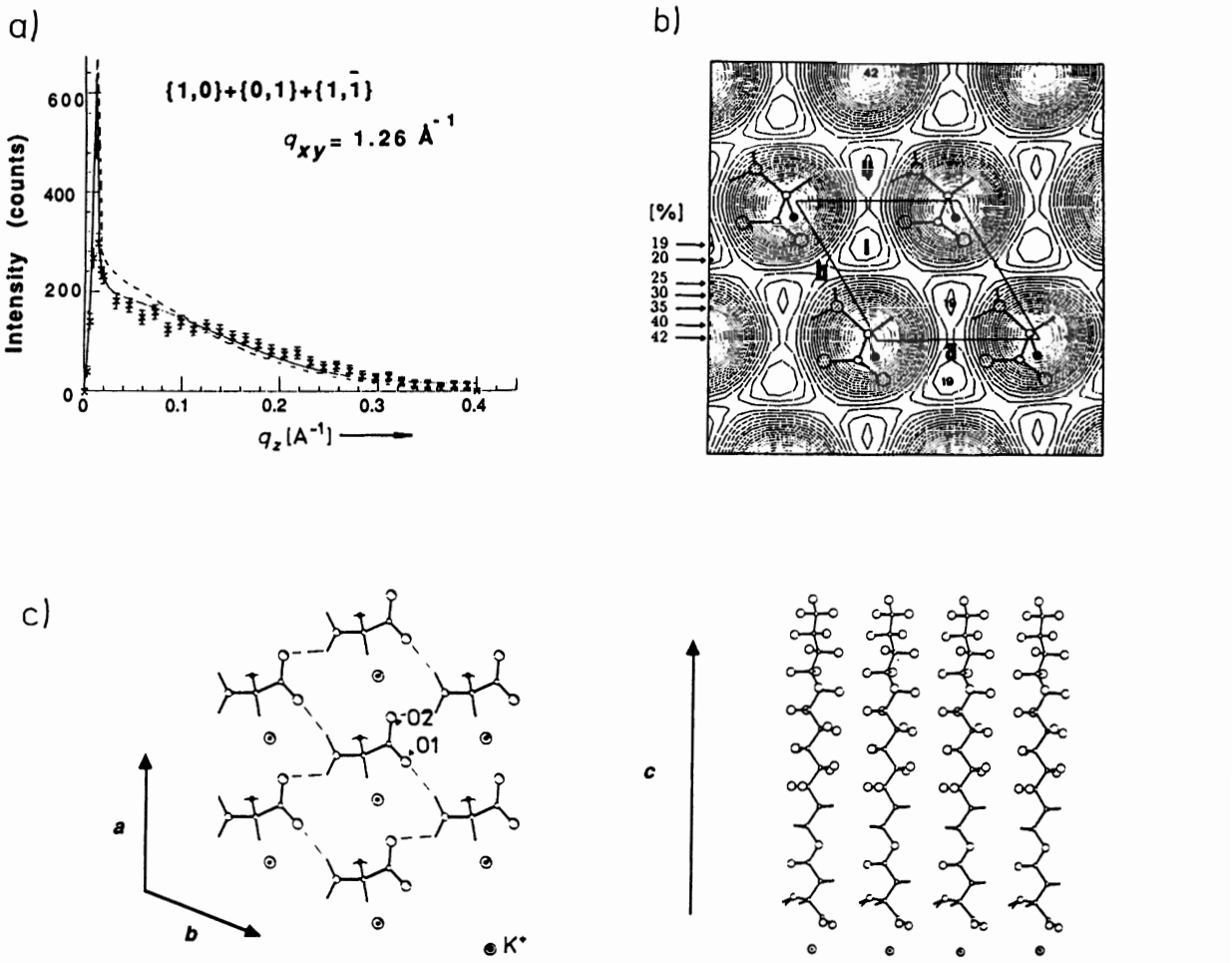

Fig. 35. PFA monolayers over KOH subphases at pH = 11.5, at room temperature and at zero surface pressure. (a) Bragg rod scan measured on the GID peak (whose reflection assignment and position is indicated) with a calculated fit including (solid line) and excluding (dashed line) contribution of K^+ ions. (b) R-factor contour map (interval 1 per cent), which expresses the fit between the calculated and observed data, obtained from BR fits as a function of the lateral position of the K^+ ion in the PFA hexagonal unit cell at a fixed z coordinate. The two sites with the lowest R-factors (19 per cent) labeled I and II, correspond to where the K^+ion is expected to lie. The model (c) favors site I for the K^+ ion. (c) Model of the uncompressed monolayer of PFA over K^+ ions. Left: View perpendicular to the monolayer showing the hexagonal net of K^+ ions. The K^+ ion bridges the oxygen atoms O_1 and O_2 of two neighboring molecules.
Right: View along the *a* axis showing the attached layer of K^+ ions (water molecules possibly interleaved in the ionic layer are not shown here).

extended, indicative of a thin monoatomic layer, could be indexed according to a 2×3 supercell of the arachidate cell. The packing arrangement of the arachidate molecules could be established from a fit to BR profiles of the arachidate triplet. The molecules are arranged in a pseudo-rectangular cell with two independent molecules related by pseudo glide symmetry in the orthogonal O⊥ motif. Specular X-ray reflectivity measurements showed that the molar ratio of cadmium to arachidate is 5:6 or 1:1 so that the counterionic layers must consist essentially of $CdOH^+$ ions [83]. The refined Cd positions in the 2×3 supercell, containing either 5 or 6 cadmium atoms, gave a very good fit to the observed diffraction data, as shown in Fig. 36. The relative positions of the cadmium ions and the arachidate

molecules could not be established with certainty by fitting the BR data of the "triplet".

As opposed to cadmium arachidate, a film of calcium arachidate over water at low temperatures did not provide direct evidence for an ordered Ca^{2+} layer [82]. Nevertheless the Ca^{2+} ions did induce high crystallinity of the uncompressed phase at high pH, with molecules aligned vertically. Possible factors for the absence of X-ray reflections arising from the Ca^{2+} ions comprise the relatively low scattering power of the counterion, or the low occupation density of one ion per unit cell. We should also note a recent surface potential and surface pressure study of ionic interactions with fatty acid monolayers [92]. It was concluded in Ref. [92] that the monolayer ordering is induced by covalent binding of carboxylate (CO_2^-)-metal ions in the case of Cd^{2+} ions, but Ca^{2+} ions do not exhibit such an ordering effect since their interactions with carboxylates are mainly ionic in nature. Structural changes induced in monolayers of heneicosanoic acid ($C_{20}CO_2H$) by the introduction of Cu^{2+} or Ca^{2+} ions into the subphase and variation of *pH* were also studied recently by GID at 5°C [93,94].

5. Transfer of structural information from Langmuir monolayers to crystals

Langmuir monolayers have been shown to induce oriented crystallization from solution of proteins [95,96] and other organic and inorganic compounds [3,4]. As mentioned in the introduction, these studies were motivated by their relevance to crystal nucleation, to two-dimensional ordering at the water surface of soluble hydrophobic molecules and to biomineralization. The crystal systems studied to date include α-glycine [3](a), sodium chloride [3](c,d), calcium carbonate [4](a–d), parahydroxy-benzoic acid [97], hexagonal ice [98,71,61], barium sulphate [99], silver propionate [100], lead sulphite [101] and cadmium sulphite [102]. Mechanisms for the oriented crystallization include structural fits and electrostatic attractions. Information on the monolayers used and the type of crystal face nucleated are listed in Table 3 for some of these crystal systems.

5.1. *Inorganic crystals and biomineralization*

Electrostatic interactions between Langmuir monolayers and crystals have been invoked to account for the oriented growth of inorganic salts. A first example is given by the oriented nucleation of NaCl crystals under α-amino acid monolayers such as PFA. NaCl precipitates from aqueous solution in a cubic cell (a = 5.64 Å) exhibiting six (100) faces. But when crystallized under α-amino acid monolayers at neutral pH, crystals were found to be attached to the monolayer by the less stable (110) face [3](d), [50] (Fig. 37a). The (110) face is composed of alternating rows of Na^+ and Cl^- ions, separated by 2.82 Å. This distance is very close to the separation of 2.8 Å between rows of NH_3^+ and CO_2^- moieties in PFA. Thus we envisage an electrostatic attraction between small domains of a (110) surface layer of NaCl and the zwitterionic α-amino acid head groups of PFA at neutral pH. At high pH (> 10), PFA monolayers induce crystallization of NaCl from the metastable (111) face. A pure (111) face of NaCl exposes a singly charged layer consisting of either Na^+ or Cl^- ions, but not both (Fig. 37b). This induction was explained in terms of a simple electrostatic interaction between the CO_2^- charged monolayer surface and an underlying layer of Na^+ ions which induces a homogeneous surface potential for (111) nucleation. The lattice of the PFA monolayer and that of the (111) layer are not similar. There is a possibility of interleaving ordered water in the first

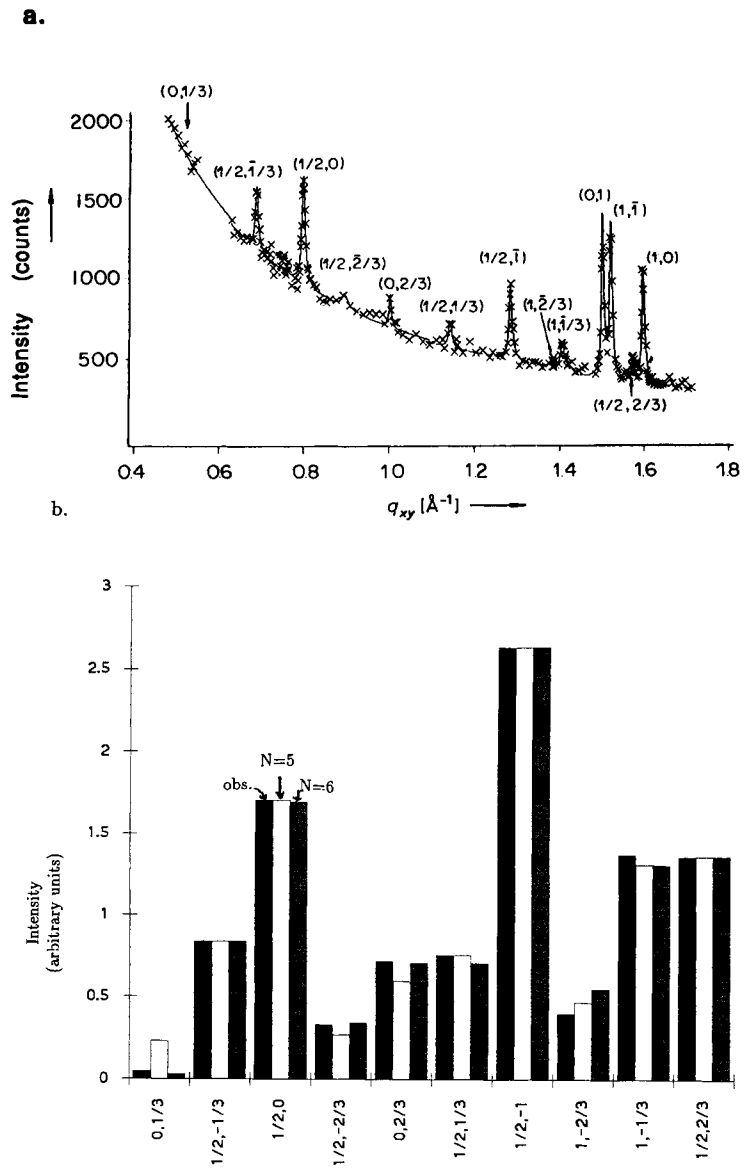

Fig. 36. Arachidic acid monolayer ($C_{19}CO_2H$) over a 10^{-3}M $CdCl_2$ subphase (pH = 8.8) in the uncompressed state and at low temperature (9°C). (a) GID peaks and reflections assignment. The reflections with integer indices correspond to the scattering arising from the arachidate moieties. The reflections with fractional indices correspond to the scattering from a 2D layer of Cd^{2+} ions. (b) GID powder pattern intensities: Observed (black) and calculated for the Cd ion arrangements with $N = 5$ (white) and $N = 6$ (grey) Cd ions in the 2×3 (a_S, b_S) unit cell. The columns represent the normalized integrated intensities. (c) Arachidate and cadmium nets. The cadmium cell (a_S, b_S) is a 2×3 supercell of the arachidate (a', b') cell.

attached layer of Na^+ ions, which could play a role in inducing oriented nucleation of the (111) face since O-H groups can form O-H···Cl^- hydrogen bonds [90] with Cl^- ions in the second layer.

As mentioned earlier, GID results on PFA monolayers over HCl solution at low pH was interpreted in terms of a partial intercalation of Cl^- ions within the head group layer [50]. Thus, rows of positive NH_3^+ and negative Cl^- charges are created at the surface, simulating the repeat motif of the charge distribution in the (110) face. Indeed, at low pH, NaCl crystallizes from its (110) face attached to

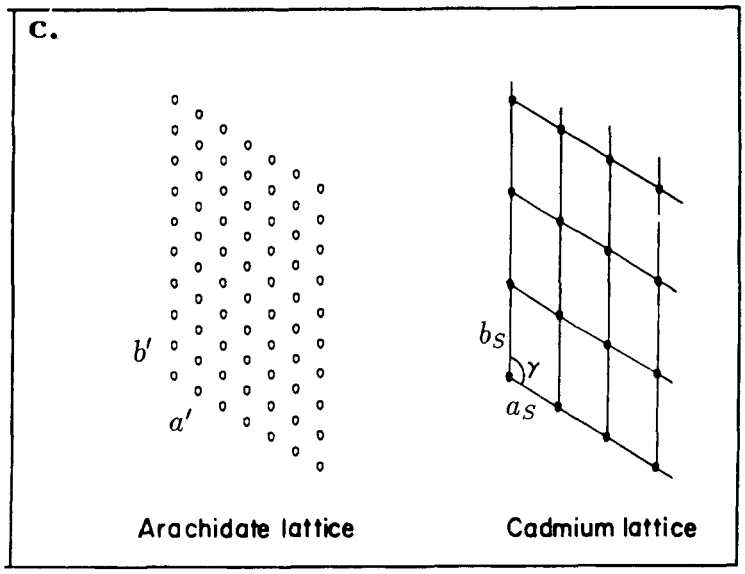

Fig. 36 — continued.

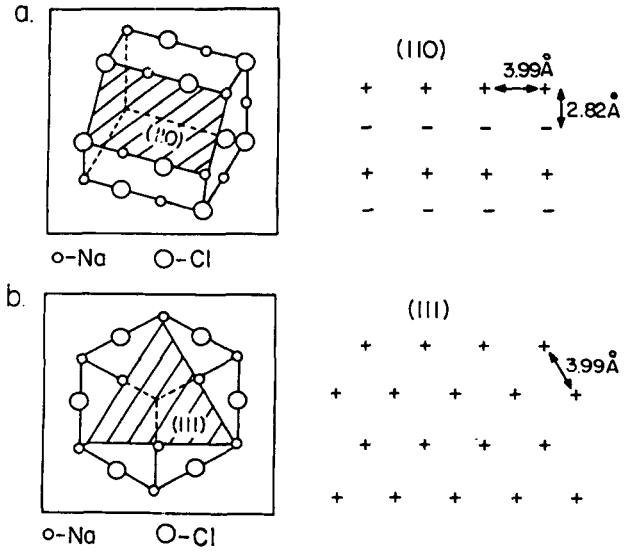

Fig. 37. Schematic representation and point charge distribution of faces of a NaCl crystal. (a) The (110) face. (b) The (111) face.

the PFA monolayer [50].

The influence of structured organic surfaces on oriented growth has a strong bearing on biomineralization. Addadi, Weiner and co-workers [4](e) have studied the effect of β-pleated sheet proteins on the crystallization of calcite. They demonstrated an oriented calcite nucleation probably arising from a combination of electrostatic and structural requirements. In order to elucidate this result on a molecular level, Mann, Heywood and coworkers have studied the induced oriented crystallization of $CaCO_3$ under monolayers of stearic acid [4](a,b) and other amphiphiles such as amines [4](c,d). Whereas crystallization of $CaCO_3$ in the absence of a monolayer of acid or amine results in rhombohedral calcite crystals, the stearic acid monolayers give rise to oriented nucleation of the less stable

Table 3
3D crystals induced by monolayers at the air-water interface

3D crystal	Monolayer[a]	Nature of binding	Crystal face	Refs.
NaCl	Acids and α-amino acids			
High *pH*	$R\text{-}CO_2^-$ $H_2N\text{-}CHR\text{-}CO_2^-$	Electrostatic binding, no match	{111} metastable charged face	[3](c,d)
Neutral *pH*	$H_3^+N\text{-}CHR\text{-}CO_2^-$	Electrostatic binding, partial match	{110} face, less stable than normal {100}	
$CaCO_3$	Acids RCO_2H	Electrostatic binding, partial match for calcite	Calcite: $\{1\bar{1}0\}$ face, vaterite: {001} face	[4](a–d)
	Amines RNH_2		Vaterite: {001} and {110} faces	
α-glycine $H_3^+N\text{-}CH_2CO_2^-$	α-amino acids $H_3^+N\text{-}C^*HR\text{-}CO_2^-$	N-H···O Hydrogen-bonds, structural match	{010} chiral face, not well developed in H_2O	[3]
Para-hydroxybenzoic acid monohydrate $HO_2C\text{-}C_6H_4\text{-}OH+H_2O$	*Para*-alcoxybenzoic acid $HO_2C\text{-}C_6H_4\text{-}OR$	Interlayer contacts induce a structural match	{401} face, not well developed in H_2O	[97]
Ice	Alcohols R-OH	O-H···O hydrogen bonds, lattice plus structural match	{0001} hexagonal face	[98,59,61]

[a] R is a long chain alkyl group of general formula C_nH_{2n+1} .

hexagonal polymorph of vaterite from the (001) face. We present a model for the interface, based on the crystallization results of NaCl and the structural data of cadmium arachidate and calcium arachidate monolayers. The double layer comprising the stearic acid molecules and the calcium ions must be neutral, implying a 1:2 stoichiometry as confirmed by X-ray and neutron reflectivity studies of the fatty acids over $CaCl_2$, $CdCl_2$ solutions [31,86,87,20]. Thus the repeat area per Ca^{2+} ion must be twice that of stearic acid. As mentioned earlier there is as yet no direct evidence of a counte-

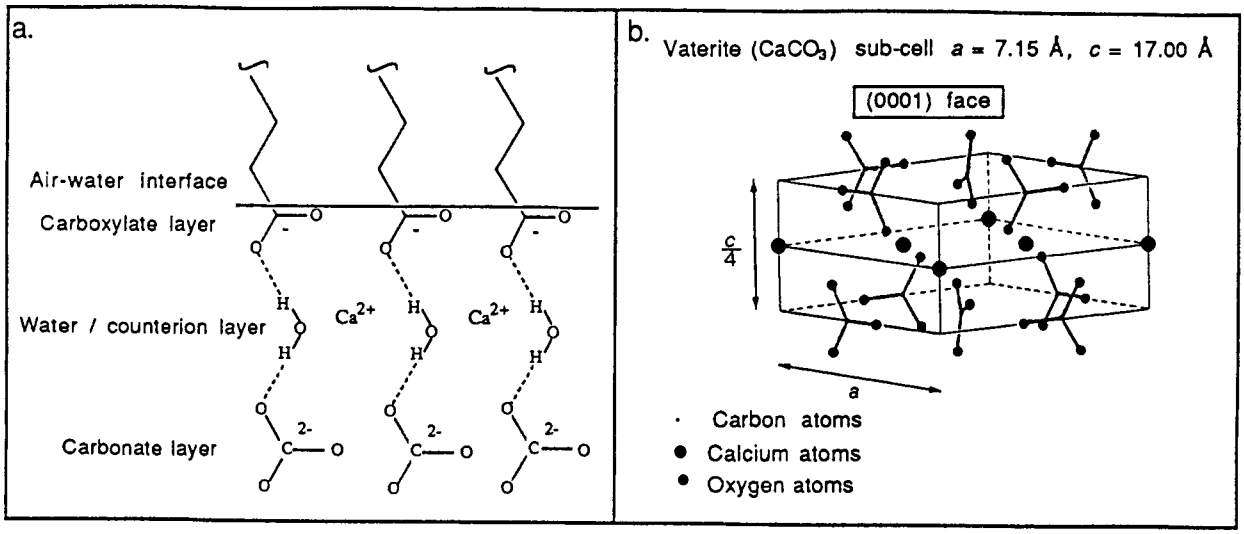

Fig. 38. (a) Schematic representation of a calcium stearate monolayer. A stoichiometry of one calcium ion per two CO_2^- carboxylate moieties is required for charge neutrality. Water molecules interleave in the low density cationic layer and form hydrogen bonds with the carboxylate layer at the interface and with a carbonate layer in the subphase. In this layer the carbonate ions are oriented as in the (0001) layer structure of vaterite. (b) Vaterite sub-cell showing the stereochemical arrangement of the carbonate ions (CO_3^{2-}) perpendicular to the (0001) face (from Ref. [4](a)).

rionic Ca^{2+} layer being ordered. The density of such a Ca^{2+} layer is low and we may assume at least one interleaving water molecules per Ca^{2+} ion as consistent with a model arrangement (based on X-ray reflectivity data) of a monolayer of a calcium salt of a fatty carboxylic acid on water [82]. Such water molecules would screen neighboring Ca^{2+} ions and form O-H···O hydrogen bonds with the monolayer carboxylate groups CO_2^- above and with carbonate ions CO_3^{2-} below the Ca^{2+} layer (Fig. 38a). The hydrogen-bonded O-H···OCO_2^{2-} system tends to be coplanar as in the crystal structure of $Na(CO_3)_2 \cdot 3/2\ H_2O_2$ [103]. This preference would promote bound carbonate molecules oriented perpendicular to the Ca^{2+} layer. Vaterite has a crystal structure with carbonates oriented in this way (Fig. 38b), while the orientation of the carbonates in the calcite structure is different. In this way we may account for the preferred nucleation of vaterite.

A geometric correspondence between monolayer and crystal layer has been invoked by Heywood and Mann for the oriented nucleation of $BaSO_4$ via its (100) face to the long-chain alkyl sulfate or phosphanate monolayers [99]. Fendler and coworkers have reported [101] highly oriented equilateral-triangular crystals of lead sulfite PbS formed by the exposure of arachidic acid monolayer coated over aqueous solution of lead nitrate $Pb(NO_3)_2$ to hydrogen sulfite H_2S. They rationalized the oriented nucleation of PbS from its (111) plane in terms of a structural match between the (111) PbS layer and the 2D lattice of a hexagonal close-packed arachidic acid monolayer.

5.2. *Crystallization of molecules under monolayers with a head group similar to the molecule*

An excellent structural fit between the head groups of the monolayer and the attached crystal layer is illustrated by the α-amino acid monolayer/glycine crystal system (Table 3). Glycine crystallizes in the α-form in a bi-pyramidal habit (Fig. 39a) from aqueous solution in a monoclinic centrosymmetric

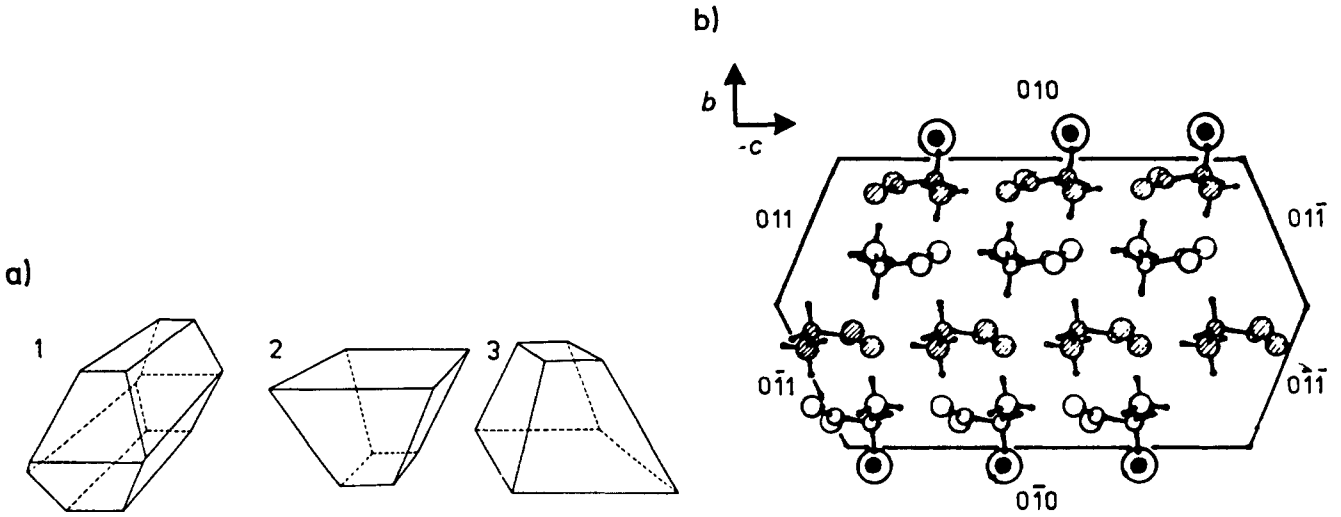

Fig. 39. (a) Morphology of the pure α-glycine crystal grown from (1) aqueous solutions; (2) and (3) at the monolayer solution interface. (b) Crystal structure of α-glycine. An (R) α-amino acid monolayer induces the (010) face. An (S) α-amino acid monolayer induces the (0$\bar{1}$0) face. Both faces are indicated by circled hydrogen atoms.

arrangement. The glycine molecules form hydrogen-bonded layers (Fig. 39b). Such a layer may be easily replaced by a monolayer of chiral resolved α-amino acid surfactant molecules provided the cross-sectional area of its hydrophobic chain is smaller or equal to that of glycine (25.5 Å^2). Indeed α-glycine crystals grow stereospecifically from several α-amino acid Langmuir monolayers whose hydrophobic chains meet the above criterion [3](a,b). For example the packing arrangement of the glycine head groups of the monolayer of PL (Fig. 21), whose GID pattern [48] is shown in Fig. 20c, fits very well to the layer structure of glycine.

The epitaxial crystallization of para-hydroxy benzoic acid (Table 3) under monolayers of para-alkoxy benzoic acid provides an example of how the molecules in solution impose a change of monolayer structure probably at the onset of crystal nucleation. The para-hydroxy benzoic acid head groups of the monolayer bound to the solute molecules change their orientation with respect to the hydrocarbon chains, so as to lie flat on the water surface, thus mimicking the {401} surface layer of the para-hydroxy benzoic acid crystal. It is noteworthy, in analogy to the α-glycine/monolayer system, that the crystals grown from solution without monolayer do not exhibit well developed {401} faces.

5.3. Nucleation of ice by monolayers

Pure water can be supercooled to temperatures as low as -40°C. Therefore the induction or inhibition of the nucleation of ice, in particular through the role of auxiliaries such as membranes or proteins, has far-reaching ramifications for both the living and non-living world. Promotion of ice nucleation has been exploited for the induced precipitation of rain by clouds seeded with silver iodide [104]. On the other hand, the promotion of ice nucleation by frost bacteria in crops can result in wide scale damage [105].

Several mechanisms have been proposed to explain the promotion of ice nucleation such as a lattice or structural match between the substrate and the nucleated ice crystal [106] or an electric field present

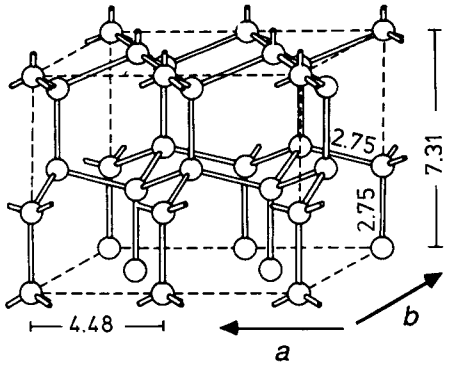

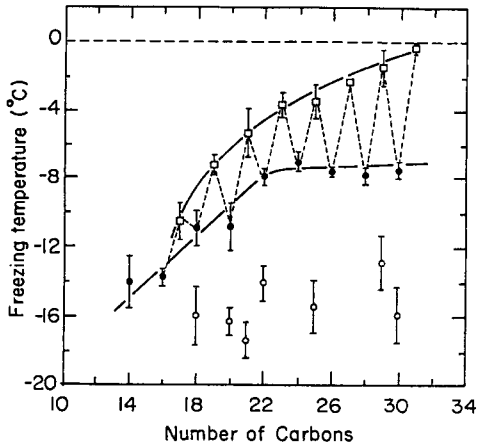

Fig. 40. Crystal structure of hexagonal ice (from [105](b)). The oxygen atoms of each water molecule are denoted by spheres and the disordered O-H···O hydrogen bonds by rods. The hexagonal axes $a = b = 4.48$ Å and $c = 7.31$ Å are indicated.

Fig. 41. Freezing points of drops of supercooled water covered by monolayers of alcohols C_nOH (n even • and n odd □) and carboxylic acids C_nCO_2H (○). Freezing point curves are drawn separately for alcohols with n odd and n even. The error bars for each point were derived from 10 to 20 freezing point measurements.

in the substrate which orients the water molecules [107]. Here we review experiments which were conducted in order to design two-dimensional surfaces which raise the ice nucleation temperature [98,61]. These experiments involved the freezing of drops of water covered with monolayers of aliphatic alcohols (C_nOH) or carboxylic acids (C_nCO_2H). The structure of hexagonal ice [108] may be described for the oxygen atoms in terms of layers parallel to the ab plane where $a = b = 4.5$ Å, $\gamma = 120°$ (Fig. 40). Advantage was taken of the observation that uncompressed Langmuir monolayers of $C_{23}OH$, $C_{30}OH$ and $C_{31}OH$ over water are highly crystalline, as reviewed in Section 3.3. Moreover the OH head groups pack essentially in a distorted hexagonal net [58,59] ($a = b = 4.5$ Å, $\gamma = 113°$) at 5°C which is similar in dimension to the ab lattice of hexagonal ice at 0°C. The largest mismatch between the two lattices is 10 per cent along the $a + b$ diagonal. The uncompressed monolayer of the carboxylic acid $C_{29}CO_2H$ has axial dimensions [58] $a = b = 4.6$ Å, $\gamma = 107°$. For this system the largest mismatch to ice is, once again, in the $a + b$ direction, with a value of 27 per cent. A structural similarity can be proposed for the OH head groups of the alcohol monolayer and the ab layer structure of ice, but no such similarity exists for the corresponding carboxyl head groups of the fatty acid monolayer.

The results of the ice nucleation temperature ("freezing point") measurements (Fig. 41) show that aliphatic chain alcohols are more efficient ice nucleators than the corresponding carboxylic acids [98,61]. Moreover the "freezing point" is sensitive not only to chain length but also to the chain parity (*i.e.*, n odd or even) of the alcohol $C_nH_{2n+1}OH$ (Fig. 41). This trend suggests that, at the temperature of ice nucleation, the arrangement of the alcohol OH groups in the odd and even analogues are not the same. The role played by the systems C_nOH ($n = 16, 20, 23, 30, 31$) and $C_{19}CO_2C_nOH$ ($n = 9, 10$) for induced ice nucleation is discussed in three papers [59,71,61] in terms of 2D crystalline coherence length, lattice and structural match to ice and orientation of the alcohol OH head groups.

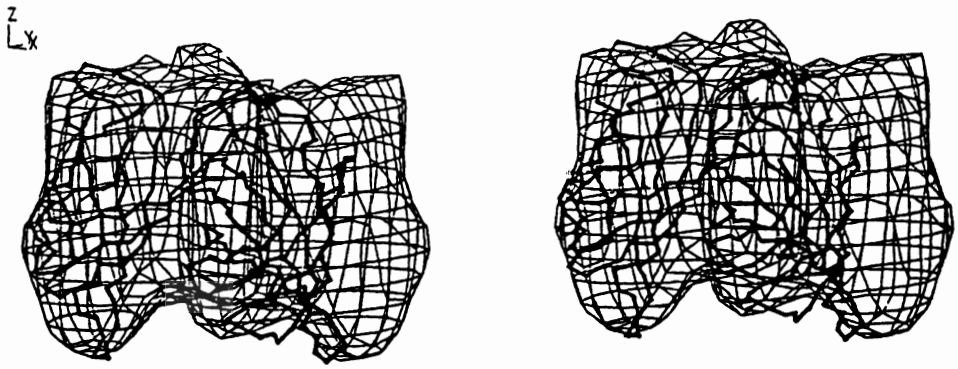

Fig. 42. Stereo view of a computer-generated model of a single streptavidin tetramer viewed at an oblique angle from above the lipid layer as revealed by electron microscopy. The α-carbon backbones of two subunits of the streptavidin tetramer, determined by X-ray crystallography are superimposed (*thick lines*) to illustrate the close match between the structures determined by the different methods. The other two subunits of the X-ray structure are omitted for clarity.

5.4. Two-dimensional crystallization of proteins under lipid monolayers

The structures of, and interactions between, proteins and lipids at the air/water interface have been investigated by optical and electron microscopy [109,95]. In electron microscopy studies [95], Kornberg, Ribi and co-workers have demonstrated, by image processing of the electron micrographs, that 2D crystals of the protein are readily formed at the air-water interface under lipid monolayers. The bound proteins are concentrated and oriented in two dimensions by virtue of specific binding and the freedom to move into regular lattice sites due to the lateral diffusion of lipids in the films. With this approach a variety of protein structures have been studied, some at about 20Å resolution. These include an anti-dinitrophenyl antibody bound to a lipid-linked dinitrophenyl group [95](b), a ribonucleatide reductase bound to a lipid-linked dATP [95](c), and a cholera toxin receptor complex [95](d). Non specific binding through purely electrostatic interactions was found to induce 2D crystallization of an *E.Coli* RNA-polymerase holoenzyme on a charged lipid layer [95](e).

The protein-lipid structure at the air-water interface has also been directly characterized by fluorescence microscopy; Ringsdorf and coworkers have shown the formation of large domains of streptavidin on biotinylated lipid monolayers [96]. The 2D crystallinity of these protein domains was then proven by electron diffraction [110]. The resulting low-resolution (20Å) structure corresponded well with the 3D structure determined by X-ray diffraction [111], as depicted in Fig. 42. The relation between 2D crystal morphology and molecular structure in streptavidin monolayers crystallized on charged lipid layers was addressed in [95](f).

In all these electron microscopy studies, the lipid-protein layer was transferred onto electron microscope grids and were stained. In contrast, the structure at the air-water interface of the streptavidin / biotinylated lipid complex layer has been recently studied *in situ* using combined X-ray and neutron reflectivity [112,113]. The X-ray and neutron data for both heavy and light water subphases are given in Fig. 43. In adding (protonated) streptavidin to the subphase the neutron reflectivity decreases for heavy water subphase but increases for a light water subphase, consistent in both cases with binding of streptavidin to the dilute biotin monolayer [112]. Quantitative analysis of the results with four different contrasts (X-rays/neutrons; subphase of light or heavy water; fits indicated by the full lines in Fig. 43) gave [113] an area per protein molecule of $4600 \pm 1000 Å^2$ and an effective thickness of

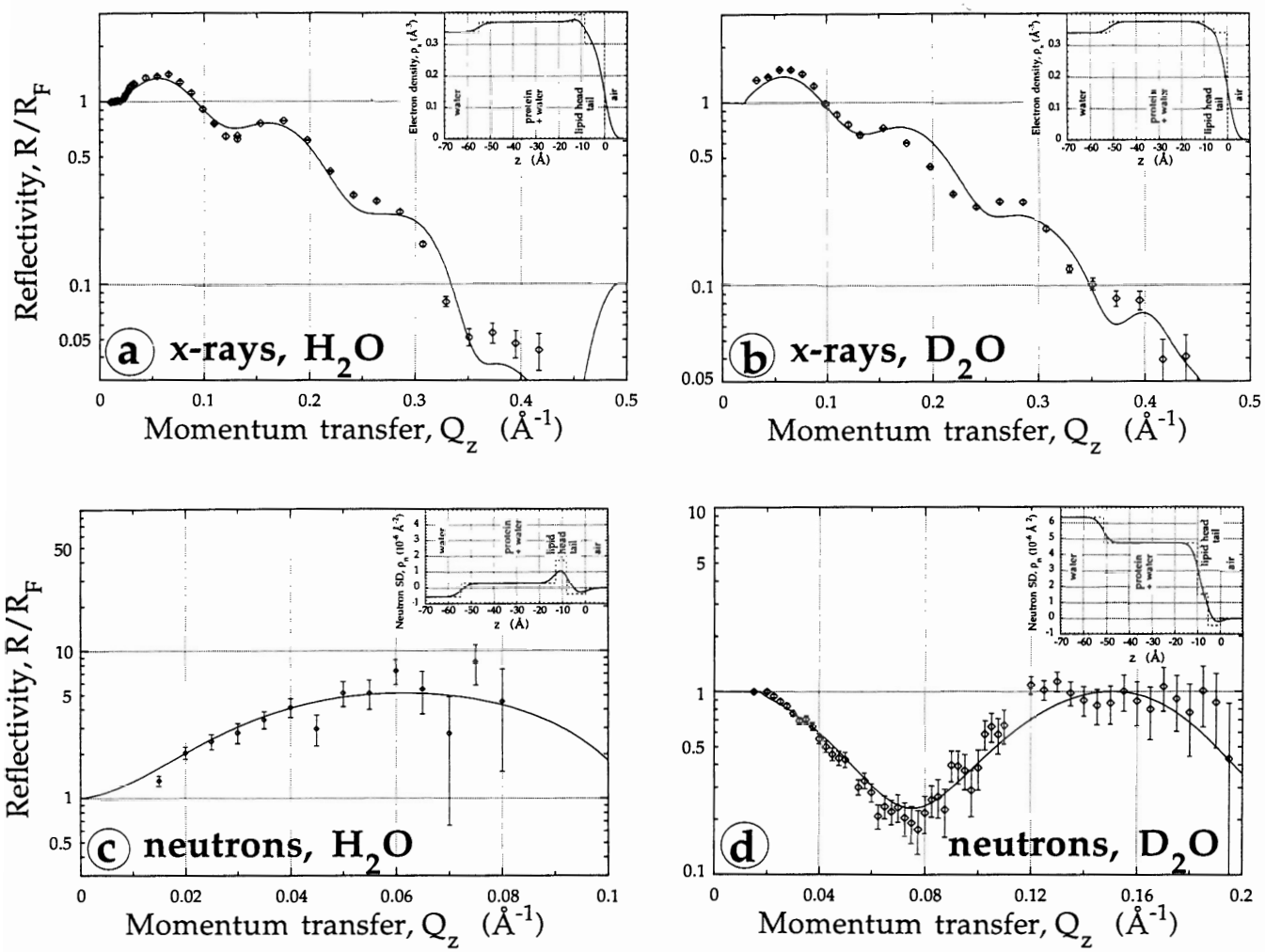

Fig. 43. Normalized X-ray (a,b) or neutron (c,d) reflectivities from monolayers of streptavidin after binding to a dilute biotin lipid monolayer over a 0.5 NaCl solution of D_2O (a,c) or H_2O (b,d). The solid line corresponds to the best fit to all four data sets of a single model. The inserts show the corresponding scattering length densities.

42±2Å. The combined reflectivity data also showed that the protein compartment is interpenetrated by 4200±1500 molecules of water per streptavidin, so that the "dry"volume of the protein is only 66000±6000 Å^3. We note that with the neutron data only, an ambiguity remained unresolved in the model derived [112]. Combination with X-ray data however lead to a unique model [113]. In further experiments [114,115] spacer groups were inserted between the lipid and the biotin moiety in order to relax the coupling between the lipid and protein monolayers, and the ensuing influence on the structure of the protein monolayer was investigated by neutron reflection.

6. Outlook

The study of structures at interfaces has received an enormous boost with the recent development of surface X-ray diffraction methods using synchrotron radiation. Research in the crystallography of

thin organic films will hopefully encompass a variety of exotic projects. For example, so far all the studies have been directed towards amphiphilic molecules bearing long hydrocarbon or fluorocarbon chains. With the present advances in synchrotron techniques, it may soon be possible to obtain diffraction patterns from monolayer aggregates at the air-water interface of water-soluble amphiphilic molecules. Experimental results from oriented crystallization, chemical reactivity and spectroscopic measurements suggest that molecules such as short chain α-amino acids, benzoic or cinnamic acids form ordered clusters at the air-water interface [5,116].

The X-ray methods should allow one to test for the presence of lateral crystalline order in monolayers consisting of a collection of molecules engineered to construct a desired and well-defined lattice. Thus, these methods are intimately linked to the development of techniques to control and perfect the structure of Langmuir films on the molecular level. It might also become possible to obtain a deeper insight into chemical transformation at the air-water interface by correlating the packing structure of reactant and product. An example of the latter is the topochemical photo-polymerization of diacetylenes in monomolecular layers as studied by Göbel et al. [117,118]. Another natural extension of these studies is the investigation of packing arrangements of amphiphilic molecules at organic solvents-water interfaces, as in emulsions. In such a system, the surface created by the terminal groups of the hydrophobic chains makes van der Waals contacts with the organic solvent such as an alkane in a bilayer membrane.

The X-ray and neutron methods are also applicable to complex biological systems at interfaces which may involve enzymatic transformations or antigen-antibody interactions and complement the elegant studies by Kornberg [95], Ringsdorf [96] and others who monitored by electron-microscopic and fluorescence methods the dynamics of these systems. Hopefully, deeper insight in some of these systems may be obtained by diffraction studies.

So far, most of the experiments have been carried out with "2D powders" at the smooth air-water interface. It is also possible to study the structure of thin organic films deposited on smooth solid supports [119](a). Recently, the structure of self-assembled monolayers on smooth mica coated with gold has been determined in great detail [119](b). One may also anticipate, in the not too distant future, the possibility to obtain diffraction patterns from single crystals of these amphiphilic molecules and so provide structural information almost at atomic resolution.

Acknowledgement

We thank Isabella Weissbuch, Ronit Popovitz-Biro and Susan Weinbach for fruitful discussions. We acknowledge financial support from the German Israeli Foundation (GIF), the U.S.A.-Israel Binational Foundation, Jerusalem, the Petroleum Research Fund, the American Chemical Society, the Israel Academy of Sciences, the Danish Foundation for Natural Sciences and HASYLAB, DESY, Hamburg, Germany for beam time. We are grateful to M. Kloster who patiently typed several versions of this article.

References

[1] I. Langmuir, J. Am. Chem. Soc. 39 (1917) 1848.

[2] J.D. Swalen, D.L. Allara, J.D. Andrade, E.A. Chandross, S. Garrof, J. Israelachvili, T.J. McCarthy, R. Munray, R.F. Pease, J.F. Rabolt, K.J. Wynne, H. Yu, Langmuir 3 (1987) 932.

[3] (a) E.M. Landau, M. Levanon, L. Leiserowitz, M. Lahav, J. Sagiv, Nature 318 (1985) 353;
(b) E.M. Landau, S. Grayer Wolf, M. Levanon, L. Leiserowitz, M. Lahav, J. Sagiv, J. Am. Chem. Soc. 111 (1989) 1436;
(c) E.M. Landau, S. Grayer Wolf, J. Sagiv, M. Deutsch, K. Kjaer, J. Als-Nielsen, L. Leiserowitz, M. Lahav, Pure & Appl. Chem. 61 (1989) 673;
(d) E.M. Landau, R. Popovitz-Biro, M. Levanon, L. Leiserowitz, M. Lahav, Mol. Cryst. Liq. Cryst. 134 (1986) 323;
(e) R. Popovitz-Biro, I. Weissbuch, D. Jacquemain, F. Leveiller, L. Leiserowitz, M. Lahav, in Butterworth-Heinemann, J. Garside, R. J. Davey, A.G. Jones (Eds.), Advances in Industrial Crystallization (1991) p. 3.

[4] (a) S. Mann, B.R. Heywood, S. Rajam, J.D. Birchall, Nature 334 (1988) 692;
(b) S. Mann, Nature 332 (1988) 119;
(c) S. Rajam, B.R. Heywood, J. B.A. Walker, S. Mann, R.J. Davey, J.D. Birchall, J. Chem. Soc. Faraday Trans. 87 (1991) 727;
(d) B.R. Heywood, S. Rajam, S. Mann, J. Chem. Soc. Faraday Trans. 87 (1991) 735;
(e) L. Addadi, J. Moradian, E. Shay, N.G. Maroudas, S. Weiner, Proc. Natl. Acad. Sci. U.S.A. 84 (1987) 2732.

[5] (a) I. Weissbuch, L. Addadi, Z. Berkovitch-Yellin, E. Gati, M. Lahav, L. Leiserowitz, Nature 310 (1984) 161;
(b) I. Weissbuch, L. Addadi, L. Leiserowitz, M. Lahav, J. Am. Chem. Soc. 110 (1988) 561;
(c) I. Weissbuch, F. Frolow, L. Addadi, M. Lahav, L. Leiserowitz, J. Am. Chem. Soc. 112 (1990) 7718.

[6] H. Kuhn, D. Möbius, Angew. Chem. 83 (1971) 672.

[7] (a) L.M. Blinov, N.V. Dubinin, L.V. Mikhnev, S.G. Yudin, Thin Solid Films 120 (1984) 161;
(b) T. Richardson, G.G. Roberts, M.E.C. Polywka, S.G. Davies, Thin Solid Films 160 (1988) 231;
(c) G.G. Roberts, B. Holcroft, A. Barraud, J. Richard, Thin Solid Films 160 (1988) 53.

[8] (a) I.R. Girling, P.V. Kolinsky, N.A. Cade, J.D. Earls, I.R. Peterson, Optics Commun. 55 (1985) 289;
(b) J.D. Swalen, Thin Solid Films 160 (1988) 197;
(c) W. Groh, D. Lupo, H. Sixl, Angew. Chem. Adv. Mater. 28 (1989) 11;
(d) Y.R. Shen in R.B. Hall, A.B. Ellis (Eds.), New Laser and Optical Investigations of Chemistry and Structure at Interfaces (Verlag-Chemie, Weinheim, 1986) p. 151;
(e) H. Fuchs, H. Ohst, W. Prass, Adv. Mater. 3 (1991) 10.

[9] (a) G.G. Roberts, K.P. Paude, W.A. Barlow, Proc. Inst. Electr. Eng. Part I 125 (1978) 169;
(b) T. Morizumi, Thin Solid Films 160 (1988) 413.

[10] G. Gaines, Insoluble monolayers at the Liquid-Gas Interface (Interscience, New York, 1966).

[11] (a) T.F. Heinz, C.K. Chen, D. Ricard, Y.R. Shen, Phys. Rev. Lett. 48 (1982) 478;
(b) Th. Rasing, Y.R. Shen, H.W. Kim, S. Grubb, Phys. Rev. Lett. 55 (1985) 2903;
(c) T. Rasing, G. Berkovic, Y.R. Shen, S.G. Grubb, M. W. Kim, Chem. Phys. Lett. 130 (1986) 1.

[12] (a) D.L. Allara, R.G. Nuzzo, Langmuir 1 (1985) 52;
(b) J. Gun, R. Iscovici, J. Sagiv, J. Colloid Interface Sci. 101 (1984) 201.

[13] (a) R.M. Weis, H.M. McConnell, Nature 310 (1984) 47;
(b) V.T. Moy, D.J. Keller, H.E. Graub, H.M. McConnell, J. Phys. Chem. 90 (1986) 3198;
(c) M. Lösche, E. Sachmann, H. Möhwald, Ber Bunsenges. Phys. Chem. 87 (1983) 848;
(d) C.A. Helm, H. Möhwald, J. Phys. Chem. 92 (1988) 1262. e) C.M. Knobler, Science 249 (1990) 870.

[14] M. Lundquist, Prog. Chem. Fats Other Lipids 16 (1978) 101.

[15] J. Als-Nielsen, in: Neutrons and Synchrotron Radiation for Condensed Matter Studies, vol. I, J. Barouchel, J.L. Hodeau, M.S. Lehmann, J. R. Regnard, C. Schlenker, (Eds.), Chapter I.1. Les Editions de Physique (Springer-Verlag, 1992).

[16] J. Als-Nielsen, H. Möhwald, in: Handbook on Synchrotron Radiation, Vol. IV, S. Ebashi, E. Rubenstein, M. Koch (Eds.) (North-Holland, Amsterdam, 1991).

[17] J. Als-Nielsen, K. Kjaer, in: Proceedings of the NATO Advanced Study Institute, Phase Transitions in Soft Condensed Matter, Series B, Vol. 211, T. Riste, D. Sherrington (Eds.) (Plenum Press, New York, 1989) p. 113.

[18] (a) A. Braslau, M. Deutsch. P.S. Pershan, A.H. Weiss, J. Als-Nielsen, J. Bohr, Phys. Rev. Lett. 54 (1985) 114;
(b) A. Braslau, P.S. Pershan, G. Swislow, B.M. Ocko, J. Als-Nielsen, Phys. Rev. A 38 (1988) 2457;
(c) M.K. Sanyal, S.K. Sinha, K.G. Huang, B.M. Ocko, Phys. Rev. Lett. 66 (1991) 628.
[19] K. Kjaer, Proceedings of the 3rd International Conference on Surface X-ray and Neutron Scattering, Dubna, Russia, June 24–29, 1993, Physica B 198 (1994) 100.
[20] J. Daillant, L. Bosio, J. J. Benattar, J. Meunier, Europhys. Lett. 8 (1989) 453.
[21] J. Daillant, L. Bosio, B. Harzallah, J. J. Benattar, J. Phys. II (Paris) 1 (1991) 149.
[22] J. Als-Nielsen, in: Handbook of Synchrotron Radiation, Vol. 3 (Elsevier Science B.V., 1991) p. 471.
[23] J. M. Bloch, P. Eisenberger, Nucl. Instrum. Meth. B 31 (1988) 468.
[24] J. M. Bloch, W. B. Yun, X. Yang, M. Ramanathan, P. A. Montano, C. Capasso, Phys. Rev. Lett. 61 (1988) 2941.
[25] R. S. Becker, J. A. Golovchenko, J. R. Patel, Phys. Rev. Lett. 50 (1983) 153.
[26] J. Daillant, L. Bosio, J. J. Benattar, C. Blot, Langmuir 7 (1991) 611.
[27] L. G. Parratt, Phys. Rev. 95 (1954) 359.
[28] S.W. Barton, B.N. Thomas, E.B. Flom, S.A. Rice, B. Lin, J.B. Peng, J.B. Ketterson, P. Dutta, J. Chem. Phys. 89 (1988) 2257.
[29] M. C. Shih, T. M. Bohanon, J. M. Mikrut, P. Zschack, P. Dutta, J. Chem. Phys. 97 (1992) 4485.
[30] P. Tippmann-Krayer, H. Möhwald, Langmuir 7 (1991) 2303.
[31] K. Kjaer, J. Als-Nielsen, C.A. Helm, P. Tippman-Krayer, H. Möhwald, J. Phys. Chem. 93 (1989) 3200.
[32] B. Lin, M.C. Shih, T.M. Bohanon, G.E. Ice, P. Dutta, Phys. Rev. Lett. 65 (1990) 191.
[33] R.M. Kenn, C. Böhm, A.M. Bibo, I.R. Peterson, H. Möhwald, K. Kjaer, J. Als-Nielsen, J. Phys. Chem. 95 (1991) 2092.
[34] Z. Berkovitch-Yellin, L. Leiserowitz, J. Am. Chem. Soc. 104 (1982) 4052.
[35] K. Kjaer, J. Als-Nielsen, C.A. Helm, L.A. Laxhuber, H. Möhwald, Phys. Rev. Lett. 58 (1987) 2224.
[36] C.A. Helm, H. Möhwald, K. Kjaer, J. Als-Nielsen, Biophys. J. 52 (1987) 381.
[37] C.A. Helm, H. Möhwald, K. Kjaer, J. Als-Nielsen, Europhys. Lett. 4 (1987) 697.
[38] C.A. Helm, P. Tippman-Krayer, H. Möhwald, J. Als-Nielsen, K. Kjaer, Biophys. J. 60 (1991) 1457.
[39] H. Möhwald, R. M. Kenn, D. Degenhardt, K. Kjaer, J. Als-Nielsen, Physica A 168 (1990) 127.
[40] C. A. Helm, P. Tippmann-Krayer, R. M. Kenn, H. Möhwald, J. Als-Nielsen, K. Kjær, in: Surface X-Ray and Neutron Scattering, Proceedings of the 2nd International Conference, H. Zabel, I. K. Robinson, (Eds.) (Physik Centrum, Bad Honnef, Germany), Springer Proceedings in Physics, Vol. 61 (Springer-Verlag, June 1992), pp. 147–149.
[41] C. Böhm, H. Möhwald, L. Leiserowitz, J. Als-Nielsen, K. Kjaer Biophys. J. 64 (1993) 553.
[42] D. Vaknin, K. Kjaer, J. Als-Nielsen, M. Lösche, Proceedings of the ECOF-90, Die Macromolekulare Chemie, Macromol. Symp. 46 (1991) 383.
[43] D. Vaknin, K. Kjaer, J. Als-Nielsen, M. Lösche, Biophys J. 59 (1991) 3125.
[44] C. Böhm, H. Möhwald, L. Leiserowitz, J. Als-Nielsen, K. Kjaer, work in progress (1994).
[45] M. Elder, P. Hitchcock, R. Mason, G.G. Shipley, Proc. R. Soc. London Ser. A 354 (1977) 157.
[46] H.-P. Weber, R.K. McMullan, S. Swaminathan, B.M. Craven, Acta Cryst. B 40 (1984) 506.
[47] C. Böhm, Thesis, Mainz University, Germany (1993).
[48] S. Grayer Wolf, L. Leiserowitz, M. Lahav, M. Deutsch, K. Kjaer, J. Als-Nielsen, Nature 328 (1987) 63.
[49] (a) S. Grayer Wolf, M. Deutsch, E.M. Landau, M. Lahav, L. Leiserowitz, K. Kjaer, J. Als-Nielsen, Science 242 (1988) 1286;
(b) D. Jacquemain, S. Grayer Wolf, F. Leveiller, M. Lahav, L. Leiserowitz, M. Deutsch, K. Kjaer, J. Als-Nielsen, Colloq. Phys. 50 (No. C7) (1989) 29.
[50] (a) D. Jacquemain, S. Grayer Wolf, F. Leveiller, M. Lahav, L. Leiserowitz, M. Deutsch, K. Kjaer, J. Als-Nielsen, J. Am. Chem. Soc. 112 (1990) 7724;
(b) D. Jacquemain, Ph. D. thesis, Feinberg Graduate School, The Weizmann Institute of Science, Rehovot, Israel (1992).
[51] (a) S. Grayer Wolf, E.M. Landau, M. Lahav, L. Leiserowitz, M. Deutsch, K. Kjaer, J. Als-Nielsen, Thin Solid Films 159 (1988) 29;
(b) S. Grayer Wolf, Ph. D. Thesis, Feinberg Graduate School, The Weizmann Institute of Science (1991);
(c) S. Grayer Wolf, unpublished results.
[52] B. Di Blasio, C. Pedone, A. Sirigu, Acta Cryst. B 31 (1975) 601.

[53] E. Benedetti, C. Pedone, A. Sirigu, Acta Cryst. B 29 (1973) 730.
[54] M. Mallikarjunan, S. Thyagarajarao, Acta Cryst. B 25 (1969) 296.
[55] M.S. Lehmann, T.F. Koetzle, W.C. Hamilton, J. Am. Chem. Soc. 94 (1972) 2657.
[56] J. Donohue, J. Am. Chem. Soc. 72 (1950) 949.
[57] T. Bohanon, B. Lin, M. Shih, G. Ice, P. Dutta, Phys. Rev. B 41 (1990) 4846.
[58] D. Jacquemain, F. Leveiller, S.P. Weinbach, M. Lahav, L. Leiserowitz, K. Kjaer, J. Als-Nielsen, J. Am. Chem. Soc. 113 (1991) 7684.
[59] J.-L. Wang, F. Leveiller, D. Jacquemain, K. Kjaer, J. Als-Nielsen, M. Lahav, L. Leiserowitz, J. Am. Chem. Soc. 116 (1994) 1192.
[60] Annual Progress Report of the Solid State Physics Department, Risø National Laboratory, DK-4000 Roskilde, Denmark. Risø-R-660, p. 84ff. (1992) and to be published.
[61] R. Popowitz-Biro, J. L. Wang, J. Majewski, E. Shavit, L. Leiserowitz, M. Lahav, J. Am. Chem. Soc. 116 (1994) 1179 .
[62] (a) S. Ställberg-Stenhagen, E. Stenhagen, Nature 156 (1945) 239;
(b) E. Stenhagen, in: Determination of Organic Structures by Physical Methods, E.A. Braude, F.C. Nachod (Eds.) (Academic Press, New York, 1955);
(c) A.M. Bibo, I.R. Peterson, Adv. Mat. 2 (1990) 309.
[63] M.L. Schlossmann, D.K. Schwartz, P.S. Pershan, E.H. Kawamoto, G. J. Kellog, S. Lee, Phys. Rev. Lett. 66 (1991) 1599.
[64] D. K. Schwartz, M. L. Schlossman, P. S. Pershan, J. Chem. Phys. 96 (1992) 2356.
[65] D.M. Small, The Physical Chemistry of Lipids, Handbook of Lipid Research, Vol.4 (Plenum Press, 1986).
[66] (a) E.M. Lee, R.K. Thomas, J. Penfold, R.C. Wood, J. Phys. Chem. 93 (1989) 381;
(b) J.E. Bradley, E.M. Lee, R.K. Thomas, A.J. Willat, D.P. Gregory, J. Penfold, R.C. Ward, A. Waschkosky, Langmuir 4 (1988) 821.
[67] B. Berge, L. Faucheux, K. Schwab, A. Libchaber, Nature 350 (1991) 322.
[68] D.A. Dixon, F.A. van Catledge, B.E. Smart, Abstracts of the 9th International Union of Physical and Applied Chemistry Conference on Physical and Organic Chemistry (1988) p. A15.
[69] S. W. Barton, A. Goudot, O. Bouloussa, F. Rondelez, B. Lin, F. Novak, A. Acero, S. A. Rice, J. Chem. Phys. 96 (1992) 1343 .
[70] D. Jacquemain, S. Grayer Wolf, F. Leveiller, M. Eisenstein, F. Frolow, M. Lahav, L. Leiserowitz, J. Am. Chem. Soc. 114 (1992) 9983.
[71] J. Majewski, R. Popovitz-Biro, K. Kjaer, J. Als-Nielsen, M. Lahav, L. Leiserowitz, J. Phys. Chem. 98 (1994) 4087.
[72] F. Leveiller, D. Jacquemain, L. Leiserowitz, K. Kjaer, J. Als-Nielsen, J. Phys. Chem. 96 (1992) 10380.
[73] D.E. Williams, Acta Cryst. 21 (1967) 349.
[74] D.E. Williams, T.L. Starr, Comput. Chem. 9 (1977) 173.
[75] D.E. Williams, Acta Cryst. A 36 (1980) 715.
[76] A.T. Hagler, E. Huler, S. Lifson, J. Am. Chem. Soc. 96 (1974) 5319.
[77] A.T. Hagler, S. Lifson, P. Dauber, J. Am. Chem. Soc. 101 (1979) 5122.
[78] A. Gavezzotti, J. Am. Chem. Soc. 113 (1991) 4622.
[79] H.R. Karfunkel, R.J. Gdanitz, J. Compt. Chem. 13 (1992) 1171.
[80] Z. Berkovitch-Yellin, L. Leiserowitz, J. Am. Chem. Soc. 102 (1980) 7677.
[81] T. Hahn (Ed.), International Tables for Crystallography, Vol. A (Reidel Publishing, 1987).
[82] C. Böhm, F. Leveiller, D. Jacquemain, H. Möhwald, K. Kjaer, J. Als-Nielsen, I. Weissbuch, L. Leiserowitz, Langmuir 10 (1994) 830.
[83] F. Leveiller, C. Böhm, D. Jacquemain, H. Möhwald, L. Leiserowitz, K. Kjaer, J. Als-Nielsen, Langmuir 10 (1994) 819.
[84] S. P. Weinbach, K. Kjaer, J. Als-Nielsen, M. Lahav, L. Leiserowitz, J. Phys. Chem. 97 (1993) 5200.
[85] S. P. Weinbach, D. Jacquemain, F. Leveiller, K. Kjaer, J. Als-Nielsen, L. Leiserowitz, J. Am. Chem. Soc. 115 (1993) 11110.
[86] R. M. Richardson, S. J. Roser, Liquid Crystals 2 (1987) 797.
[87] M. J. Grundy, R. M. Richardson, S. J. Roser, J. Penfold, R. C. Ward, Thin Solid Films 159 (1988) 43.

[88] (a) M.J. Bedzyk, D.H. Bilderback, G.M. Bommarito, M. Caffrey, J.S. Schildkraut, Science 241 (1988) 1788;
(b) M.J. Bedzyk, G.M. Bommarito, M. Caffrey, T.L. Penner, Science 248 (1990) 52;
(c) H.D. Abrunña, G.M. Bommarito, D. Acevedo, Science 250 (1990) 69.
[89] P. Dutta, J.B. Peng, B. Lin, J.B. Ketterson, M. Prakash, P. Georgopoulos, S. Ehrlich, Phys. Rev. Lett. 58 (1987) 2228.
[90] B. Di Blasio, V. Pavone, C. Pedone, Cryst. Struct. Comm. 6 (1977) 745.
[91] F. Leveiller, D. Jacquemain, M. Lahav, L. Leiserowitz, M. Deutsch, K. Kjaer, J. Als-Nielsen, Science 252 (1991) 1532.
[92] M. Yazdanian, H. Yu, G. Zografi, Langmuir 6 (1990) 1093.
[93] B. Lin, T.M. Bohanon, M.C. Shih, P. Dutta, Langmuir 6 (1990) 1665.
[94] M. Shih, T. Bohanon, J. Mikrut, P. Zschack, P. Dutta, J. Chem. Phys. 96 (1992) 1556.
[95] (a) R.D. Kornberg, H.O. Ribi, in: Protein Structure, Folding, Design 2, Proceedings of a Dupont-UCLA Symposium, D.L. Oxender (Ed.) (Alan R. Liss,Inc., New York, 1987) p. 175;
(b) E.E. Uzgiris, R.D. Kornberg, Nature (Lond.) 301 (1983) 125;
(c) H.O. Ribi, P. Reichard, R.D. Kornberg, Biochemistry 26 (1987) 7974;
(d) S.D. Ludwig, H.O. Ribi, G.K. Schoolnik, R.D. Kornberg, Proc. Natl. Acad. Sci. USA 83 (1986) 8585;
(e) S.A. Darst, H.O. Ribi, W. Pierce, R.D. Kornberg, J. Mol. Biol. 203 (1988) 269;
(f) A.C. Ku, S.A. Darst, C.R. Robertson, A.P. Gast, R.D. Kornberg, J. Phys. Chem. 97 (1993) 3013.
[96] (a) D.W. Grainger, A. Reichert, H. Ringsdorf, C. Salesse, FEBS Lett. 252 (1989) 73;
(b) M. Ahlers, R. Blankenburg, D.W. Grainger, H. Ringsdorf, C. Salesse, Thin Solid Films 178 (1989);
(c) M. Ahlers, R. Blankenburg, H. Haas, D. Möbius, H. Möhwald, W. Müller, H. Ringsdorf, H.-U. Siegmund, Adv. Mater. 3 (1991) 39;
(d) R. Blankenburg, P. Meller, H. Ringsdorf, C. Salesse, Biochemistry 28 (1989) 8214.
[97] (a) I. Weissbuch, G. Berkovic, M. Lahav, L. Leiserowitz, J. Am. Chem. Soc. 112 (1990) 5874;
(b) I. Weissbuch, G. Berkovic, R. Yam, J. Als-Nielsen, K. Kjaer, M. Lahav, L. Leiserowitz, J. Phys. Chem. (1994), submitted for publication.
[98] M. Gavish, R. Popovitz-Biro, M. Lahav, L. Leiserowitz, Science 250 (1990) 973.
[99] B. R. Heywood, S. Mann, Adv. Mater. 6 (1994) 1, and references cited therein.
[100] I. Weissbuch, J. Majewski, K. Kjaer, J. Als-Nielsen, M. Lahav, L. Leiserowitz, J. Phys. Chem. 97 (1993) 12848.
[101] X.K. Zhao, J. Yang, L.D. McCormick, J.H. Fendler, J. Phys. Chem. 96 (1992) 9933.
[102] X.K. Zhao, L.D. McCormick, J.H. Fendler, Chem. Mater. 3 (1991) 922.
[103] K.V. Titova, E.I. Kolmakova, V.Y. Rosolovskii, Russ. J. Inorg. Chem. 27 (1982) 347 (Engl. Transl.).
[104] (a) B. Vonnegut, J. Appl. Phys. 18 (1947) 593;
(b) M.L. Corrin, J.A. Nelson, J. Phys. Chem (1968) 643.
[105] (a) R.C. Schnell, C. Vali, Nature 263 (1972) 163;
(b) L.R. Maki, E. L. Galyon, M. Chang Chien, D.R. Colwell, Appl. Microbiol. 28 (1974) 456.
(c) S.E. Lindow, D.C. Arny, C.D. Upper, Phytopathology 68 (1978) 523.
[106] (a) N.Y. Fletcher, The Chemical Physics of Ice (Cambridge University Press, Cambridge, 1970) p. 73;
(b) B. Kamp, in: Ice Polymorphism and the Structure of Water in Structural Chemistry and Molecular Biology, A. Rich, N. Davidson (Eds.) (Freeman Press, San Francisco, 1968) p. 507.
[107] H.R. Prappacher, Z. Angew. Math. Phys. 14 (1963) 590.
[108] L. Pauling, J. Am. Chem. Soc. 57 (1935) 2680.
[109] H.M. McConnell, L. Tamm, R.M. Weiss, Proc. Natl. Acad. Sci. USA 81 (1984) 3249.
[110] S.A. Darst, M. Ahlers, P.H. Meller, E.W. Kubalek, R. Blankenburg, H.O. Ribi, H. Ringsdorf, R.D. Kornberg, Biophys. J. 59 (1991) 387.
[111] W.A. Hendrickson, A. Pähler, J.L. Smith, Y. Satow, E.A. Merrit, R.P. Phizackerley, Proc. Natl. Acad. Sci. USA 86 (1989) 2190.
[112] D. Vaknin, J. Als-Nielsen, M. Piepenstock, M. Lösche, Biophys. J. 60 (1991) 1545.
[113] D. Vaknin, K. Kjaer, H. Ringsdorf, R. Blankenburg, M. Piepenstock, A. Diederich, M. Lösche, Langmuir 9 (1993) 1171.
[114] M. Lösche, M. Piepenstock, A. Diederich, T. Grünewald, K. Kjaer, D. Vaknin, Biophys. J. 65 (1993) 2160.
[115] M. Lösche, C. Erdelen, E. Rump, H. Ringsdorf, K. Kjaer, D. Vaknin, Thin Solid Films 242 (1994) 112.

[116] I. Weissbuch, L. Leiserowitz, M. Lahav, J. Am. Chem. Soc. 113 (1991) 8941.
[117] H.D. Göbel, H. Möhwald, Thin Solid Films 159 (1988) 63.
[118] H. D. Göbel, K. Kjaer, J. Als-Nielsen, H. Möhwald Thin Solid Films 179 (1989) 41.
[119] (a) M. Seul, P. Eisenberger, H.M. McConnell, Proc. Natl. Acad. Sci. U.S.A. 80 (1983) 5795;
(b) M.G. Samant, C.A. Brown, J.G. Gordon, Langmuir 7 (1991) 437.
[120] M.C. Shih, T.M. Bohanon, J.M. Mikrut, P. Zschack, P. Dutta, Phys. Rev. A 45 (1992) 5734.